Elastic Registration of Medical Images Using Generic Dynamic Deformation Models

ELASTIC REGISTRATION OF MEDICAL IMAGES USING GENERIC DYNAMIC DEFORMATION MODELS

BY

BAHRAM MARAMI

M.Sc., Electrical Engineering

Sharif University of Technology, Tehran, Iran

B.Sc., Biomedical Engineering

B.Sc., Electrical Engineering

Amirkabir University of Technology, Tehran, Iran

A THESIS

SUBMITTED TO THE DEPARTMENT OF ELECTRICAL & COMPUTER ENGINEERING

AND THE SCHOOL OF GRADUATE STUDIES

OF McMASTER UNIVERSITY

IN PARTIAL FULFILMENT OF THE REQUIREMENTS

FOR THE DEGREE OF

DOCTOR OF PHILOSOPHY

Doctor of Philosophy (2013) McMaster University

(Electrical & Computer Engineering) Hamilton, Ontario, Canada

TITLE:	Elastic Registration of Medical Images Using Generic Dynamic Deformation Models
AUTHOR:	Bahram Marami M.Sc., Electrical Engineering Sharif University of Technology, Tehran, Iran B.Sc., Biomedical Engineering B.Sc., Electrical Engineering Amirkabir University of Technology, Tehran, Iran
SUPERVISORS:	Dr. Shahin Sirouspour and Dr. David W. Capson
NUMBER OF PAGES:	193

To my beloved family

Abstract

Modern imaging techniques are increasingly used in healthcare and medical research. Fusion of information obtained from images of the same or different modalities and/or dimensionalities can greatly help physicians in diagnosis and treatment of diseases. To this end, the images must be spatially aligned through a procedure often referred to as "image registration". Since soft tissue organs in the human body can undergo significant deformation between imaging sessions or during an intervention, registration techniques that would account for such non-rigid geometrical transformations are of great interest.

This thesis presents a family of automatic elastic registration methods applicable to single and multimodal images of similar or dissimilar dimensions. These registration algorithms employ a generic *dynamic* linear elastic continuum mechanics model of the tissue deformation which is discretized using the finite element method. The dynamic deformation model provides spatial and temporal correlation between images acquired from different orientations at different times. First, a volumetric registration algorithm is presented which estimates the deformation field by balancing internal deformation forces of the elastic model against external forces derived from an intensity-based similarity/distance measure between images. The registration is achieved by iteratively solving a reduced form of the dynamic deformation equations in response to image-derived nodal forces.

A general approach for automatic deformable image registration is also presented in this thesis which deals with different registration problems within a unified framework irrespective of the image modality and dimension. Using the dynamic deformation model, the problem of deformable image registration is approached as a classical *state estimation* problem with various image similarity/distance measures providing an observation model. With this formulation, single and multiple-modality, three-dimensional (3D)-3D and 3D-2D image registration problems can all be treated within the same framework. The registration is achieved through a *Kalman*-like filtering process which incorporates information from the deformation model and an observation error computed from an intensity-based similarity/distance measure. Correlation ratio, normalized correlation coefficient, mutual information, modality independent neighborhood descriptor and sum of squared differences

between images are similarity/distance measures employed for single and multiple modality image registration in this thesis.

The performance of the proposed registration algorithms are evaluated in a number of different registration scenarios. First, 3D magnetic resonance (MR) images of a realistic breast phantom are registered to its compressed 3D high- and low-resolution MR images. 3D MR images of uncompressed and compressed actual breast tissue are also registered using the proposed 3D-3D registration algorithms. The state estimation-based registration method is employed to register 3D MR images to a sequence of simulated 2D interventional MR images acquired from a breast phantom as well as human breast tissue with static deformation. Furthermore, the registration algorithm is employed to dynamically track a target sub-volume inside the breast tissue during the process of needle insertion using a sequence of 2D intraoperative images. Finally, the algorithm is assessed in dynamically tracking the deformation of a breast phantom, based on registration of 3D preoperative MR images to its real-time intraoperative 2D ultrasound (US) images.

The results presented in this thesis show that the proposed family of elastic registration methods can significantly improve the quality of image matching in terms of target registration error (TRE). TREs resulted from the proposed methods are comparable to those obtained using image registration toolkit (IRTK) in 3D-3D MR-MR registration; the proposed methods outperform IRTK in 3D-2D MR-MR static registration. Registration results in dynamic 3D-2D MR-MR and MR-US scenarios demonstrate that real-time large deformations of a breast phantom as well as actual breast tissue can be tracked with a TRE less than 2 mm. Other qualitative and quantitative performance evaluations are also reported in the thesis.

Acknowledgements

Foremost, I would like to express my sincere appreciation and gratitude to my supervisor, Dr. Shahin Sirouspour, for his continuous support, motivation, guidance and brilliant ideas throughout my Ph.D. study and writing my thesis. I would also like to thank my co-supervisor, Dr. David W. Capson, for his support and encouragement during my study at McMaster University. Beside my supervisors, I would like to extend my gratitude to my advisory committee members, Dr. Shahram Shirani for his encouragement and insightful comments, and Dr. Michael D. Noseworthy, for his valuable comments and tremendous support in providing the access to medical images, MRI scanner and US machine.

I warmly thank Dr. Peter Bevan, Dr. Jan Modersitzki and Dr. Alexandru Patriciu for their helps and comments on my research project. My sincere gratitude goes to my fellow labmates and friends at McMaster University for all the fun and joyful time we have had during last five years. I am also grateful to Dr. Aaron Fenster and his group members at Robarts Research Institute for their support at the final stages of my thesis and their valuable comments on my project.

Last but not the least, I would like to warmly thank my family, my parents, my brothers and sisters, for their endless love and support throughout my life. I could not have imagined getting my Ph.D. without their motivation and encouragement.

List of Acronyms

cMI	Conditional Mutual Information
CR	Correlation Ratio
CT	Computed Tomography
DRAMMS	Deformable Registration via Attribute Matching and Mutual-Saliency
DRR	Digitally Reconstructed Radiograph
FFD	Free-Form Deformation
FFT	Fast Fourier Transform
FE	Finite Element
FEM	Finite Element Method
FLE	Fiducial Localization Error
FRE	Fiducial Registration Error
GPU	Graphics Processing Unit
IRTK	Image Registration Toolkit
IIR	Infinite Impulse Response
MI	Mutual Information
MIND	Modality Independent Neighbourhood Descriptor
MR	Magnetic Resonance
MRI	Magnetic Resonance Imaging
NCC	Normalized Correlation Coefficient
NMI	Normalized Mutual Information

PDE	Partial Differential Equation
PET	Positron Emission Tomography
RBF	Radial Basis Functions
RMS	Root Mean Square
SNR	Signal-to-Noise Ratio
SPECT	Single Photon Emission Computed Tomography
SPSA	Simultaneous Perturbation Stochastic Approximation
SSD	Sum of Squared Differences
std	Standard Deviation
SVD	Singular Value Decomposition
TPS	Thin-Plate Splines
TRE	Target Registration Error
TRUS	Transrectal Ultrasound
US	Ultrasound
2D	Two-Dimensional
3D	Three-Dimensional

Contents

List of Figures

Chapter 1

Introduction

This chapter introduces the research problem and objectives of the thesis, and gives a summary of the proposed solution approaches. It first outlines the context and motivation of the work and explains the problem. The philosophy of the proposed image registration framework is briefly discussed along with major contributions of the thesis from an application perspective. Finally, an overview of all chapters of the thesis as well as a list of related publications are given.

1.1 Motivation

During the last two decades, modern imaging technologies have made it possible to non-invasively visualize different organs and structures of the human body. Medical images provide valuable information about the internal organs, their structures and functionality, all with minimum pain and discomfort for the patient. This information may be in the form of the two-dimensional (2D) projection images of traditional radiography, 2D slices of US images, or full three-dimensional (3D) images acquired by magnetic resonance imaging (MRI), X-ray computed tomography (CT), positron emission tomography (PET), single

photon emission computed tomography (SPECT), functional MRI, or US. Imaging techniques differ in quality and resolution, sensitivity to various biological tissue properties, risk to the patient, speed of image acquisition, availability and cost. They use different sensors and capture different properties of the tissue. High-resolution MRI and X-ray CT images provide detailed structural information about internal organs. Bony and dense structures are best observed in CT images, while soft-tissue structures are better visualized in magnetic resonance (MR) images. Yet, both MR and CT imaging capture anatomical information and not functional behaviour [1]. In contrast, PET and SPECT allow metabolic measurement and are able to display functional aspects of the body [2]. However, PET and SPECT perform poorly in capturing anatomical structures.

Fusing information from various imaging modalities could provide complementary information about the imaged tissue. Image fusion is helpful in reducing uncertainty and increasing reliability in medical diagnosis by maximizing relevant information particular to an application [3]. Fused images may also be created from a sequence of single modality images to enhance the quality of imaging [4]. The integration of information from different images is usually achieved in two steps. First, image data sets are spatially aligned through a procedure referred to as *image registration*. In the second step, the contents of the images are fused to generate a single image from the original images. Therefore, registration is an essential task in image fusion. Modern medical scanners that capture registered multi-modality images simultaneously are also becoming available, e.g., see [5, 6].

Beside multi-modality image fusion, there are other important applications for registration of single-modality images taken at different times. Detection of the breast cancer in MR images requires injection of a contrast agent. The contrast agent uptake curve in malignant disease is different from that of benign disease [7]. The rate of uptake can be

quantified from the difference between images prior to injection and a dynamic sequence of postcontrast images. These images have to be non-rigidly aligned in order to facilitate the analysis of pre and postcontrast image information [8]. Verification of treatment by comparing pre and post treatment images [9], and monitoring tumors growth using time series of images [10] are other example applications of single-modality image registration.

High-resolution preoperative MRI/CT images are usually used for diagnosis of diseases, localization of lesions and tumors, and treatment planning. However, treatment and interventional plans based on preoperative image data are not accurate and reliable during the actual procedure because of the possible movement and deformation of the underlying tissue. Therefore, preoperative plans have to be updated using intraoperative images. In breast biopsy for cancer diagnosis and treatment, lesions are preoperatively identified and localized using MR or CT images in supine position [11, 12]. However, MR-guided breast biopsy is usually performed while the patient is in a prone position. Furthermore, the breast is immobilized by compression to prevent any shift during the needle insertion [12]. Therefore, pre-treatment plans have to be updated during the procedure by co-registering pre and intraoperative images to account for the movement and deformation of the tissue. A significant shape change also occurs between pre and intraoperative images in MR-guided prostate brachytherapy or ablation therapy. Preoperative imaging is usually conducted with the patient in supine position using an endorectal coil [13]. Intraoperatively, the patient is in the lithotomy position with a rectal obturator in place [13, 14]. The difference in the volume of the bladder is also another source of deformation between pre and intraoperative images. To improve the information content of intraoperative images and better visualize substructures of the prostate during the operation, preoperative high-field MR images need to be registered to low-resolution low-field intraoperative images. Lesion outlines and the

targeted area can then be updated in intraoperative images accordingly [14].

Intraoperative MRI or CT imaging is difficult and often impossible to achieve in image-guided interventional procedures for several reasons. MRI scanners are not compatible with many other equipment and surgical instruments in the operation room. To limit exposure to the ionizing radiation, CT imaging cannot be used while the operation is being performed. Limited space inside the imaging machine also restricts surgeon's access to the operating field. Moreover, long acquisition and processing times make it difficult to have high-resolution images at sufficiently high update rates during the procedure. MRI has very few known harmful effects on the human body compared to X-ray and nuclear imaging. This has motivated engineers and scientists to develop technologies for utilizing MRI in interventional radiology. During the last decade, many dedicated interventional MRI systems have been developed for minimally invasive procedures, e.g. see [12, 15–17]. The cost of these systems is very high, primarily due to the limitations concerning the types of material that could be used inside MRI machines. Interventional MRI systems acquire one or a few image slices from certain orientations from the patient's body during the procedure [18]. These few image slices would only provide limited information compared to what is available from preoperative high-resolution image volumes [15]. Furthermore, signal-to-noise ratio (SNR) in interventional images is lower than diagnostic MR images. This is due to the weaker magnetic field of the open magnets used in interventional imaging compared to that of conventional diagnostic imaging systems [15].

US as an intraoperative imaging technique is safe for both the patient and the radiologist. US can also be easily used in the operating room with other equipment. US images are essentially 2D tomographic images captured with small transducers. 3D US images can be

constructed using several 2D slices in different orientations. This is accomplished by special 3D transducers or by a 2D probe sweeping the object using a mechanical device [19]. US has been widely used in interventional procedures such as image-guided biopsy [20] and ablation therapy [21, 22] due to its low cost, availability and fast acquisition time. However, this imaging technique has some significant limitations. US has a very limited field of view and the quality of its images is inferior to MR or CT images. US images have low SNR and often suffer from artifacts and speckle noise. This reduces US sensitivity in detecting relatively small lesions and tumors.

To take advantage of high-resolution MR/CT imaging systems during medical procedures, preoperative image volumes can be registered to the limited (e.g., low quality, low resolution, one of a few sparse image slices) but real-time data, e.g., interventional MRI or US images. This co-registration would help the medical practitioner form a comprehensive understanding of the underlying tissue. Operational plans can also be updated accordingly based on the registered images. The development of a method for non-rigidly registering images of different modalities and dimensions can be very valuable in various medical applications such as disease diagnosis, therapies, monitoring, and minimally invasive procedures.

1.2 Problem Statement and Thesis Objectives

Image registration is a fundamental task in medical image analysis whenever more than one set of images are involved. Since there is no guarantee that the patient would be placed exactly in the same position at different imaging sessions with respect to the imager coordinate frame, images acquired at different times would not be spatially aligned. Therefore, in order to compare images from different sessions or modalities, they need to be

co-registered. Rigid body motion, in which the distances between all points in the images are preserved, can be compensated using a rigid transformation with up to six parameters. A rigid transformation is comprised of translations along and rotations about axes of the co-ordinate frame. This mapping is the simplest registration which can be effectively applied to rigid anatomical structures such as bones and skull. However, most organs in the human body are non-rigid and deform due to internal and external loads. For instance, during the respiration process, most organs in the abdominal region experience deformation to some extent. The deformation may also be caused by the patient movement between imaging sessions or by external devices such as imaging and surgical tools.

To register images with non-rigid morphological changes within the organs during the imaging sessions, a more complicated function than a rigid transformation is needed. In rigid registration, a single transformation is applied to all voxels/pixels of the source image to match it with the target image. But, in non-rigid registration, ideally a deformation vector field is determined for each image voxel/pixel. Applying the total deformation vector field to the source image establishes a geometrical mapping between two images based on a similarity/distance metric. Image registration is an ill-posed problem by itself [23], meaning that several (infinite) solutions may exist for a given registration problem. Having a very large number of degrees of freedom in deformable image registration renders it into a complex and computationally intensive mathematical problem. Imposing constraints on the deformation field could reduce the number of degrees of freedom and regularize the problem to achieve a unique solution. Constraints can be *static* based on anatomical landmarks or control points, or be in the form of a *dynamic* deformation model of a solid body.

Intraoperative images are often in the form of 2D X-ray projection images, 2D slices of

US images, or a sequence of sparse 2D tomographic MR images. X-ray projection images are usually used in procedures involving bony structures. Most commonly, simulated X-ray projection images called digitally reconstructed radiographs (DRRs) from preoprerative 3D MR/CT images are rigidly registered to intraoperative X-ray images [24]. Non-rigid registration of preoperative volumetric image data to intraoperative 2D tomographic images is more challenging and of great importance. Most of the previously developed 3D-2D registration methods employ a rigid transformation and try to find the best matching among interpolated slices of preoperative images to 2D intraoperative images, e.g., see [15, 25]. Developing an automatic deformable registration method for matching preoperative image volumes to 2D intraoperative images is critical for many medical imaging applications and is subject of ongoing research.

The goal of this thesis is to develop a family of versatile deformable registration methods applicable to medical diagnosis and image-guided interventions. These registration methods must meet the following requirements:

1. They should be able to align images from the same or different modalities.

2. They are expected to be automatic or at least require minimum manual intervention by the physician.

3. They should be applicable to images from various soft tissues in the human body such as breast, prostate, and liver, perhaps with some small modification in the algorithm.

4. They should be capable of aligning images of different dimensions, i.e., should be able to handle 3D-3D and 3D-2D registration problems.

5. They should account for both static and dynamic tissue deformations. In a static deformation scenario, the preoperative images are registered to the intraoperative images of a

statically deformed tissue, whereas in a dynamic deformation scenario, the preoperative images are registered to a sequence of 2D or 3D intraoperative images of a dynamically deforming tissue over time.

1.3 Solution Approach and Thesis Contributions

A model of tissue deformation can incorporate image information from different orientations or different times into a common framework. Physics-based models relate geometry and material properties of the objects to their dynamics considering applied loads, boundary conditions and other constraints. These models are very useful in many simulation and estimation applications as well as in soft tissue deformation modelling. In this thesis, a new class of model-based deformable registration methods is proposed for the registration of multi-modal and multi-dimension images. The proposed registration methods employ a generic "dynamic" linear elastic model of the tissue deformation, discretized by the finite element method (FEM). Rather than constructing a finite element (FE) mesh based on the actual geometry of the tissue, registration methods utilize a cubic mesh of tetrahedral finite elements for the creation of the deformation model. Dynamical modes of the deformation model are decoupled based on a modal transformation of the state variables. Fast vibrational modes of the decoupled model can be discarded to significantly reduce computations with minimal impact on the registration results at a particular time scale relevant to the application of interest.

First, a volumetric registration method is presented which estimates the deformation field by balancing the internal elastic forces of the model against external image-derived forces. In similar optimization-based methods in the literature, the registration is achieved by minimizing a cost function comprised of an intensity-based similarity/distance measure

and the weighted linear elastic energy of the model. Rather than finding the minimum of the cost function using traditional optimization methods, in this thesis, the developed dynamic deformation model is employed to solve the Euler-Lagrange equilibrium equations derived from the cost function. The registration is achieved by iteratively solving the dynamic deformation model over time in response to nodal forces derived from an intensity-based similarity/distance measure. The steady-state equilibrium of the dynamic model would minimize the cost function associated with the intensity-based image registration problem which is regularized by the linear elastic energy of the deformation model. Discarding fast vibrational modes of the dynamic model helps the solution to smoothly converge to the equilibrium. The convergence of the reduced dynamic nonlinear system of equations is usually faster than solving the static equations using other means [26].

The registration method described above can only be applied to 3D-3D registration problems. Using a dynamic elastic deformation model, a general approach for automatic deformable image registration is also presented in this thesis which deals with different registration problems within a unified framework irrespective of the image modality and dimension. The problem of deformable image registration is approached from a new perspective, i.e., "state estimation" for dynamical systems. The registration is achieved through a *Kalman*-like filtering process which incorporates information from the deformation model and an observation error computed from an intensity-based similarity/distance measure. Using the proposed approach, single and multiple-modality, 3D-3D and 3D-2D image registration problems with static or dynamic tissue deformation can all be treated in the same framework.

The general flow of the proposed family of registration methods is shown in Figure 1.1.

In this state estimation-based registration, the unknown states to be estimated are the positions and velocities of the nodal points of the volumetric finite element (FE) mesh based on which the deformation model is constructed. In this framework, the intraoperative image data sets are the sensor observations based on which the estimation of the current state of deformation is carried out. At any time, the soft tissue undergoes deformation caused by external applied loads or imaging and interventional tools. Real-time imaging of the deforming tissue provides a "reference image". The reference image can be a 3D volume, or a sparse sequence of 2D images (one or a few slices). The "template image" is the corresponding image slices in the coordinate of the preoperative image volume. The states of tissue deformation are estimated in an iterative algorithm. At each iteration, deformation states are first predicted based on their estimates from the previous iteration using the dynamics of the deformation model. This prediction (time update) gives *a priori* estimate of the deformation states ($\hat{\mathbf{x}}_k^-$) based on which the displacement field of the template image is predicted. The predicted deformation field is applied to the template image, and the deformed template image is interpolated. A comparison between the reference image and the deformed template image provides an observation prediction error. Estimation algorithm updates the state estimates based on a correction term proportional to the observation prediction error.

In this thesis, images are compared based on various intensity-based similarity/distance measures including sum of squared differences (SSD), correlation ratio (CR), normalized correlation coefficient (NCC), mutual information (MI) and modality independent neighbourhood descriptor (MIND) for single and multi-modality image matching. The iterative algorithm terminates when the relative change in the similarity/distance measure is less than a given small number ε or the total iterations exceeds a maximum number.

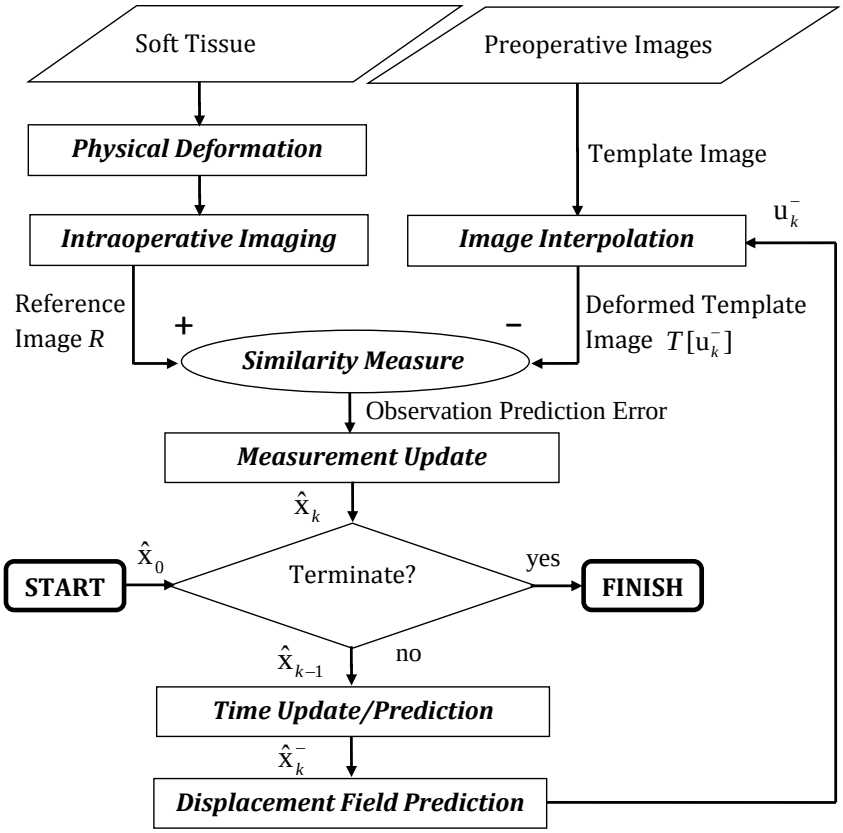

Figure 1.1: General flow of the iterative registration method based on the concept of dynamic state estimation.

The strengths and versatility of the proposed registration methods stem from a number of key differences with existing model-based deformable registration algorithms in the literature which are summarized below.

a) Instead of a static model, a dynamic linear elastic deformation model is employed. This allows for the registration of dynamically deforming tissue, e.g., during needle insertion, from a sequence of (real-time) intraoperative images. Basically, the dynamic deformation model recursively correlates image information over time and provides the deformation needed for matching preoperative and intraoperative images. In the case that

tissue deformation is static, the algorithm simply converges to a steady-state solution.

b) No specific geometry information is computed from the preoperative images; instead, a cubic or spherical volume discritized by tetrahedral finite elements is employed for the registration. In most of the existing model-based deformable registration methods, a geometrical model of the tissue is constructed from the segmented preoperative images. Then, the geometrical model is associated to the material properties using linear or non-linear equations. The model is deformed by solving the resulting system of equations given the boundary conditions and applied loads/forces which are determined based on the difference in the object surfaces and anatomical features extracted from preoperative and intraoperative images [27–29]. Extracting surfaces and other image features from preoperative and intraoperative image data is often difficult and unreliable, especially in multi-modality image registration. Also, for constructing an accurate linear or nonlinear model, mechanical properties of the tissue with all its substructures have to be quantified, which requires a good understanding of normal and pathological tissue properties. Therefore, these methods involve image and tissue preprocessing steps, and possibly manual interventions by specialists at high computational and time costs.

   In the proposed methods in this thesis, the model can be geometrically and physically inaccurate and still produce acceptable results. This is partly due to the fact that the estimation process takes into account modelling and imaging uncertainties in the form of unknown process and measurement disturbances. This makes the method applicable to any soft tissue in the body such as breast, liver and prostate with relatively straightforward modifications in the deformation model and the observation prediction error.

c) Unlike other model-based registration methods, the deformation model in the proposed methods is rather generic. In other words, the model is not patient specific and the same

deformation model constructed for an organ, for instance the model for breast deformation, can be used for images acquired from any patient. Most of the previous work in the literature construct a patient specific deformation model to warp the preoperative image based on the deformation computed for the model [30–32]. However, developing an accurate deformation model is very difficult because of the complex nonlinear behaviour of the soft tissue inside the body, their heterogeneous texture and their interaction with surrounding deformable tissues. The linear elastic model employed in the registration method proposed in this thesis is determined based on two elasticity parameters [26]. The state-estimation framework allows uncertainty in the model parameters in the form of process disturbances.

d) The proposed method requires no manual intervention or explicit feature extraction from the images for the calculation of boundary conditions and external forces which are required in most model-based registration methods. The deformation estimation is carried out merely based on the model and image intensity information. The observation prediction error, which is used for estimating the deformation states, is automatically computed based on the analytical gradient of the similarity/distance measure. It should be noted that, extracted image features such as edges and surfaces can be easily utilized in the algorithm to compute the observation prediction error. However, in this thesis, registration is performed solely based on the grayscale information in the template (3D) and reference (3D or 2D) images and does not involve pre- or post- processing of the images.

e) The formulation of the registration as state estimation allows for a unified treatment of the problem irrespective of the image modality and dimension. In other words, single-modality, multiple-modality, 3D-3D and 3D-2D registration problems can all be solved

within the same framework with the only difference being in the way the observation prediction errors are calculated.

The main contributions of this thesis are as follows.

1. A FEM-based dynamic linear elastic deformation model is developed which uses a cubic volume discritized by tetrahedral finite elements. Using the dynamic deformation model, a 3D-3D registration method is proposed which estimates the deformation field between images by balancing internal deformation forces of the elastic model against external image-derived forces. The registration is achieved by iteratively solving the dynamic deformation equations over time in response to nodal forces derived from intensity-based similarity/distance measures between images. Fast vibrational modes of the model are isolated using a canonical modal transformation and discarded without significantly affecting the steady-state response of the system. The steady-state equilibrium of the dynamic model represents the minimum of a cost function comprised of the similarity/distance measure between images and the linear elastic energy of the deformation model. The proposed method is used to register high-resolution 3D MR images of a breast phantom to its compressed 3D high and low-resolution MR images. The method is also evaluated in 3D-3D registration of MR images acquired from normal and compressed actual breast tissue.

2. A generic class of deformable registration methods is proposed based on the philosophy of state estimation for dynamical systems to register multi-modal and multi-dimensional images. In this framework, a dynamic linear elastic deformation model describes the tissue response under unknown external disturbance forces. The deformation of the tissue is then estimated using a state estimator based on the deformation model and an intensity-based similarity/distance measure between the template and reference images.

3. An instance of the general state estimation-based registration is developed and examined for 3D-3D registration of volumetric images. The method is evaluated in 3D-3D registration of normal and compressed MR images acquired from a breast phantom as well as actual breast tissue. This scenario would be relevant in breast needle biopsy if one were to register pre-treatment diagnostic images to intraoprative images right before the needle insertion to locate the target in the intraoperative images.

4. An instance of the general state estimation-based registration algorithm is developed to register preoperative 3D images to a sparse sequence of intraoperative 2D images acquired from the tissue with static deformation. In this registration scenario, the deformation states of the tissue are estimated based on the deformation and observation models to spatially correlate image information obtained from different cross-sections. The method is evaluated in the registration of 3D MR images of a breast phantom to a sequence of 2D MR images of the compressed phantom acquired from different cross-sections. 3D MR images of the actual breast tissue are also registered to a sequence of interventional 2D MR images acquired from the compressed breast.

5. An instance of the general state estimation-based registration algorithm is developed to register preoperative image volumes to real-time intraoperative 2D images of a dynamically deforming tissue. The states of tissue deformation is estimated over time using the proposed method based on a sequence of real-time 2D images. This approach can be used for real-time tracking of tissue deformation in image-guided interventions, e.g., breast biopsy or prostate ablation therapy. The proposed method is evaluated in tracking a target sub-volume inside the breast tissue based on registering 3D preoperative images to a sequence of real-time 2D MR images during a simulated MR-guided breast biopsy experiment. Also, the dynamic deformation of a breast phantom is tracked over time

based on 3D-2D MR-US image registration using the proposed method.

1.4 Thesis Organization

The rest of this thesis is organized as follows. Chapter 2 provides a brief review on existing imaging techniques, image registration methods and pertinent registration literature. In Chapter 3, the FEM-based dynamic tissue deformation model is developed. In Chapter 4, the dynamic deformation model is employed in an optimization-based registration approach to register volumetric images. In Chapter 5, the model-based deformable image registration problem is formulated as state estimation for dynamical systems. The developed generic method is evaluated in 3D-3D registration of MR images in this chapter. The state estimation-based registration method is employed in Chapter 6 to register 3D preoperative images to a sequence of 2D intraoperative images acquired from different cross-sections of the tissue with static deformation. In Chapter 7, the proposed registration method is employed to track the deformation of a soft tissue based on registration of 3D preoperative MR images to real-time 2D MR/US images of a dynamically deforming tissue. Chapter 8 discusses the results and computational aspects of the proposed registration methods. In Chapter 9, the thesis is concluded and some possible directions for further research are discussed.

1.5 Related Publications

- B. Marami, S. Sirouspour, and D. W. Capson, "Dynamic model-based deformable registration of medical images," submitted for publication in the journal of *Computerized Medical Imaging and Graphics.*

- B. Marami, S. Sirouspour, A. Fenster and D. W. Capson, "Dynamic tracking of a deformable tissue based on 3D-2D MR-US image registration," submitted for presentation at SPIE Medical Imaging 2014, San Diego, USA.

- B. Marami, S. Sirouspour, and D. W. Capson, "Model-based deformable registration of preoperative 3D to intraoperative low-resolution 3D and 2D sequences of MR images," in *Medical Image Computing and Computer-Assisted Intervention, MICCAI 2011*, pp. 460-467. Springer Berlin Heidelberg, Sep. 18–22, 2011, Toronto, Canada.

- B. Marami, S. Sirouspour, and D. W. Capson, "Model-based 3D/2D deformable registration of MR images," in *Engineering in Medicine and Biology Society, EMBC, 2011 Annual International Conference of the IEEE*, pp. 4880-4883, Aug. 28-Sep. 3, 2011, Boston, USA.

- H. Mousazadeh, B. Marami, S. Sirouspour, A. Patriciu, "GPU implementation of a deformable 3D image registration algorithm," in *Engineering in Medicine and Biology Society, EMBC, 2011 Annual International Conference of the IEEE*, pp. 4897-4900, Aug. 28-Sep. 3, 2011, Boston, USA.

Chapter 2

Literature Review

This chapter reviews the literature on medical image registration techniques and other related work to subject matter of this thesis. First, a brief introduction to medical imaging techniques is given. Next, image registration is defined and different aspects of registration problems are discussed. Deformable image registration methods are also reviewed. Finally, physical model-based image registration methods and their applications are discussed.

2.1 Medical Imaging

Medical imaging concerns creating images from the human body for clinical purposes. Over the last four decades, medical imaging has been increasingly used for diagnosis, treatment planing and monitoring disease progression. The origin of medical imaging dates back to November 1895 when Wilhelm Conrad Roentgen first discovered the X-ray [33]. During his experiments, he observed that the new radiation could penetrate some solid materials like human flesh better than others like bone, and penetrated rays could be recorded in photographic plates. Before that, physicians were relying on their senses to diagnose illnesses and treat injuries. However, human senses are quite limited in their ability to

provide information on an incredibly complex biological system such as the human body. Internal organs are mostly inaccessible to these senses, and it is really difficult to discern physiological and anatomical properties of the biological tissue based on the natural senses.

After the discovery of X-ray, many techniques were developed in the twentieth century to acquire images from the internal organs of the human body. These images provide massive amount of information about the anatomy and physiology of the body, without being physically invasive. Over the first half of the 1900s, X-ray imaging advanced and different dedicated imaging systems were developed [33]. "Fluoroscopy" [34] is an imaging technique for obtaining real-time moving images from the internal structures of the patient. Fluoroscopy uses X-rays and first was developed in 1920s. "Mammography" is another imaging technology based on X-ray for acquiring high-resolution images of the breast and is used in breast cancer diagnosis and treatment [35]. In the 1940s, "X-ray tomography" was introduced to produce tomographic images [33]. "Tomograms" are image slices that are obtained through the use of a penetrating wave. This technique is capable of imaging a slice of the tissue without showing the over- or underlying tissues [36]. This is different from conventional X-ray images which are acquired through projections. X-ray is also the basis for "Angiography", an imaging technique for visualizing inside of the blood vessels and organs of the body, introduced in 1950s [37].

In 1950s nuclear medicine was first employed in diagnostic imaging tests. In nuclear imaging, a small amount of radioactive material called "tracer" is injected into the body and a specialized camera is used to detect the radiation (mostly gamma) from different parts of the body and construct the image [1, 33]. Nuclear imaging based on organ-specific tracers can determine the cause of a medical problem by identifying the physiological function of the organ, whereas X-ray and other conventional radiological techniques only provide

anatomical information about the body. “Positron emission tomography” (PET) is a modern nuclear imaging technique which produces three-dimensional (3D) images of the body. A PET system detects pairs of gamma rays emitted indirectly in opposite directions by a positron emitting isotope. Based on the arrival time of the emitted rays at the detectors around the patients, the source of emission is localized and the image is constructed [1].

Ultrasound (US) imaging was first clinically used in 1970s and was developed for visualization of internal organs without using ionizing radiation [33]. In this technique, sound waves with a frequency above the audible range of normal human hearing pass through the tissue and are reflected back by different structures in the body. Reflected signals are detected by the US probe and tomographic images are created. US is a noninvasive imaging method and is frequently used for visualizing abdominal region especially for fetal imaging during pregnancy [33, 38]. Although the early US machines were bulky, the current systems are the most portable and widespread imaging devices available; some are smaller than a laptop computer. Figure 2.1 shows a clinical US system.

In early 1970s, digital computers entered into the world of medical imaging and accelerated the development of new imaging technologies. X-ray computed tomography (CT), which was invented in 1973, creates multiple tomographic images of the body [1, 33]. X-ray beams passing through the body structures are processed in computers and a 3D volumetric image is generated from a series of 2D images. Modern scanners often use a single gantry system to acquired both CT and PET images sequentially in the same session from the patient. This combined system, e.g., see Figure 2.2, is called PET/CT and allows two sets of acquired images to be co-registered to create a single image for diagnostic applications [5]. Using this system, functional images obtained by PET are fused with structural images captured by CT.

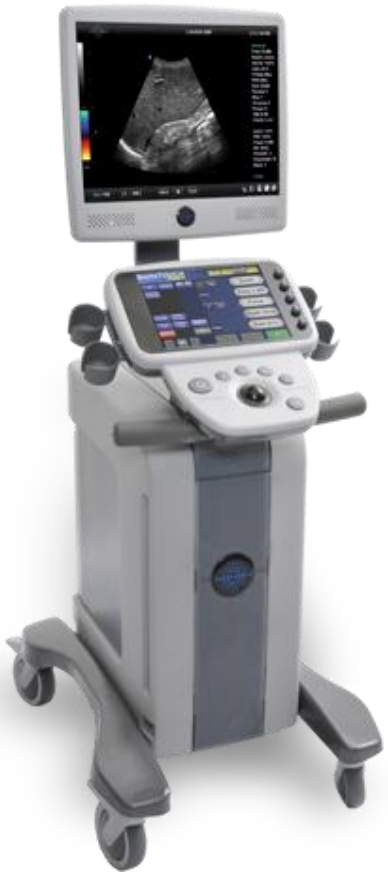

Figure 2.1: SonixTouch, a touch screen ultrasound system [39]. This imaging system was used to acquire the US data for MR/US registration in this thesis.

Magnetic resonance imaging (MRI) was developed during the 1970s to visualize internal structures of the body [33]. Unlike X-rays, MRI does not use ionizing radiations, but rather takes advantages of the property of nuclear magnetic resonance to image nuclei of atoms in the body. MRI produces images using a strong magnetic field, varying gradient fields and radio frequency waves. Inside the varying magnetic field, some atomic nuclei in the body produce radio frequency signals which can be detected by receiver coils. Nuclei at different locations resonate at different frequencies depending on the magnetic field gradients. Therefore, spatial information of the different nuclei can be extracted from the

Figure 2.2: Siemens Biograph 16 PET/CT, Imaging Research Centre, St. Josephs Healthcare, Hamilton, ON, Canada. Photo's courtesy of Dr. Michael D. Noseworthy.

measured signals using a *Fourier* analysis [33, 38]. The MRI machine which was used to acquire images for this thesis research is shown in Figure 2.3. It is well known that MRI differentiates soft tissue structures better that CT making it an important imaging technique for diagnostic applications related to muscles, the brain, the heart and the breast. During the 1990s superconducting magnets made it possible to have 1.5T (Tesla) and 3.0T MRI machines. More powerful MRI scanners with 7T [40] and 9.4T [41] magnetic fields have also being developed for research purposes. These high-field scanners yield a 2- to 3-fold improvement in image SNR over 3.0T systems. They also enable an imaging resolution of ≈ 0.1 mm^3 or 0.1μl which is $\approx 1\mu$l on current clinical 1.5T or 3.0T [42].

2.2 Image Registration

Image registration is the process of aligning two sets of images to establish spatial correspondence between their structures and features. These images could be acquired at

Figure 2.3: General Electric (GE) Discovery MR750 3.0T, Imaging Research Centre, St. Josephs Healthcare, Hamilton, ON, Canada. Photo's courtesy of Dr. Michael D. Noseworthy.

different times, using different imaging techniques, or from different viewpoints. Therefore, a mapping function has to be determined to relate one space to another. The mapping function which is also called "transformation" is two dimensional for 2D images and three dimensional for 3D images. Maurer and Fitzpatrick in [43] define "registration" as: "the determination of a one-to-one mapping between the coordinates in one space and those in another such that points in the two spaces that correspond to the same anatomical points are mapped to each other". In the literature, the image on which the transformation is applied is refered as "moving" or "template" image. The other image is called "target" or "reference" image. A simple example of registering two images is given in Figure 2.4. In this figure, a transformation is applied to the template (moving) image to align it with the

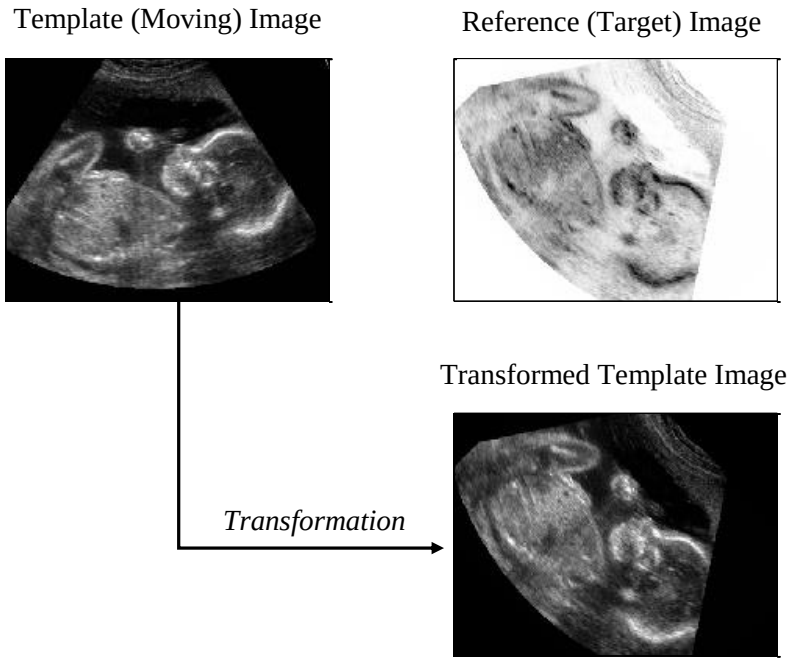

Figure 2.4: A simple example of image registration.

reference (target) image. As can be seen from this figure, although the transformed template image has a different intensity level, it is spatially aligned with the reference image. The transformation is this simple example is a 45 degrees of clockwise rotation around the center of the image. In this thesis, intraoperative images are referred by reference (R) and preoperative images are referred by template (T) images [42].

Given a reference image R and a template image T, image registration can be formulated as an optimization problem. Basically, registration is finding a transformation or a displacement field $\mathbf{u}$, so that the transformed image $T[\mathbf{u}]$ is as similar as possible to R. The objective function to be minimized is generally defined as

$$\underset{\mathbf{u}}{\text{minimize}} \quad J(\mathbf{u}) = I(R, T[\mathbf{u}]) \tag{2.1}$$

where I is a measure of similarity or closeness between images and is defined as a distance metric to be minimized. This measure, which is computed from the reference and template images, forms the basis of the registration [44]. The registration can be based on extrinsic factors such as fiducials (screw or skin markers), and frames and moulds which are invasively or non-invasively attached to the body of interest. Intrinsic information of the image used in registration includes anatomical and geometrical landmarks, curves, surfaces and voxel/pixel intensity values. The similarity function I is defined in a way that the distance between fiducial markers, curves, or surfaces in the transformed template image $T[\mathbf{u}]$ and the reference image R is minimized at its optimal point. In purely intensity-based methods, voxel/pixel intensity information in the images is compared through a similarity/distance measure. Various similarity/distance measures have been developed for single and multi-modality image registration problems among which SSD, CR, NCC, MI, and MIND are considered in this thesis and will be defined later in the the thesis.

The transformation $\mathbf{u}$ can be rigid or non-rigid. Different non-linear functions could be employed to match image spaces. Non-linearity makes the problem of image registration more complex and ill-posed. The optimal value for $\mathbf{u}$ in (2.1) has to result in a *realistic* transformation or deformation. Registration problems especially those based on image intensity often have more than one solution. A case example is shown in Figure 2.5. Landmark-based registration (matching a→a, b→b, and c→c) would give a single solution for this problem which is a translation from bottom-left to top-right of the template (T) image. However, intensity-based registration would give two more solutions for the problem. These solutions include a rotation (120, or 240 degrees) around the center and then a translation which basically are all rigid transformations. In non-rigid registration, more complex transformation functions would provide solutions many of which may be

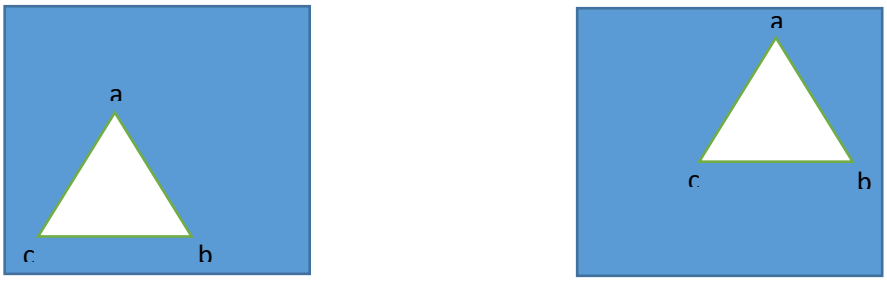

(a) Template (T) (b) Reference (R)

Figure 2.5: An example of an ill-posed image registration problem.

physically non-realistic.

To achieve reasonable and realistic solutions, the problem of image registration can be constrained based on the physical and geometrical properties of the body. For instance, the constraint in the example of Figure 2.5 can be in the form of a penalty function on the rotational parameter. These constrains can be mathematically formulated and added to the equation (2.1) as

$$\underset{\mathbf{u}}{\text{minimize}} \quad J(\mathbf{u}) = I(R, T[\mathbf{u}]) + \gamma S(\mathbf{u}); \quad \gamma \in \Re_+ \tag{2.2}$$

where $S(\mathbf{u})$ is called the regularization function. γ balances the importance of the regularization term compared to the similarity/distance measure. The cost function in Equation (2.2) can be minimized using different numerical or analytical optimization methods to find the optimal mapping (transformation) function $\mathbf{u}$ between images. The final step of the registration is to apply the mapping function to the template image in order to align with the reference image. An appropriate interpolation technique has to be employed to compute the transformed image in non-integer coordinates.

Based on what was discussed in this section, in majority of registration methods, the

following questions need to be addressed.

1. *Nature of registration basis*: The nature of registration basis needs to be determined based on the modalities and dimensions of the reference and template images. In feature-based registration, correspondence between identified landmarks has to be established. These methods are suitable for images with enough distinctive and detectable features. Surfaces, structure, and curves also need especial descriptors to be mapped in two images. However, extracting these features and landmarks can be difficult especially in multi-modal images and often needs manual data extraction by the radiologist.

   Intensity-based similarity/distance metrics often require no preprocessing. However, care needs to be taken in selecting the similarity/distance measure suitable for image registration considering the image modality and the tissue. Intensity-based similarity/distance measures for intermodality image registration are subject of active research.

2. *Mapping function*: Mapping function depends on the tissue and the nature of mismatch between images. Rigid transformation is more suitable for bony and stiff structures such as pelvis and femur. Nonlinear mapping functions and deformable models can be used for non-rigid registration of images acquired from soft tissues such as breast, liver, prostate and brain.

3. *Regularization*: The regularizer term in (2.2) is intended to make the registration problem well-posed, i.e., to ensure the existence of a unique solution preferably through a convex cost function. However, excessively restrictive regularizers may lead to an unfavorable registration.

4. *Interpolation methods and optimization*: Smoothness of the cost function depends on image resampling and interpolation techniques used. The method of optimization needs

to be determined in conjunction with the interpolation technique and the employed regularizer. A trade-off between the computational complexity and the accuracy of the interpolation technique should also be considered depending on the application.

The remainder of this chapter surveys different registration methods and touches upon various aspects of the problem.

2.3 Basis of Registration

2.3.1 Registration based on Extrinsic Properties

In the registration methods based on extrinsic properties, artificial objects which are detectable in both pre and intraoperative images are attached to the patient's body. Stereotactic frame systems usually use a "V" or "N" shape markers rigidly screwed to the patient's outer skull [45, 46]. This system, if enough cross-section of the markers are visible in the tomographic images, can relate the image space to the physical coordinate space during neurosurgery. Screw-mounted markers are other invasive objects that are used for the registration of images from different modalities [47, 48]. Skin markers, which are affixed to the patient's skin, are less invasive than to screw-mounted markers. In [49], external reference markers are used for the correction of head rotation in brain single-photon emission tomography. In [50], fiducial skin markers taped to the surface of the breast to help track its movement and deformation.

Most extrinsic methods employ rigid or affine transformation for point-to-point registration and do not utilize patient related image information. As a result, the registration parameters can be computed explicitly and there is no need for complex optimization methods. Furthermore, extrinsic markers can be designed such that they can be identified

automatically in multiple modality images. The distance between corresponding markers after registration is called "fiducial registration error" (FER). It has been shown that this error is proportional to the "fiducial localization error" (FLE), i.e., the error in determining the position of markers [51, 52], which is typically half the size of pixels/voxels for extrinsic landmarks [53]. Since extrinsic methods are often invasive and are constrained with rigid motion transformations, their application is usually limited to brain and orthopedic imaging [54].

2.3.2 Landmark-based Registration Methods

Landmark-based registration relies on salient points called "anatomical landmarks" or "fiducials" identified from the intrinsic image content. The points are typically outstanding features of an image, e.g., the point of maximal curvature, center of a lesion, corners, and the bifurcation point of vessels. Identifying the location of landmarks in two sets of images is a sophisticated task especially in multimodal images, and requires an expert's manual intervention. Identified matching landmarks in two set of images can be registered using either a least squares fit or an interpolation function [55]. To find the least-squares fit, Evans *et al.* [52] used the method of singular value decomposition (SVD) to register PET and MR brain images. The same method was used by Hill *et al.* [56] to register CT and MR skull base images. Although landmark-based methods are mostly employed for finding rigid or affine transformations, they can also be instrumental in finding more complex transformations provided that a large set of points are identified. In [57], first and second order polynomials are used for landmark-based registration of abdominal MR images. In order to constrain the problem and reduce the number of degrees of freedom in the deformation field, basis functions are employed to form a mathematical deformation model. In [58],

a landmark-based registration method using Gaussian radial basis functions (RBF) as a regularizer is proposed, which ensures the smoothness and invertibility of the transformation. In this method RBF coefficients are calculated by solving a system of linear equations rather than using a numerical optimization approach. Also, Rohr *et al.* [59] elastically registered brain MR images using thin-plate spline approximation based on anatomical landmarks. Various smooth landmark-based registration schemes with numerical methods are explained in [23, 60].

To assess the accuracy of intrinsic landmark-based methods, distances between corresponding landmark points after registrationis are measured. These points are different from those which are used for the registration and are called "targets". The registration error is also called "target registration error" (TRE). TRE is proportional to FLE and is inversely proportional to the square root of the number of fiducials used for the registration [47]. FLE for intrinsic landmarks is roughly twice the size of pixels/voxels which is larger than that of extrinsic landmarks. Therefore, to reduce the TRE, the number of intrinsic fiducials has to be increased.

2.3.3 Registration based on Curves and Surfaces

Curves, planes, and surfaces extracted from images can also be used as matching bases in image registration. These features are obtained automatically or semi-automatically in a step prior to the registration. Ayache *et al.* [61] used crest lines on the object surfaces to match 3D CT skull images. They extracted the crest lines by computing up to third order derivatives of the image intensity function and approximated them by spline curves to compute a number of differential invariants at each point. They claimed that the crest lines are stable with respect to rigid transformation and the registration method is accurate and

robust. In [62] an open curve matching method is proposed to match 2D curves which do not have well-defined end points. First, the overlap between corresponding curves is determined based on a search algorithm on the local curvatures and then a number of point pairs are generated that are used in a direct point-to-point matching algorithm. Furthermore, Charnoz *et al.* [63] proposed a tree matching algorithm for intra-patient vascular system based on registering edges and nodes extracted from liver CT images.

The surfaces of organs are anatomical structures which can be extracted from multimodal images and used in image registration. Extracted surfaces are widely used to form rigid and deformable models in different applications. The "head-hat" method proposed by Chen, Pelizzari and others [64–67] is one of the successful surface-based registration methods which currently is in clinical use. This method registers CT, PET, and MRI tomographic images of the brain. In this method, a surface model called "head" is extracted from images based on the head surface. This model is registered iteratively to a set of points called "hat" extracted from contours in the other image using a rigid or affine transformation. Some user involvement may be required to improve segmentation performance and avoid local minina in the search algorithm. In [68], Chow *et al.* formulated surface registration of human skull and vertebra as an optimization problem and solved it by a dynamic genetic algorithm. An algorithmic overview of surface registration techniques in medical imaging is given in [69]. It should be noted that the performance of these registration algorithms depends on the accuracy of the image segmentation method used.

Although the application of surface registration is well established in brain and orthopedic imaging, these same methods are not applicable to soft tissue imaging. However, deformable models based on segmented edges and surfaces are used in image registration. These models are constructed based on geometrical information obtained from one image

and using elastic deformation formulation. The template model is then deformed to match the other image. Ferrant *et al.* [29, 70] used a deformable surface matching algorithm for non-rigid registration of 3D MR images of the brain. They iteratively deformed the surface model based on preoperative 3D images to match cortical surface and the lateral ventricles in intraoperative image sequences showing brain shift. Then, they obtained a volumetric deformation field from displacements at the boundary surfaces using a linear elastic FE model. A surface model-based deformable registration method was also developed by Kaus *et al.* [71] to register 3D CT images of the lung and liver images in radiation therapy planning. They segmented both pre and intraoperative images and constructed 3D triangular surface meshes. Based on the deformation obtained for certain vertex points in the meshes, they employed various interpolation methods to estimate the volumetric deformation field.

2.3.4 Registration based on Image Intensity

Voxel/pixel intensities can be directly used for image registration with no prior feature identification. The principal-axes or moment-based method introduced by Alpert *et al.* [72] is an example of image intensity-based registration which employs reduced information rather than the whole image voxels/pixels data. In this method, registration is carried out by aligning the image centers of mass and their principal orientations (axes). The center of mass and principal axes are image zeroth and first-order moments respectively [73]. Although matching principal axes provides exact registration for an object with a rigid transformation (rotation and translation), for non-rigid objects this method may result in an approximate solution. Moments computed for segmented binary volumes produce acceptable results in many applications.

Intensity-based methods using whole image content are widely popular in various medical applications. At the expense of computational cost, these methods employ all available image information; they can be applied to single and multiple modality images using any type of transformation. A similarity/distance metric can be directly computed from the image voxel/pixel gray-scale values or indirectly, e.g., image gradients, which are derived from the image intensity content. Some of the widely used similarity/distance metrics as well as most recently developed intensity-based measures are briefly reviewed here.

• *Measures based on intensity differences*

Comparing two images, an intuitive and simple measure of similarity/distance measure is the difference of image intensities. Sum of squared differences (SSD) between images is one of the simplest similarity/distance measures which is minimized in the registration process. The average SSD between the reference (R) and the transformed template image ($T[\mathbf{u}]$) is defined as follows

$$\mathrm{SSD}(\mathbf{u}) = \frac{1}{n}\sum_{i=1}^{n}\Big(R_i - T_i[\mathbf{u}]\Big)^2 \tag{2.3}$$

where n in the number of voxels/pixels in the overlap area between images. Viola in [74] showed that SSD is an optimum measure when the only difference between images after registration is additive Gaussian noise. This restricts the application of this metric to single modality images. SSD is widely used for the registration of MR images [8, 75]. The definition of distance measure in (2.3) makes it highly sensitive to a small number of voxels/pixels which have a large intensity difference in two images (e.g., because of the contrast agent). This effect can be mitigated using the sum of absolute differences (SAD) defined

as [76]

$$\mathrm{SAD}(\mathbf{u}) = \frac{1}{n}\sum_{i=1}^{n}\left|R_i - T_i[\mathbf{u}]\right| \tag{2.4}$$

• *Measures based on correlation techniques*

A quick method to approximately evaluate the degree of dependence between two images assuming their intensity values as random variables is to compute their correlation coefficient (CC). In case image intensities in two images have a linear relationship, CC would provide the optimum similarity/distance metric. The CC is defined as

$$\mathrm{CC}(\mathbf{u}) = \frac{\mathrm{Cov}(R, T[\mathbf{u}])}{\sqrt{\mathrm{Var}(R)\mathrm{Var}(T[\mathbf{u}])}} = \frac{\sum_{i=1}^{n}(R_i - \overline{R})(T_i[\mathbf{u}] - \overline{T}[\mathbf{u}])}{\sqrt{\sum_{i=1}^{n}(R_i - \overline{R})^2 \sum_{i=1}^{n}(T_i[\mathbf{u}] - \overline{T}[\mathbf{u}])^2}} \tag{2.5}$$

where Var and Cov represent variance and covariance, and $\overline{R}$ and $T[\mathbf{u}]$ are the mean voxel/pixel intensity value in the reference and transformed template images. Since CC measures linear dependency between variables, it is mostly used in intramodality registration [77, 78]. Kaneko *et al.* [79] computed CC for selective voxels/pixels in order to match images under ill-conditioned illumination or partial occlusion.

Correlation ratio (CR) as a similarity measure between images is a measure of functional dependence between them and was introduced by Roche *et al.* [80, 81]. CR between two images is defined as [80]

$$\mathrm{CR}(\mathbf{u}) = \frac{\mathrm{Var}[\mathrm{E}[T[\mathbf{u}] \mid R]]}{\mathrm{Var}[T[\mathbf{u}]]} \tag{2.6}$$

where Var[E[$T[\mathbf{u}] \mid R$]] is the variance of the conditional expectation E[$T[\mathbf{u}] \mid R$] and measures the part of $T[\mathbf{u}]$ which is predicted by R. Equation (2.6) can intuitively be explained

as the portion of energy in $T[\mathbf{u}]$ which is explained by R. In [82], CR is generalized to take into account the nature of US images. They used a modulus of the MR image gradient as an additional explanatory variable in registering preoperative MR images of the brain to its 3D intraoperative US images. CC and CR are both bounded between 0 and 1 (1 for the perfect match) and both metrics are available in most image registration software packages.

• *Information theoretic measures*

A statistical relationship might be an alternative to the functional dependency between images which sometimes happens to be too restrictive. In 1948, Shannon *et al.* [83] introduced a measure of uncertainty for an event, called "Shannon entropy". For a variable X occurring n times with probabilities $p_1, ..., p_n$, Shannon entropy is defined as

$$\mathrm{H} = -\mathrm{E}_X[\log(p)] = \sum_{i=1}^{n} -p_i \log(p_i) \tag{2.7}$$

The Shannon entropy can be computed for an image to measure the distribution of the gray values of the image. Basically, the entropy of an image represents the amount of information a gray value of the image as an event provides when it takes place and the uncertainty about the outcome of that event [84]. It also tells how disperse the probabilities of the gray values are. Assuming template T and reference R images as random variables, the dependency between them can be defined based on their conditional and joint entropy defined as follows [74]

$$\mathrm{H}(T \mid R) = \mathrm{E}_R[\mathrm{E}_T[log(p(T \mid R))]] \tag{2.8}$$

$$\mathrm{H}(T, R) = \mathrm{E}_R[\mathrm{E}_T[log(p(T, R))]] \tag{2.9}$$

where conditional entropy in (2.8) is a measure of the randomness of T given information about R. Joint entropy can be expressed in terms of marginal and conditional entropy as follows

$$\mathrm{H}(T\ ,\ R) = \mathrm{H}(T \mid R) + \mathrm{H}(R) \tag{2.10}$$

As T becomes more dependent on R, $\mathrm{H}(T \mid R)$ becomes smaller. However, a small value of $\mathrm{H}(T \mid R)$ may not necessarily imply dependency of T and R, since it could be due to a small $\mathrm{H}(T)$ [74]. "Mutual information" (MI) between two images, which is a measure of reduction in the entropy of T given R is defined as

$$\mathrm{MI}(T,R) = \mathrm{H}(T) - \mathrm{H}(T \mid R) = \mathrm{H}(T) + \mathrm{H}(R) - \mathrm{H}(T,R) = \mathrm{MI}(R,T) \tag{2.11}$$

The last equality in (2.11) implies that minimizing the joint entropy would result in maximizing the MI between images. MI based on the joint marginal probability distribution of images is defined as [84, 85]

$$\mathrm{MI}(R,T) = \sum_{r,t} p(r,t) \log \frac{p(r,t)}{p(r)p(t)} \tag{2.12}$$

MI and joint entropy need to be computed in the overlapping area between images and as a result both are sensitive to the size and contents of the overlap. However, since MI is comprised of marginal entropies $\mathrm{H}(T)$ and $\mathrm{H}(R)$, it is less sensitive to overlapping region than joint entropy [86]. Studholme *et al.* [87] showed that with increasing missregistration as a result of decreasing overlap, the MI measure may increase. This happens when the sum of marginal entropies increases faster than the joint entropy. They proposed normalized

mutual information (NMI) defined as

$$\mathrm{NMI}(R,T) = \frac{\mathrm{H}(R) + \mathrm{H}(T)}{\mathrm{H}(R,T)} \tag{2.13}$$

which is less sensitive to changes in the overlap region. NMI takes values between 0 and 2 where the upper bound happens when two images are identical. It should be noted that CC, CR, MI and NMI are similarity measures and are maximized during the registration process. Therefore, their values with a negative sign have to be used in the formulation of Equation (2.2).

Mutual information is probably the most widely used intensity-based similarity metric especially for multimodal image registration in the literature. Rueckert *et al.* [88] non-rigidly registered contrast enhanced breast MRI images using NMI. Luan *et al.* [89] proposed a quantitative-qualitative measure of MI (Q-MI) for multimodal image registration. The new similarity measure considers both image intensity distribution and the utility of voxels [89]. They claimed that, Q-MI based registration is more robust compared to the conventional MI-based methods and provides a smoother cost function with a relatively large capture range in rigid registration of the brain MR, CT and PET images. MI-based rigid and non-rigid registrations of US volumes obtained from abdominal and thoracic organs were also investigated in [90]. Furthermore, Tomazevic *et al.* [91] added spatial information in the form of local intensity changes to a global intensity matching function based on MI. They tested the proposed similarity measure in the registration of spine MR-CT images as well as brain MR-PET images.

It has been reported in several articles that MI and NMI result in reliable outcome if the overlapping region provides enough information about the images. Andronache *et al.* in [92] showed that MI does not produce reliable results for small-sized images and

local image patches. They also reported that local joint intensity histogram of sub-images allows more robust and computationally efficient correlation coefficients (CC) for image matching. Also, Roche *et al.* [80] showed that correlation ratio (CR) is more robust than mutual information in rigid registration of MR, CT and PET low-resolution images.

• *Other intensity-based similarity/distance measures*

Developing a comprehensive intensity-based similarity/distance measure applicable to multimodality image registration is still a challenge and there is no universal metric which can be applied for all types of image registration problems. The problem becomes even more challenging when one of the images contains artifacts and has lower signal to noise ratio (SNR), e.g., in US imaging. In addition to the similarity/distance measures discussed above, quite a few other metrics have been developed in recent years most of which are application dependent and can be applied only to specific image modalities. Roche *et al.* in [93] developed a similarity measure generalizing CR to incorporate multivariate information from the preoperative MR data. They used the gray value for each voxel along with the intensity gradient at each point to estimate a polynomial function to compute the remapped MR image data. Then, they registered a remapped MR to intraoperative US images based on CR. In [94], Haber *et al.* instead of using the gray value at each point, computed the normalized gradient of the image to derive intensity change at each point. In order to align images, they minimized the norm of the cross-product or maximized the square of the dot-product between gradients in two images. The proposed similarity/distance measure was employed for the registration of MR T1 and T2 brain images in [94] and for the registration of 3D CT and US liver images in [95].

Adding structural and spatial information to image intensities in the computation of similarity/distance measures has also been investigated before. Loeckx *et al.* [96] proposed

a similarity measure called "conditional mutual information" (cMI) using a 3D histogram incorporating intensity dimensions in two images as well as a spatial dimension expressing the location of the joint intensity pair. They showed that cMI outperforms the classical MI specially in non-rigid registration. A deformable registration via attribute matching and mutual-saliency (DRAMMS) weighting for multimodal image matching was proposed in [97]. DRAMMS renders each voxel by a set of multi-scale and multi-resolution attributes which reflect the anatomical and geometric context around the voxel. Moreover, DRAMMS assigns higher weights to those voxels having higher ability to establish correspondence between images using weighting maps called "mutual saliency". More recently, Heinrich *et al.* [98] proposed an intensity-based similarity/distance metric called modality independent neighbourhood descriptor (MIND). MIND is based on similarity of small image patches and compares distinctive structures in a local neighbourhood. This makes MIND independent from image modalities. Simple image similarity/distance metrics such as SSD [98] or CC [99] can be employed to compare locally extracted descriptors in two images. In this thesis, MIND is used in the registration of 3D preoperative MR images to 2D real-time US images of a realistic breast phantom. This similarity/distance measure will be discussed in details in Chapter 7.

2.3.5 Registration based on Frequency Domain Analysis

Several properties of the Fourier transform such as translation, rotation, reflection, and scaling can be exploited and utilized in image registration. Image information in the frequency domain can be utilized to register multiple images. Although frequency domain-based methods are more robust than intensity-based methods with respect to disturbances

and frequency-dependent noises, they are only applicable to images with rigid misalignment [100]. De Castor *et al.* [101] proposed a frequency-based technique for the registration of images which are translated and rotated with respect to each other. Liu *et al.* [102] introduced a method for matching images with large non-overlapping field of view. They rigidly aligned images with matching dominant local frequency image representations. A robust scale-invariant image registration method based on fast fourier transform (FFT) was also presented in [103]. This method estimates relative translation, rotation and scaling parameters using FFT-based correlation.

2.4 Transformation/Mapping Functions

The geometric relationship between voxels/pixels in two images is modeled through "transformation function". The transformation function not only takes into account the physical movement and deformation of the imaged object, but also deals with any possible geometric distortion between images. If there is no distortion in the images and the imaged object is rotated and translated, a *rigid* transformation function can be used to map two images. Such a function mapping image coordinates 1 to image coordinates 2 in 2D can be written as

$$\begin{bmatrix} x_2 \\ y_2 \end{bmatrix} = \begin{bmatrix} \cos\theta & -\sin\theta \\ \sin\theta & \cos\theta \end{bmatrix} \begin{bmatrix} x_1 \\ y_1 \end{bmatrix} + \begin{bmatrix} t_x \\ t_y \end{bmatrix} \tag{2.14}$$

where t_x and t_y are translations along the x and y directions respectively, and θ is the rotation angle about the axis perpendicular to the image plane. With rigid transformation, the overall geometric relationship between points do not change, i.e., angles and lengths are preserved.

The rigid transformation function for 3D images is comprised of three translational

parameters along three axes, i.e., t_x, t_y, and t_z as well as three rotational parameters around those axes, i.e., θ_x, θ_y, and θ_z. The rigid 3D transformation maps two coordinates as follows

$$\begin{bmatrix} x_2 \\ y_2 \\ z_2 \end{bmatrix} = R(\theta_x, \theta_y, \theta_z) \begin{bmatrix} x_1 \\ y_1 \\ z_1 \end{bmatrix} + \begin{bmatrix} t_x \\ t_y \\ t_z \end{bmatrix} \tag{2.15}$$

where $R(\theta_x, \theta_y, \theta_z)$ is a 3×3 matrix computed as

$$R(\theta_x, \theta_y, \theta_z) = \begin{bmatrix} \cos\theta_z & -\sin\theta_z & 0 \\ \sin\theta_z & \cos\theta_z & 0 \\ 0 & 0 & 1 \end{bmatrix} \begin{bmatrix} \cos\theta_y & 0 & \sin\theta_y \\ 0 & 1 & 0 \\ -\sin\theta_y & 0 & \cos\theta_y \end{bmatrix} \begin{bmatrix} 1 & 0 & 0 \\ 0 & \cos\theta_x & -\sin\theta_x \\ 0 & \sin\theta_x & \cos\theta_x \end{bmatrix} \tag{2.16}$$

Rigid transformation is often used for the registration of images obtained from bony structures such as skull [82] and vertebra [104]. In non-rigid registration methods, a rigid transformation based alignment is usually performed first to bring the images as close as possible prior to the application of the deformable registration galgorithm. Rigid registration can also provide fast and robust results for images of non-rigid tissue with small deformation [105, 106].

Affine transformation is the simplest non-rigid mapping function which can account for other spatial distortions such as shearing and scaling [107, 107]. The general 2D affine transformation is defined as

$$\begin{bmatrix} x_2 \\ y_2 \end{bmatrix} = \begin{bmatrix} a_{11} & a_{12} \\ a_{21} & a_{22} \end{bmatrix} \begin{bmatrix} x_1 \\ y_1 \end{bmatrix} + \begin{bmatrix} t_x \\ t_y \end{bmatrix} \tag{2.17}$$

The affine transformation in 3D has 12 parameters which accounts for rigid body transformations, shears and aspect ratio changes (scaling) as follows

$$\begin{bmatrix} x_2 \\ y_2 \\ z_2 \end{bmatrix} = \begin{bmatrix} a_{11} & a_{12} & a_{13} \\ a_{21} & a_{22} & a_{23} \\ a_{31} & a_{32} & a_{33} \end{bmatrix} \begin{bmatrix} x_1 \\ y_1 \\ z_1 \end{bmatrix} + \begin{bmatrix} t_x \\ t_y \\ t_z \end{bmatrix} \tag{2.18}$$

With this transformation, angles and lengths are no longer preserved but straight lines parallelism remains unchanged. Affine registration can also be employed for initial alignment of medical images prior to deformable registration. Rather than using a global transformation, multiple affine transformations can be employed locally to non-rigidly register images. This technique is called piecewise affine registration where local affine transformations are embedded in a deformable or elastic model to ensure smoothness of the deformation [108–110].

Projective transformation is another non-rigid transformation which accounts for the distortion related to projected images. Projective transformation mapping coordinates 1 to coordinates 2 in 2D is defines as [111]

$$x_2 = \frac{a_{11}x_1 + a_{12}y_1 + a_{13}}{b_1x_1 + b_2y_1 + b_3} \tag{2.19}$$

$$y_2 = \frac{a_{21}x_1 + a_{22}y_1 + a_{23}}{b_1x_1 + b_2y_1 + b_3} \tag{2.20}$$

When a 3D scene is projected through an optical imaging system to a 2D plane, the resulting distortion is called *perspective*. Perspective transformation from 3D to 2D can be expressed

as

$$x_2 = \frac{a_{11}x_1 + a_{12}y_1 + a_{13}}{b_1x_1 + b_2y_1 + b_3z_1} \tag{2.21}$$

$$y_2 = \frac{a_{21}x_1 + a_{22}y_1 + a_{23}}{b_1x_1 + b_2y_1 + b_3z_1} \tag{2.22}$$

where a and b terms are determined based on the registration method. In the projective and perspective transformations parallelism in lines and angles are not preserved, but straight lines are still straight. A 3D-2D projective registration method is proposed in [112] to register free-form curves and surfaces.

Transformation functions that map straight line to curves are called *curved* or *deformable* transformations. In 2D, this type of transformations can be formulated as

$$\begin{bmatrix} x_2 \\ y_2 \end{bmatrix} = \begin{bmatrix} f(x_1, y_1) \\ g(x_1, y_1) \end{bmatrix} \tag{2.23}$$

where $f(.)$ and $g(.)$ are nonlinear functions mapping the two coordinates. Polynomial functions are examples of global transformation functions which are used in non-rigid registration of medical [113] and airborne images [114]. Most nonlinear transformation functions in the literature are inspired from the interpolation theory [115]. In this theory, displacements of image voxels/pixels are interpolated using an interpolation function based on a limited set of known displacements. Using this concept, the transformation function approximates the known displacements having low degrees of freedom, which facilitates parameters inference. Radial basis functions (RBFs) are widely used for interpolation strategies. Using RBFs, the displacement at point $\mathbf{x}$, i.e., $\mathbf{u}(\mathbf{x})$ is given as a linear combination of

translated radially symmetric functions plus a low-degree polynomial as

$$\mathbf{u}(\mathbf{x}) = \mathrm{A}\mathbf{x} + \mathbf{t} + \sum_{i=1}^{N} \omega_i \phi(||\mathbf{x} - \mathbf{p}_i||) \tag{2.24}$$

where $\phi(.)$ is called the basis function centered at the known sample points $\mathbf{p}$. These sample points are often called "control points". A comprehensive study of RBFs in non-rigid image registration is given in [116]. RBFs are able to interpolate image displacements based on known displacements at irregular control points. However, similar to polynomial functions, RBFs give global deformation field, i.e., the deformation at one control point affects points in the whole image.

Thin-plate splines (TPS) [117] are the most popular form of RBFs. The radial basis term of TPS in 2D is in the form of

$$\phi(||\mathbf{x} - \mathbf{p}_i||) = ||\mathbf{x} - \mathbf{p}_i||^2 log(||\mathbf{x} - \mathbf{p}_i||) \tag{2.25}$$

It takes a simpler form in 3D as [117]

$$\phi(||\mathbf{x} - \mathbf{p}_i||) = ||\mathbf{x} - \mathbf{p}_i||. \tag{2.26}$$

TPS can be interpreted as a very thin plate which is fixed at control points in the reference image. The TPS minimizes the bending energy of the whole image and the solution can be obtained in a closed-form [115]. TPS-based registration with infinite boundary condition provides a global support. Jing *et al.* [118] proposed a compact support TPS algorithm to improve registration of local deformations. Furthermore, an extension of TPS-based registration was proposed in [119] to control the spatial influence of acting forces and thus

the locality of the transformation. It should be noted that the transformations obtained based on TPS defined in (2.25) or (2.26) from one image domain to another are not inverse consistent. Marsland *et al.* [120] proposed polyharmonic clamped-plate splines which minimize the same energy as TPS under specific boundary condition; but, the resulting dense deformation is diffeomorphic.

Gaussian functions are other RBFs that are used for approximating deformation as

$$\phi(||\mathbf{x}-\mathbf{p}_i||) = e^{-\frac{||\mathbf{x}-\mathbf{p}_i||^2}{\sigma^2}} \tag{2.27}$$

where σ controls the spatial influence of the Gaussian kernel. Shen *et al.* [121] used Gaussian functions to approximate elastic deformation in the registration of brain MR images based on matching geometric moment invariants. Another family of RBFs providing global support is called multi-quadratics [122] and is defined as

$$\phi(||\mathbf{x}-\mathbf{p}_i||) = \left(||\mathbf{x}-\mathbf{p}_i||^2 + d^2\right)^{\frac{\mu}{2}} \tag{2.28}$$

Here d controls the smoothness of the deformation and μ is a non-negative scalar.

Free-form deformation (FFD) is another type of transformation models which first was proposed by Rueckert *et al.* [8] for non-rigid registration of breast MR images. While the global motion of the breast is modeled by an affine transformation, the local deformation is described by a FFD based on B-splines. In this method, a 3D grid of control points with uniform spacing is superimposed on the image and the dense deformation of the image is formulated as a summation of tensor products of univariate splines [8]. Using this model of deformation, the displacement in the control points only affects the local neighbourhood of

the point which makes it suitable for capturing local deformations with few degrees of freedom. Rueckert *et al.* developed a diffeomorphic registration method based on FFD in [77], ensuring that individual B-spline-based deformations are one-to-one transformations. FFD models are well established and have been frequently used in non-rigid image registration applications in the past [123–125]. In order to improve their accuracy, the number of control points needs to be increased which increases the computations. Implementation of registration algorithms on graphics processing units (GPUs) is a promising approach for speeding up their computations [126].

2.5 Regularization Methods

Ill-posed mathematical problems have a very old history. Despite Hadamard's belief [127] that ill-posed problems could not happen in physical systems, nowadays they in fact can arise in many areas of science and engineering. Image registration is usually ill-posed and needs regularization in order to obtain a reasonable solution [23] and prevent folds and tears in images.

The problem of registering two images is formulated as a regularized minimization of a similarity/distance measure between images in (2.2). Using the concept of calculus of variations, the objective function can be minimized by solving a nonhomogeneous system of differential Equations [128, 129]. The variational derivatives of the regularizer provide the partial differential equations. Driving forces in the Euler-Lagrange equations are also the results of variational derivatives of the similarity/distance measure [129]. Various regularizers have been reported in the literature for non-rigid image registration. The choice of regularizer depends on the application, similarity/distance measure, and available boundary conditions for the problem. A group of standard regularizers used in nonparametric

image registration and their partial differential operators are given in [129]. Modersitzky [23, 60] discusses numerical implementation of L_2-norm based regularizers some of which are reviewed here.

The diffusion regularizer proposed in [130] measures variations in the displacement field $\mathbf{u}$ and is employed for the registration of brain MR images [131]. Curvature regularizer [132] is based on second-order derivative of the displacement field $\mathbf{u}$ and has been used for non-rigid registration of brain MR images [133] and MR mammography images [134]. Elastic regularizer, which is probably the most commonly used regularization term in image registration, measures the energy resulted from deforming an elastic material [135]. It should be noted that in diffusion and curvature regularizers, the regularization energy is sum of independent energies on each coordinate of the transformation. But, in the elastic regularizer, the coordinates are dependent, and the regularization strength as well as the coupling between coordinates are controlled by two parameters [129, 136]. Fluid regularizer [137] is the same as elastic regularizer in formulation, but in fluid models the strain depends on the rate of change in the displacement field. In other words, while elastic models are characterized by the spatial smoothing of the displacement field, fluid models are defined by the spatial smoothing of the velocity field [23, 129].

2.6 Interpolation Methods and Optimization

In image registration algorithms, the template image is transformed to match the reference image through a backward mapping. The forward mapping which transforms each voxel/pixel of the template image is complicated to implement and may produce holes or overlaps in the transformed image. In backward mapping, the regular grid of the reference image is transformed to the coordinates of the template image using the inverse of the

estimated transformation function. Gray-scale values at transformed grid points form the transformed template image. The transformed grid points do not necessarily match with the template image grid, thus an interpolation technique has to be employed.

Comparative investigations on different image interpolation methods are given for 2D and 3D images in [138] and [139] respectively. The nearest neighbour [60], bilinear (trilinear in 3D) and bicubic [60], quadratic splines [140], cubic B-splines [60, 141], Gaussians [142] and truncated *sinc* functions [141, 143] are some of the most commonly used interpolation functions. Lehmann *et al.* [144] performed a detailed spatial and Fourier analysis on different interpolation methods and compared their computational complexity as well as qualitative and quantitative interpolation errors. Ideally, based on Shannon's information theory, any band-limited function can perfectly be interpolated by *sinc* functions. However, medical images are not band-limited. Furthermore, *sinc* function is infinite in extent and is hard to be implemented in practice even for band-limited functions. Although truncating the *sinc* function is a solution to this problem [143], truncation blurs the image and causes ringing effect in the frequency domain.

Spline functions have been used to approximate the *sinc* function because of their ease of implementation. The kernel for B-spline approximator is spatially unlimited, thus B-spline interpolator acts like an infinite impulse response (IIR) filter [144]. There is a consensus agreement in the literature that, among all interpolation methods, B-spline interpolation offers the best trade off in terms of similarity to the original image and computational efficiency. Cubic (third order) B-spline interpolator is the most widely used spline function and has sufficient accuracy for many practical applications [145]. Bilinear/trilinear interpolation, however, is the most commonly used interpolation method in medical image processing. In this method a pixel (voxel) value in the transformed image is estimated by a

weighted average of four (eight) nearest neighbours in the original image. Although other higher order approximation methods outperform bilinear interpolation in terms of accuracy, this method represents a good trade-off between accuracy and computational complexity.

Optimizing strategy is very important in both parametric and non-parametric optimization-based registration methods. Despite choosing appropriate similarity/distance measure, transformation function, regularizer, and interpolation method, optimizing the cost function might result in irrelevant outcome. There might be multiple optima within the parameter space because, as was discussed before, the image registration problem is not a well-posed problem. Furthermore, iterative optimization algorithms may be trapped in local minimum points. These points may be caused by local matching between image features and intensities. Pluim *et al.* [86] showed that in the MI-based registration, bilinear and partial volume interpolation [146] methods can cause multiple local minima in the cost function. They demonstrated that this artifact occurs when the corresponding voxel sizes of the images are identical or are multiples of each other. They also showed that resampling the images would solve this problem. Starting from multiple initial values for parameters and blurring (smoothing) images can be effective in avoiding local minima in the optimization procedures. Multilevel or multiresolution optimization is also another approach to mitigate the effect of image artifacts [146]. In this framework, optimization starts with low-resolution images which yields a smooth cost function. Higher resolution images are employed when the solution closer to the global minimum point. A review of various optimization methods used in image registration is given in [147]. Since MI is the most widely used similarity measure for multimodal images, many optimization techniques have been developed for registration based on maximizing this metric [146, 148, 149].

2.7 Deformable Model-based Registration Methods

Deformable models have been widely investigated in computer-assisted medical image analysis. These models combine geometry, physics and material properties of the object to approximate its behaviour under environmental forces. They are used in segmentation, registration, and tracking images of anatomical structures utilizing image-based constraints and *a priori* knowledge about the location, size, and shape of these structures [150]. As mentioned in Section 2.5, deformable models in image registration regularize the ill-posed problem by limiting the solution space to a large extent. The deformation model in image registration problems implies an important assumption about the nature of deformation to be estimated. Computational complexity and the richness of the deformation descriptor are other factors needed to be considered in selecting a deformation model for image registration.

A review of geometric transformation models for non-rigid image registration is given by Holden in [151]. More recently, Sotiras *et al.* [115] provided an overview of deformable registration methods together with most recent advances in deformable models and similarity/distance measures. The models are classified in two groups based on their theoretical foundation. The first group consists of models based on interpolation and approximation theory explained by basis function expansions. Radial basis functions, elastic body splines, free-form deformation models, basis functions from signal processing (wavelets) and piecewise affine models belong to this group. The second group includes physical models described by partial differential equations of continuum mechanics. Linear elastic models, viscous fluid flow models, diffusion models, curvature registration and flows of diffeomorphisms are also considered in this group [115]. Some of these models were briefly reviewed

in Sections 2.4 and 2.5. Elastic models are the most commonly used deformation models in medical image processing and particularly in image registration. The registration method developed in this thesis also employs a linear elastic deformation model discretized using FEM. Hence, some of the related registration methods based on elastic models are reviewed here.

Physical deformation models based on elasticity theory respond naturally to applied forces and constraints. Deformation energy which is defined based on the geometric degrees of freedom of the model grows monotonically as the model deforms away from its rest position. This energy, which is also called stress-strain energy, is induced by the external forces. In image registration, external potential energies are defined as similarity/distance measures between images. External forces derived from the similarity/distance measures deform the model such that it fits into the image data. Image registration is achieved when the external energy and the internal deformation energy of the model are balanced. In other words, the elastic energy regularizes the registration problem as defined in Equation (2.2). Therefore, the optimal deformation of the model is found by minimizing the objective function in (2.2).

The potential energy of a elastic body with deformation of $\mathbf{u}$ is defined as [23]

$$S(\mathbf{u}) = \int_{\Omega} \frac{\mu}{4} \sum_{i}^{d} \sum_{j}^{d} (\partial_{x_i} u_j + \partial_{x_j} u_i)^2 + \frac{\lambda}{2} (\nabla . \mathbf{u})^2 \, dx \tag{2.29}$$

Here $\nabla .$ is the divergence operator, d is the dimension of the model, Ω is the body of the image, and u_i is the i^{th} component of the displacement field $\mathbf{u}$. Moreover, λ is the so-called Lamé's first coefficient and μ quantifies the stiffness of the material [115]. The Euler-Lagrange equation corresponding to the linear elastic energy defined in (2.29) is given

by [23, 128]

$$\mu\nabla^2\mathbf{u} + (\lambda+\mu)\nabla(\nabla.\mathbf{u}) = -\mathbf{f} \tag{2.30}$$

where ∇^2 and ∇ indicate Laplacian and Gradient operators, respectively. Furthermore, $\mathbf{f} = \frac{1}{\gamma}\nabla I(R, T[\mathbf{u}])$ determines applied forces to the elastic body, and is proportional to the directional derivative of the similarity/distance measure. These equations are also called Navier-Cauchy [115] and Navier-Lamé [23] equations. The partial differential equations (PDEs) in (2.30) balances the external forces derived from the image similarity/distance metric with the internal stress, imposing smoothness constraints. This equation can be solved using variational [23, 60], finite difference [135], basis function expansions [152], Fourier transform [23], and finite element methods [153]. Linear elastic models become inaccurate in large deformations. To cope with this limitation, He and Christensen [154] proposed an inverse consistent registration method for locally large nonlinear deformations. They assumed that the images are taken from the same structures using the same imaging technique. Large deformation was estimated by concatenating a sequence of small deformation transformation which is regularized using a linear elastic continuum mechanics model.

Biomechanical elastic models are also of wide interest in medical image analysis. These models use anatomical and physiological properties of the tissue under consideration to estimate the deformation field of the tissue. FEM discretization of the continuum mechanics based model using elastic body deformation is the most popular physical model-based analysis in various medical applications. This method is more accurate and reliable than other simpler methods such as mass-spring modelling [155]. Estimating the material properties of the tissue, identifying the geometry of the object, and defining the boundary conditions

are three challenging tasks involved in the FEM-based modelling. Material properties can be roughly estimated based on a limited number of experiments. The deformable tissue may be modeled as a homogeneous material [29, 156, 157], or as heterogeneous consisting of different homogeneous tissues [13, 158, 159]. The geometry of the object may be defined based on segmentation of anatomical structures using automatic or semi-automatic methods. The segmented areas/volumes in the image domain are then appropriately meshed to construct the geometry of the model. Boundary conditions are often specified as displacement constraints for the segmented organ surfaces.

Biomechanical models based on FEM have been used for registration and image based deformation tracking of various soft tissues including brain, breast, liver, prostate and lung. In [30], multi-object deformation models have been developed for the abdominal region of the human body and have been used in image registration. FEM-based linear elastic deformation models have also been employed for the registration of endorectal coil MRI in prostate radiotherapy planning [31, 160] as well as for predicting respiratory motion of the lung tumor over a breathing cycle [161]. Ferrant *et al.* [27, 29, 70, 162] have investigated the use of FE-based elastic deformation models in the computation of brain shift and deformation in neurosurgery. In breast imaging, FE-based deformation models have been employed to predict mechanical deformations during MRI-guided biopsy or under external perturbations [28, 32, 163]. They have also been used for validation of non-rigid breast image registration methods [164] and co-registration of prone and supine breast images [165].

2.8 Registration of Preoperative 3D MR/CT images to Intraoperative 2D MR/CT or 2D/3D US Images

Registration of high-resolution preoperative 3D MR/CT images to one or a few interventional 2D MR/CT images could be instrumental in updating preoperative plans, localizing the target inside the tissue and tracking organs motion. Previously, Fei *et al.* [15] developed a slice-to-volume registration algorithm with application to radio-frequency thermal ablation of prostate cancer. They rigidly and independently registered 15 interventional MR image slices from transverse, sagittal, and coronal orientations to a preoperative MRI volume. In a similar work, Xu *et al.* [16] rigidly registered preoperative 3D CT images of the lung to intaroperative 2D CT fluoroscopy image series to infer the position of lesions outside the plane of the CT fluoroscopy images. Yaniv *et al.* [166] assessed the Thirions "demons" deformable registration method [131] in non-rigidly registering 3D CT volumes to simulated 2D CT fluoroscopy images. They used the insight toolkit (ITK) for implementation and found out that the method is not suitable for the task of 3D-2D registration, as in most cases the recovered displacements were less than 50% of the original displacements. Furthermore, Chandler *et al.* [18] corrected misaligned slices in multi-slice cardiac examination using a rigid slice-to-volume MR image registration. A slice-to-volume registration algorithm is also proposed in [25] for tracking the prostate motion in MR-guided prostate biopsy. Three orthogonal intraoperative MR images are acquired and rigidly registered to a high-resolution preoperative target planning MR volume.

The fusion of preoperative MR/CT images with real-time US images has also gained significant attention in recent years and several systems have been developed to provide such functionality, e.g., see [167, 168]. These systems are based on tracking the US probe

using an exterior localizer. The US image in a global coordinate frame is registered to the MR image coordinates using fiducial markers which are attached to fixed positions with respect to the object. Therefore, the corresponding image slice of the real-time US in the MR image volume can be interpolated and overlaid on the 2D US image. Such approach would be acceptable when the object is rigid and static with respect to the fiducial markers; however, human organs are mostly non-rigid and can move and deform due to external and internal forces. A closed-loop control system based on rigid transformations is proposed in [169] to compensate for the prostate motion in transrectal ultrasound (TRUS) guided needle biopsy. Furthermore, a combined statistical-biomechanical model-based approach is proposed in [157] to non-rigidly register 3D preoperative MR images with 3D TRUS images of the prostate.

Chapter 3

Linear Elastic Deformation Model for Image Registration

In this chapter, the dynamic FEM-based linear elastic deformation model is developed based on minimizing the elastic energy of the body. To reduce computational complexity, dynamical modes of the model are decoupled through a change of variables and fast vibrational modes are discarded.

3.1 Background and Motivation

Continuum mechanics based models of biological soft-tissue deformation are well established [27, 28, 32, 160, 163, 170]. Biological tissues in general exhibits a complex deformation behaviour which is best described by nonlinear models. Kyriacou *et al.* [10] proposed a biomechanical model of brain deformation based on FEM to register brain MR/CT images with tumor pathology. They estimated the deformation induced by the growth of tumors using a nonlinear elastic model. A subject-specific nonlinear FE-based biomechanical model is also proposed by Wittek *et al.* [171], to simulate needle insertion

into the brain. They used nonlinear FE procedures that account for large deformations and nonlinear strain-stress relationships. Furthermore, Bharatha *et al.* in [13] employed different linear elastic deformation models for the peripheral zone and the central gland of the prostate to register pre and intraoperative MR images. The proposed FEM-based model provides an inhomogeneous linearly elastic deformation model for the registration.

3.2 Static Linear Elastic Deformation Model

When at a static equilibrium, the total potential energy of deformable body is at a minimum. The total potential energy of an elastic body, Π, is sum of its strain energy and the potential energy of the external loads [172]. For an elastic continuum body with no initial strains or stresses, Π can be written as

$$\Pi = \frac{1}{2}\int_{\Omega} \sigma^t \epsilon \, d\Omega + \int_{\Omega} \mathbf{u}^t \mathbf{f} \, d\Omega \tag{3.1}$$

where $\mathbf{f}(x,y,z)$ is the vector of forces applied to the elastic body (acting on a unit volume of material within the element), $\mathbf{u} = (u,v,w)$ is the displacement field, and Ω represents the body of the elastic object. Moreover, ϵ is the strain vector which is defined for linear elastic

material as

$$\epsilon = \left(\frac{\partial u}{\partial x}, \frac{\partial v}{\partial y}, \frac{\partial w}{\partial z}, \frac{\partial u}{\partial x} + \frac{\partial v}{\partial y}, \frac{\partial v}{\partial y} + \frac{\partial w}{\partial z}, \frac{\partial u}{\partial x} + \frac{\partial w}{\partial z}\right)^t = \begin{bmatrix} \frac{\partial}{\partial x} & 0 & 0 \\ 0 & \frac{\partial}{\partial y} & 0 \\ 0 & 0 & \frac{\partial}{\partial z} \\ \frac{\partial}{\partial x} & \frac{\partial}{\partial y} & 0 \\ 0 & \frac{\partial}{\partial y} & \frac{\partial}{\partial z} \\ \frac{\partial}{\partial x} & 0 & \frac{\partial}{\partial z} \end{bmatrix} \begin{bmatrix} u \\ v \\ w \end{bmatrix} = \mathbf{Lu} \tag{3.2}$$

The stress vector, σ, is related to the strain vector by the material's constitutive relations. For linearly elastic materials with no initial stresses or strains, this relation is expressed as

$$\sigma = (\sigma_x, \sigma_y, \sigma_z, \tau_{xy}, \tau_{yz}, \tau_{xz})^t = \mathbf{D}\epsilon \tag{3.3}$$

where $\mathbf{D}$ is the *elasticity matrix of moduli* [172]. For isotropic material, i.e. material having identical values of a property in all directions, two independent elastic constants may be used to describe $\mathbf{D}$. Here, $\mathbf{D}$ is defined based on the Young's modulus of elasticity E, and Poisson's ratio ν as follows

$$\mathbf{D} = \frac{E}{(1+\nu)(1-2\nu)} \begin{bmatrix} 1-\nu & \nu & \nu & 0 & 0 & 0 \\ \nu & 1-\nu & \nu & 0 & 0 & 0 \\ \nu & \nu & 1-\nu & 0 & 0 & 0 \\ 0 & 0 & 0 & (1-2\nu)/2 & 0 & 0 \\ 0 & 0 & 0 & 0 & (1-2\nu)/2 & 0 \\ 0 & 0 & 0 & 0 & 0 & (1-2\nu)/2 \end{bmatrix} \tag{3.4}$$

Young's modulus E and Poisson's ratio ν are related to Lamé's first and second coefficients, λ and μ in Equations (2.29) and (2.30) as follows [172].

$$E = \frac{\mu(3\lambda + 2\mu)}{\lambda + \mu} \tag{3.5}$$

$$\nu = \frac{\lambda}{2(\lambda + \mu)} \tag{3.6}$$

Young's modulus E is the elastic modulus for tensile-compressive stress and represents the ratio of stress (force per area) to strain (fractional increase or decrease in length) in the direction of the load for a given material. Poisson's ratio ν, on the other hand, is the ratio of the strain perpendicular to the applied load (lateral strain) to the strain in the direction of the applied load (axial strain).

Based on the concept of a finite element discretization, a volume of elastic body is approximated as an assemblage of discrete finite elements interconnected at nodal points on the element boundaries. Hence, displacements of any point (x, y, z) within the elastic body $\mathbf{u}^{el}$ can be written as a function of the displacements at the element's nodal points $\mathbf{u}_j^{el}$ weighted by the element's shape function λ_j^{el} as defined in [172]

$$\mathbf{u}^{el} = \sum_{j=1}^{4} \lambda_j^{el}(x, y, z)\mathbf{u}_j^{el}. \tag{3.7}$$

Tetrahedral elements with linear interpolation of the displacement field are used to discretize the continuous volumetric body. Therefore, the shape function of node j of the tetrahedral element el is defined as

$$\lambda_j^{el}(x, y, z) = \frac{1}{6V^{el}}(a_j^{el}x + b_j^{el}y + c_j^{el}z + d_j^{el}) \tag{3.8}$$

where V^{el} is the volume of the tetrahedron. The four coefficients a_j^{el}, b_j^{el}, c_j^{el} and d_j^{el} can be obtained based on the position of the four vertices of the tetrahedron $\mathbf{u}_j^{el}$, e.g., see [172]. Deformation of the image grid in the registration technique is induced by the deformation of the FE mesh. Hence, deformation of any point on image grid can be computed based on nodal point displacements of the element in which the point lies using Equations (3.7) and (3.8).

For the volume of any tetrahedral element *el* with 4 vertices, the function to be minimized at each element, can be written as [172]

$$\Pi(\mathbf{u}_1^{el},...,\mathbf{u}_4^{el}) = \frac{1}{2}\int_\Omega \Big(\sum_{i=1}^{4}\sum_{j=1}^{4} \mathbf{u}_i^{el^t}\mathbf{B}_i^{el^t}\mathbf{D}\mathbf{B}_j^{el}\mathbf{u}_j^{el}\Big)\, d\Omega + \int_\Omega \Big(\sum_{i=1}^{4} \mathbf{u}_i^{el^t}\lambda_i^{el^t}\mathbf{f}\Big)\, d\Omega \tag{3.9}$$

Here, $\mathbf{u}_i^{el}$ and $\mathbf{u}_j^{el}$ are the nodal points displacement, $\mathbf{D}$ is the elasticity matrix, and

$$\mathbf{B}_i^{el} = \mathbf{L}_i\lambda_i^{el} \tag{3.10}$$

where $\mathbf{L}_i$ is the matrix $\mathbf{L}$ at node i. $\Pi(\mathbf{u}_1^{el},...,\mathbf{u}_4^{el})$ basically determines the contribution of element *el* to the energy function of the whole body.

The potential energy in (3.9) is a quadratic function of the nodal displacements vector. If $\Pi(.)$ has a local extremum at $\mathbf{u}^{el}$, its partial derivative with respect to the displacement field $\mathbf{u}^{el}$ must vanish, i.e.,

$$\frac{\partial\Pi(\mathbf{u}_1^{el},...,\mathbf{u}_4^{el})}{\partial\mathbf{u}_i^{el}} = 0 \;;\; i = 1,...,4 \tag{3.11}$$

$$\int_{\Omega} \sum_{j=1}^{4} \mathbf{B}_i^{el^t} \mathbf{D} \mathbf{B}_j^{el} \mathbf{u}_j^{el} \, d\Omega + \int_{\Omega} \lambda_i^{el^t} \mathbf{f} \, d\Omega = 0 \;\; ; \; i = 1, ..., 4 \tag{3.12}$$

This yields a set of linear equations of the form

$$\mathbf{K}^{el} \mathbf{u}^{el} = -\mathbf{f}^{el} \tag{3.13}$$

for each tetrahedral element, where $\mathbf{K}_{i,j}^{el} = \int_{\Omega} \mathbf{B}_i^{el^t} \mathbf{D} \mathbf{B}_j^{el} \, d\Omega$ is a 3×3 matrix and every i, j refers to pairs of nodes of the element el, and $\mathbf{f}_i^{el} = \int_{\Omega} \lambda_i^{el^t} \mathbf{f} \, d\Omega$ is the vector of forces concentrated at the node i of the element el.

The 12×12 matrices $\mathbf{K}^{el}$ and the 12×1 vector $\mathbf{f}^{el}$ are computed for each element and then are assembled in a global system as

$$\mathbf{K}\mathbf{u} = -\mathbf{f} \tag{3.14}$$

where $\mathbf{K}$ is called the global stiffness matrix associated with the volumetric mesh and is numerically integrated over the volume of the elastic body. The solution to this linear system of equations will provide the displacement field corresponding to the global minimum of the potential energy in Equation (3.1).

3.3 Dynamic Finite Element Deformation Model

The steady-state shape of a deformable body under external forces is determined by the solution to the static equilibrium Equation (3.14) which minimizes the energy function as a static problem. Another approach for computing the minima of a functional such as (3.1) is to construct a dynamical system which is governed by the functional. This allows

the system to gradually evolve to its equilibrium. Most anatomical structures in the human body are deformable and continuously undergo nonrigid motion due to interactions with the surrounding environment *in vivo*. Hence, dynamic models are highly valuable in medical image analysis applications. They have intuitively meaningful dynamical behaviour and can be used to estimate the deformation of soft tissue over time.

In image registration applications, one might also be interested in the transient motion and deformation behaviour of the object. To this end, the inertial body forces and energy dissipation through velocity dependent damping forces are added to the static equilibrium Equation (3.14) resulting in the following set of second-order differential equations for the nodal points displacement of the FE mesh [26]:

$$\mathbf{M}\ddot{\mathbf{u}} + \mathbf{C}\dot{\mathbf{u}} + \mathbf{K}\mathbf{u} = -\mathbf{f} \tag{3.15}$$

Here $\mathbf{M}$ is the mass matrix of the elements concentrated at nodes, and $\mathbf{C} = \alpha\mathbf{M} + \beta\mathbf{K}$ is the Rayleigh damping matrix for constant values of α and β. In nonlinear FE analysis, adding inertia and damping forces helps find the solution to the static equilibrium in a numerically effective way [26]. The volume of a tetrahedron with four vertexes can be computed based on the position of its nodal points as

$$V^{el} = \frac{1}{6}\det\begin{bmatrix} 1 & x_1 & y_1 & z_1 \\ 1 & x_2 & y_2 & z_2 \\ 1 & x_3 & y_3 & z_3 \\ 1 & x_4 & y_4 & z_4 \end{bmatrix} \tag{3.16}$$

Therefore, its mass is equal to $M^{el} = \rho V^{el}$ where ρ is the mass density of the object. To

construct the matrix $\mathbf{M}$ in (3.15), one-fourth of the mass of each element is concentrated at each nodal point of the element.

3.4 Modal Reduction

The differential Equations (3.15) can be solved over time using existing implicit or explicit numerical integration routines some of which are explained in [26]. To reduce computations very fast modes of this dynamical system might be isolated and discarded without affecting the response at a particular time scale relevant to the application of interest. For this purpose, Bathe [26] transforms the dynamics equations using a new variable $\mathbf{u} \triangleq \phi\mathbf{x}$, where columns of ϕ are eigenvectors of $\mathbf{M}^{-1}\mathbf{K}$. With this change of variables, Equation (3.15) can be written as

$$\tilde{\mathbf{M}}\ddot{\mathbf{x}} + \tilde{\mathbf{C}}\dot{\mathbf{x}} + \tilde{\mathbf{K}}\mathbf{x} = -\tilde{\mathbf{f}} \tag{3.17}$$

where $\tilde{\mathbf{M}} = \phi^t\mathbf{M}\phi$, $\tilde{\mathbf{C}} = \phi^t\mathbf{C}\phi$ and $\tilde{\mathbf{K}} = \phi^t\mathbf{K}\phi$ are diagonal matrices, and $\tilde{\mathbf{f}} = \phi^t\mathbf{f}$. Now, the dynamic finite element equations are decoupled in (3.17) and each equation describes a vibrational mode of the deformable body.

In the proposed registration method, the 3D FE mesh is not constrained; so, it would be able to move and deform at the same time. This would allow for simultaneous rigid and deformable transformation of the body. As a result, the dynamics of the 3D body in Equation (3.17) include six coupled equations accounting for rigid body motion which determine the position and orientation of the object. The remainder modes are all decoupled and can be solved independently. Modes that are very fast compared to the time step used for registration and the rate of changes in external forces can be simply eliminated from

the system dynamics. The modal reduction basically projects a full model behaviour onto a subspace of lower dimensionality, resulting in significant reduction of the computations of the registration algorithm. Working with a reduced number of states with slower dynamics improves the efficiency and robustness of the state estimation process as well, as will be explained later in the thesis.

Chapter 4

Volumetric Elastic Registration of Breast MR Images Using a Dynamic Deformation Model

In this chapter, the elastic energy of the developed model is employed as the regularizer in the optimization-based registration framework with an intensity-based similarity/distance measure. Rather than solving the optimization problem directly, corresponding Euler-Lagrange equations of motion are solved over time using a reduced dynamic FE model. The method is evaluated in the 3D-3D registration of a breast phantom MR images as well as real breast MR images.

4.1 Background and Motivation

Biomechanical elastic models are widely used in medical image analysis. In this section, a linear elastic model is employed to register volumetric images. The elastic energy of the model regularizes the deformation field in the optimization-based registration methods. As

explained in Section 2.7, elastic registration of two images can be formulated as solving a set of Euler-Lagrange equations given in (2.30). Using a biomechanical elastic model discretized in the spatial domain by FEM, Equation (2.30) can be written as

$$\mathbf{Ku} = -\mathbf{f}(\mathbf{u}) = -\frac{1}{\gamma}\nabla I(R, T[\mathbf{u}]) \tag{4.1}$$

where $\nabla I(R, T[\mathbf{u}])$ is the gradient of the similarity/distance measure between the reference R and the deformed template T images given nodal point displacement of the deformation model $\mathbf{u}$. The solution for Equation (4.1) would provide the deformation field for matching two images. It should be noted that the deformation for any voxel point of the image can be computed based on the deformation of the FE mesh using the elements' interpolation function in (3.7) and (3.8). In Equation (4.1), $\mathbf{f}(\mathbf{u})$ is a highly nonlinear function of $\mathbf{u}$. So, usually no closed-form solution can be found.

Rather than solving this nonlinear system of equations, De Craene *et al.* [173] directly optimized the cost function in Equation (2.2), from which these equilibrium equations are derived. They registered brain MR images using MI as the matching metric which was regularized by the linear elastic energy of the FE model. The optimal deformation field was found using a simultaneous perturbation stochastic approximation (SPSA) of the gradient. Ferrant *et al.* in [27] registered 3D brain MR images based on SSD between images using a linear elastic FE model. To avoid the computation of forces in (4.1), they approximated the deformed template image $T[\mathbf{u}]$ by its first order Taylor expansion assuming that the deformation field is small. Thanks to the simplicity of the SSD function, they derived a linear system of equations the solution of which would provide the deformation field corresponding to the global minimum of the matching cost function. In another work from this group, Ferrant *et al.* [70] used key surface information of the brain to find the deformation

rather than directly using image intensity information. They deformed the boundaries of an active surface model [174] to match them with the image boundaries using an iterative process. Having the displacements at the boundaries of the model, surface nodes of the volumetric FE model were determined to match those generated by the deformable surface model. The volumetric deformation field was then inferred from the solution for the biomechanical FE model of the object. Furthermore, Crouch *et al.* [160] calculated the boundary conditions for the solution of FE model using segmented surfaces of the prostate images. Solution methods and their implementation for equilibrium equations in FE static analysis are discussed in [26].

The stiffness matrix $\mathbf{K}$ in (4.1) is not full rank when the model is not constrained. For a 3D FE model with n nodal points, the rank of $\mathbf{K}$ is $3 * n - 6$. Therefore, even when applied forces are given, a unique displacement field can not be computed without applying some constraints on the model. Applied constraints can be obtained based on the boundary conditions, or fixing some of the nodes by giving them predetermined displacements [26]. Since the deformable tissues can undergo free form deformations and movements, fixing nodal points of the mesh is not desirable, unless we have a good understanding of the organ and its surrounding tissues.

An iterative method needs to be employed to solve Equation (4.1) which is derived from the registration problem. A few methods for the solution of nonlinear equilibrium equations are given in [26]. These methods which all are based on the derivative of the nonlinear function $\mathbf{f}(\mathbf{u})$ would not be suitable for the present problem. Image similarity/distance metric is often a highly nonlinear and non-smooth function of the displacement field. $\mathbf{f}(\mathbf{u})$ is already computed based on the first derivative of the similarity/distance measure, i.e., $\nabla I(R, T[\mathbf{u}])$. The second derivative of the similarity/distance measure would not be smooth

and continuous, and a solution for (4.1) may be difficult or impossible to obtain.

4.2 Registration Method

In this thesis, a dynamic deformation model is employed to solve nonlinear equilibrium equations resulted from the linear elastic FE model-based registration. The dynamic model smoothly drives the nonlinear equations to their equilibrium points over time. No specific geometrical model is used in the registration , rather a simple cubic mesh discretized by tetrahedral elements is employed. It is the image derived forces that deform the FE mesh to produce a deformation field for matching images.

4.2.1 Deformation Model

To solve the problem in this thesis, the inertia and velocity dependent forces are added to the static equilibrium equations as

$$\mathbf{M}\ddot{\mathbf{u}} + \mathbf{C}\dot{\mathbf{u}} + \mathbf{K}\mathbf{u} = -\mathbf{f}(\mathbf{u}) = -\frac{1}{\gamma}\nabla I(R, T[\mathbf{u}]) \tag{4.2}$$

The dynamic model not only provides an estimate of the tissue deformation over time, but also the dynamic inertia $\mathbf{M}\ddot{\mathbf{u}}$ and damping $\mathbf{C}\dot{\mathbf{u}}$ forces tend to smoothly drive the system to its equilibrium. It should be noted that the steady-state equilibrium of the dynamic system given in (4.2) is the solution to the static system of Equations (4.1). Equation (4.1) is solved iteratively and Equation (4.2) is solved over time. However, because of the smoothing effect rendered by the inertia and damping forces in (4.2), the convergence of the dynamic nonlinear system of equations is faster than its static solution in (4.1) [26]. As mentioned before in Section 3.4, discarding fast vibrational modes of the dynamic model also helps

the model to smoothly evolve towards its equilibrium. The reduced dynamic deformation model is solved numerically at each iteration to find the displacement of the FE mesh nodal points and the deformation field for the template image. Various implicit and explicit methods are discussed in [26] to solve the equilibrium equation in the dynamical FE analysis among which the Newmark integration method is employed in this thesis. Newmark method is an implicit numerical integration method for solving differential equations which is explained in Appendix A. In the Newmark method, other than time step Δt for integration, two parameters, i.e., δ and ξ, need to be selected. For appropriate values of δ and ξ, the Newmark method is stable regardless of the size of time step Δt for integration [26].

4.2.2 Gradient of Similarity/Distance Measures

Registration of MR images is considered in this chapter. Four different similarity/distance measures applicable to single and multi-modality images (see 4.1) are employed for the registration and their performances are evaluated. To obtain the force vector in Equation (4.2), derivative of the employed similarity/distance measure should be computed. An analytical approach is proposed in [128, 175] to compute the variational gradient of some statistical similarity/distance measures. By letting g denote a generic intensity comparison function, the gradient of the given similarity/distance measure can be written as

$$\nabla I(R, T[\mathbf{u}]) = g(T[\mathbf{u}], R)\, \nabla T[\mathbf{u}] \tag{4.3}$$

where $\nabla T[\mathbf{u}]$ is the gradient of the deformed template image for a given displacement field $\mathbf{u}$. The intensity comparison functions related to metrics given in Table 4.1 are summarized in Table 4.2 where $\Psi(.)$ is a bidimensional density kernel (strictly positive and differentiable) for smoothing and $\mu(\Omega)$ denotes the volume of Ω. Moreover, i_1 and i_2 are

Table 4.1: Similarity/distance measures.

Similarity/Distance Measure $I(T[\mathrm{u}], R)$
$\mathrm{SSD}(\mathrm{u}) = \frac{1}{2}\int_{\Omega}(T[\mathrm{u}]-R)^2\, d\Omega$
$\mathrm{CR}(\mathrm{u}) = 1 - \frac{\mathrm{Var}\left[E[X_{\mathrm{u}}^{T}\|X^{R}]\right]}{\mathrm{Var}\left[X_{\mathrm{u}}^{T}\right]}$
$\mathrm{NCC}(\mathrm{u}) = -\frac{\mathrm{Cov}\left[X_{\mathrm{u}}^{T}, X^{R}\right]^2}{\mathrm{Var}\left[X_{\mathrm{u}}^{T}\right]\mathrm{Var}\left[X^{R}\right]}$
$\mathrm{MI}(\mathrm{u}) = \int_{\Re^2} p_{\mathrm{u}}^{T,R}(i_2,i_1)\log(\frac{p_{\mathrm{u}}^{T,R}(i_2,i_1)}{p_{\mathrm{u}}^{T}(i_2)p^{R}(i_1)})\, di_1 di_2$

Table 4.2: Intensity comparison functions related to similarity/distance measures given in Table 4.1.

I	$g(T[\mathrm{u}], R)$
SSD	$i_1 - i_2$
CR	$\frac{2\Psi*\left(i_2 - E[X_{\mathrm{u}}^{T}\|X^{R}=i_1] + (\mathrm{CR}_{\mathrm{u}}^{T,R}-1)(i_2-E[X_{\mathrm{u}}^{T}])\right)}{\mathrm{Var}\left[X_{\mathrm{u}}^{T}\right]\mu(\Omega)}$
NCC	$-\frac{2}{\mu(\Omega)}\left[\frac{\mathrm{Cov}\left[X_{\mathrm{u}}^{T}, X^{R}\right]}{\mathrm{Var}\left[X_{\mathrm{u}}^{T}\right]}(\frac{i_1 - E[X^{R}]}{\mathrm{Var}\left[X^{R}\right]}) + \mathrm{NCC}_{\mathrm{u}}^{T,R}(\frac{i_2 - E[X_{\mathrm{u}}^{T}]}{\mathrm{Var}\left[X_{\mathrm{u}}^{T}\right]})\right]$
MI	$-\frac{1}{\mu(\Omega)}\left[\Psi * \left(\frac{1}{p_{\mathrm{u}}^{T,R}}\frac{\partial p_{\mathrm{u}}^{T,R}}{\partial i_2} - \frac{1}{p_{\mathrm{u}}^{T}}\frac{\partial p_{\mathrm{u}}^{T}}{\partial i_2}\right)\right](i_2, i_1)$

the intensity of the reference R and the deformed template $T[\mathbf{u}]$ images respectively at any point that the derivative of the similarity/distance measure is computed at.

4.2.3 Registration Algorithm

The flowchart of the proposed registration algorithm is given in Figure 4.1. In the following, the registration steps at each iteration are explained in details.

1. *Image Interpolation*: Trilinear interpolation method [60] is used to compute the reference R and the deformed template $T[\mathbf{u}]$ images. To reduce computations in the iterative routine, R and $T[\mathbf{u}]$ might be obtained by downsampling of the original acquired images. A multilevel scheme (low to high-resolution) might also be used in the iterative

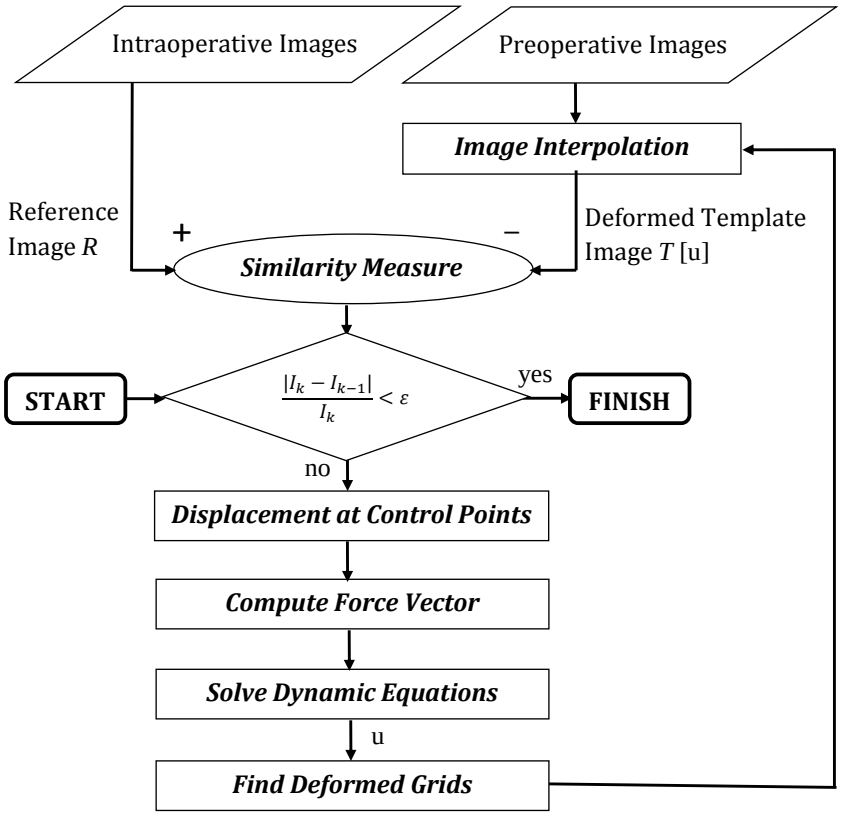

Figure 4.1: Block diagram of the iterative registration algorithm based on the concept of dynamic state estimation.

to smoothen and speed up the convergence. At the beginning of the registration algorithm low resolution R and $T[\mathbf{u}]$ images are employed which provide smoother image comparison function. While the algorithm progresses, the higher resolution images are computed for R and $T[\mathbf{u}]$ from the original acquired images to utilize more image details in the registration. R (computed once for each level) and $T[\mathbf{u}]$ images at each iteration are used to compute the joint histogram when NCC, CR, or MI is employed as the similarity/distance measure between the images.

2. *Displacement at Control Points*: Other than the image grid, there is another grid whose

intersections are called "control points", or $\mathbf{x}_c$ [8]. The force vector which is applied on the nodal points of the FE mesh are computed based on the gradient of the similarity/distance measure at the control points. Directional gradient of the matching metric at these points provides a displacement field towards matching two images at each iteration, i.e.

$$\mathbf{dx}_c = \frac{1}{\gamma_1} \nabla I_{\mathbf{x}_c}(R, T[\mathbf{u}]) \tag{4.4}$$

where γ_1 is constant gain.

3. *Compute Force Vector*: Each control point falls inside one tetrahedral element. Applied forces are proportional to the amount of displacement at nodal points. Therefore, having the displacement at control points, the displacement at nodal points of the FE mesh $\mathbf{dx}_p$ are computed based on the inverse of the elements' interpolation (shape) functions using following equitation

$$\Lambda \, \mathbf{dx}_p = \mathbf{dx}_c \tag{4.5}$$

Equation (4.5) is an overdetermined linear system of equations, and Λ is a tall matrix computed based on the current position of FE nodal points and the interpolation functions of the elements. The nodal point forces are approximated as the least-squares solution of the overdetermined equations, i.e.

$$\mathbf{f} = \frac{1}{\gamma_2} \mathbf{dx}_p = \frac{1}{\gamma_2} \Lambda^+ \, \mathbf{dx}_c = \frac{1}{\gamma_1 \gamma_2} \Lambda^+ \, \nabla I_{\mathbf{x}_c}(R, T[\mathbf{u}]) = \frac{1}{\gamma} \Lambda^+ \, \nabla I_{\mathbf{x}_c}(R, T[\mathbf{u}]). \tag{4.6}$$

where $\Lambda^+ = \lim_{\delta \to 0} (\Lambda^t \Lambda + \delta I)^{-1} \Lambda^t$ is the Moore-Penrose pseudoinverse of Λ [176]. This limit exists even when Λ is singular or ill-conditioned. $\gamma = \gamma_1 \gamma_2$ is the factor which

weight the regularizer to provide a balance between the similarity/distance measure and the elastic energy of the linear FE model.

4. *Solve Dynamic Equations*: The force vector computed at nodal points of the FE mesh are applied to the dynamic model to find the displacement field at each sample time. As explained in Section 3.4, the model in (4.2) is not directly solved, but a reduced dynamic model is used to compute the deformation. After the change of variables in (3.17), assume that $\mathbf{x} = [\mathbf{x}_1, \mathbf{x}_2]^t$ where $\mathbf{x}_1$ denotes the first m slow modes of the decoupled equations and $\mathbf{x}_2$ represents the rest of the modes. Therefore, to find $\mathbf{x}$ at each iteration, the following equations are solved:

$$\tilde{\mathbf{M}}_1\ddot{\mathbf{x}}_1 + \tilde{\mathbf{C}}_1\dot{\mathbf{x}}_1 + \tilde{\mathbf{K}}_1\mathbf{x}_1 = -\tilde{\mathbf{f}}_1 \tag{4.7}$$

$$\tilde{\mathbf{K}}_2\mathbf{x}_2 = -\tilde{\mathbf{f}}_2 \tag{4.8}$$

$\tilde{\mathbf{M}}_1$, $\tilde{\mathbf{C}}_1$, $\tilde{\mathbf{K}}_1$ and $\tilde{\mathbf{K}}_2$ are parts of the original $\tilde{\mathbf{M}}$, $\tilde{\mathbf{C}}$, and $\tilde{\mathbf{K}}$ matrices, and $\tilde{\mathbf{f}} = [\tilde{\mathbf{f}}_1, \tilde{\mathbf{f}}_2]^t$. Based on numerical experiments, 5-10% of the slower modes of the original model are enough to capture the dynamic of the deformation. The rest of the modes are fast enough with respect to the first m modes so that only steady-state solution for these fast modes is computed. Equation (4.7) is solved using the Newmark numerical intergration method [26]. $\tilde{\mathbf{K}}_2$ is a diagonal matrix; hence, $\mathbf{x}_2 = -\tilde{\mathbf{K}}_2^{-1}\tilde{\mathbf{f}}_2$, where the $\tilde{\mathbf{K}}_2^{-1}$ is a diagonal matrix whose elements are the inverse of the $\tilde{\mathbf{K}}_2$ diagonal elements. Having $\mathbf{x}$ at each sample time, nodal points displacements can be computed using $\mathbf{u} \triangleq \phi\mathbf{x}$.

5. *Find Deformed Grids*: Deformation of both image grid and the grid for control points are computed based on the deformation of the FE mesh using elements' interpolation (shape) functions. The deformed image grid is used to interpolate the deformed template

image $T[\mathbf{u}]$ in the next iteration. Derivative of the similarity/distance metric is computed at new positions of the control points to obtain the force vector in the next iteration.

The iterative algorithm terminates when the relative change in the similarity/distance measure between the reference R and the deformed template image $T[\mathbf{u}]$ (i.e., $I(R, T[\mathbf{u}])$) is less than a given small number ε, i.e., $|I_k - I_{k-1}|/I_k < \varepsilon$, or the total iterations exceeds a maximum number. At the end of the iterations, the deformation model reaches its equilibrium point with a nodal point displacements vector of $\mathbf{u}$. Based on Equation (4.1) and Equation (4.6), the steady-state equilibrium equations become

$$\mathbf{K}\mathbf{u} = -\frac{1}{\gamma}\Lambda^{+}\ \nabla I_{\mathbf{x}_c}(R, T[\mathbf{u}]) \tag{4.9}$$

At the end of the iterations, one can compute the deformed template image $T[\mathbf{u}]$ with desired resolution in the similar way explained in steps 5 and 1 of the iterative algorithm. Since the second-order differential equations in (4.7) are decoupled (except for the first six equations), the characteristic equation for each vibrational mode can be written as

$$s^2 + 2\zeta\omega_n s + \omega_n^2 = 0 \tag{4.10}$$

where ζ and ω_n are the damping ratio and natural frequency respectively. The parameters α and β in $\mathbf{C} = \alpha\mathbf{M} + \beta\mathbf{K}$ are chosen for a critically damped response, i.e., $\zeta \approx 1$; this would ensure a fast response without oscillation, the system converges to its steady-state response as fast as possible without having oscillations. The sample time in the Newmark method which is also the sample time for the iterations is obtained as

$$T_s \cong \frac{1}{30\sqrt{2}}\left(\frac{2\pi}{\omega_m}\right) \tag{4.11}$$

where ω_m is the natural frequency for the fastest vibrational mode in the reduced dynamic model of size m (4.7). In other words, sampling frequency is chosen to be 30 times the bandwidth of the system defined by the fastest vibrational mode.

4.3 Experiments and Results

4.3.1 Registration of a Breast Phantom MR Images

In this section, high-resolution volumetric MR images of a breast phantom is registered to its compressed high and low resolution images. A triple modality biopsy training breast phantom (CIRS model 051 [177]) is used for obtaining the experimental data. This compressible phantom can be imaged under three different modalities, e.g., X-ray, US, and MRI, and is designed specially for needle biopsy training. A volume of high-resolution (512×512×136) MR images with voxel size of 0.43×0.43×0.8 mm was obtained from the uncompressed phantom using a GE Discovery MR750 3.0T machine and a head receiver coil. An apparatus is designed and fabricated in order to provide a stand for the phantom during imaging. As is shown in Figure 4.2a, this structure is made of plexiglass and is MR compatible. It has two stabilizing plates between which the phantom can be compressed. Four pairs of screws and nuts which are connected to the plates are used to adjust the distance between them to compress the phantom. Moreover, four capsules of vitamin E are placed on the framework as landmarks to match the coordinates of the deformed and undeformed image data after acquiring images. As can be seen from Figure 4.2b, the phantom is compressed by 40.5 mm in x direction. Two sets of high-resolution (512×512×116) and low-resolution (64×64×32) MR volumes are obtained from the compressed phantom for which the voxel sizes are 0.43×0.43×0.8 mm and 3.44×3.44×6.4 mm respectively. Other

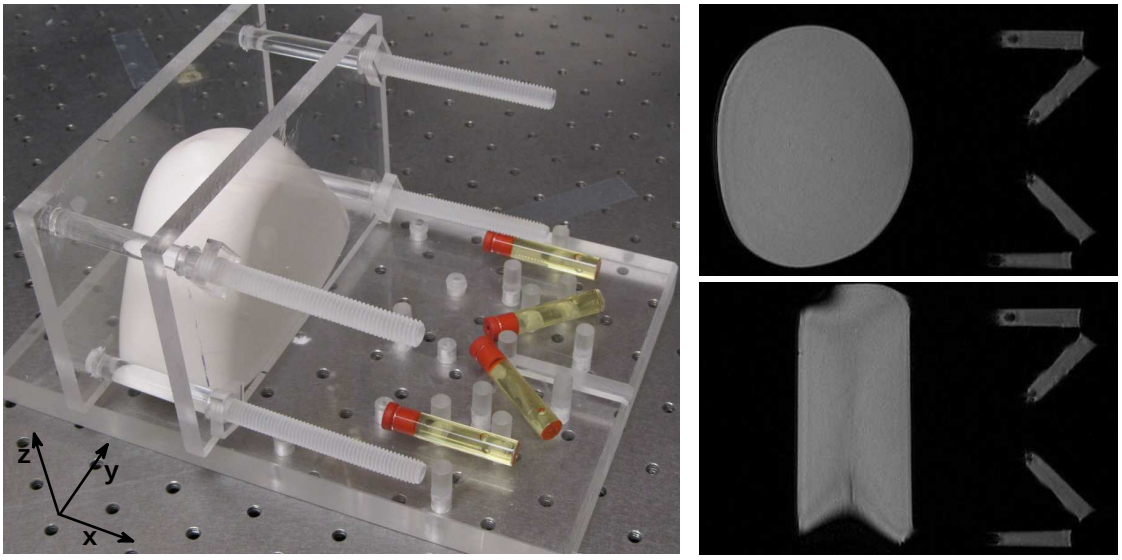

(a) (b)

Figure 4.2: (a) The apparatus for compressing the breast phantom and (b) Coronal views of the uncompressed (top) and compressed (bottom) phantom images.

imaging parameters for high-resolution images are as follows: field-of-view: 220×220 mm, number of signal averages: 1, repetition time: 9.16 ms, echo time: 2.1 ms, flip angle: 12°. These parameters for low-resolution images are: field-of-view: 220×220 mm, number of signal averages: 1, repetition time: 5.38 ms, echo time: 2.1 ms, flip angle: 12°.

A coronal (x-y) view of the uncompressed and compressed phantom images is shown in Figure 4.2b in which the capsules of vitamin E can be seen.

A cubic mesh of tetrahedral elements which encompasses the entire volume of the compressed breast image data is created using the COMSOL Multiphysics and Simulation Software [178]. The mesh has 15112 elements with 3067 nodal points. Using this mesh, an isotropic linear elastic model of deformation with the Young's elasticity modulus $E = 3$ kPa, the Poisson's ratio $\nu = 0.49$ and a mass density of $\rho = 0.95$ g/cm^3 is created. These values are close to what are reported in literature for real breast tissue, e.g., see [179, 180]. Since the geometry of the breast is not determined in the registration, the elastic properties of the

image background (air) are considered to be similar to those of the breast tissue. However, nodal point forces are computed using an intensity-based image similarity/distance measure at any point rather than using surfaces or boundaries. Therefore, the model is essentially regularizes the registration problem, providing a smooth transformation between images. The model parameters can also be tuned to obtain a desirable outcome. Although the model is not accurate, it is the vector of forces derived from the image similarity/distance metric which deforms the model in a way that brings two set of images together as close as possible. The most effective and important parameter to be tuned is γ which determines the amplitude of the applied force vector. In other words, γ is important in balancing the effect of the similarity/distance measure and the linear elastic energy of the deformable model which regularizes the registration problem. It is clear from Figure 4.2b that, to register uncompressed images to compressed images, the FE mesh based on which the deformation model is defined has to translate and deform in order to cope with the large deformation in the breast phantom.

A grid of 20×30×10 inside the domain of reference image R is used as control points. Also, the resolution of image grid in the iterative process is considered twice the resolution of the control points, i.e. 40×60×20. A higher resolution image grid would provide more information in information theoretic-based similarity/distance measures, which in principle should result in a better outcome. The size of the image grid was determined through numerical experimentation to achieve a balance between registration quality and computational load.

Using the proposed algorithm, uncompressed phantom images are registered to compressed phantom images based on four different similarity/distance measures. Registration results using SSD as a distance measure between images are shown in Figure 4.3 where

three different views of the template (a), reference (b), deformed template (c) and the difference images (d) are given. In this figure, the high-resolution MR image data of the compressed phantom is used as the reference image and the difference image is the intensity difference between the reference and the deformed template images. As is shown in this figure, template images (a) are registered to the reference images (b) and the resulting deformed template images (c) are very similar to the reference images.

The iterative evolution of four similarity/distance measures based on which the registration is performed are given in Figure 4.4. The iterative algorithm in SSD, CR and NCC-based registration is terminated before reaching the maximum number of iterations (i.e., 120). All values in this figure are computed based on the formula given in Table 4.1 except for SSD which is divided by the number of voxel points to give a sensible number. Number of bins for computing the joint histogram of images and compute similarity/distance measures is considered as $N = 64$. Furthermore, to compute displacement at control points $d\mathbf{x}_c$, the joint histogram function is smoothed using a 2D Gaussian filter.

In the computation of the gradient of the template image $\nabla T[\mathbf{u}]$ in Equation (4.3), a 3D Gaussian filter with a variable standard deviation σ is employed to reduce noise and control the amount of image details used in the registration. It starts with a 23×23×23 kernel and $\sigma = 5$ that would filter out high spatial frequency content of the image; so, the registration relies on low-frequency content in the beginning. As the number of iterations grows, σ is gradually reduced to utilize more of the image details in the registration. The size of the Gaussian kernel is 3×3×3 with $\sigma = 0.5$ towards the end of the iterative registration algorithm. The FE mesh used for the registration before and after deformation is shown in Figure 4.5. In image registration, a backward mapping function is used to transform the template image T and match it with the reference image R. Hence, as shown in Figure 4.5,

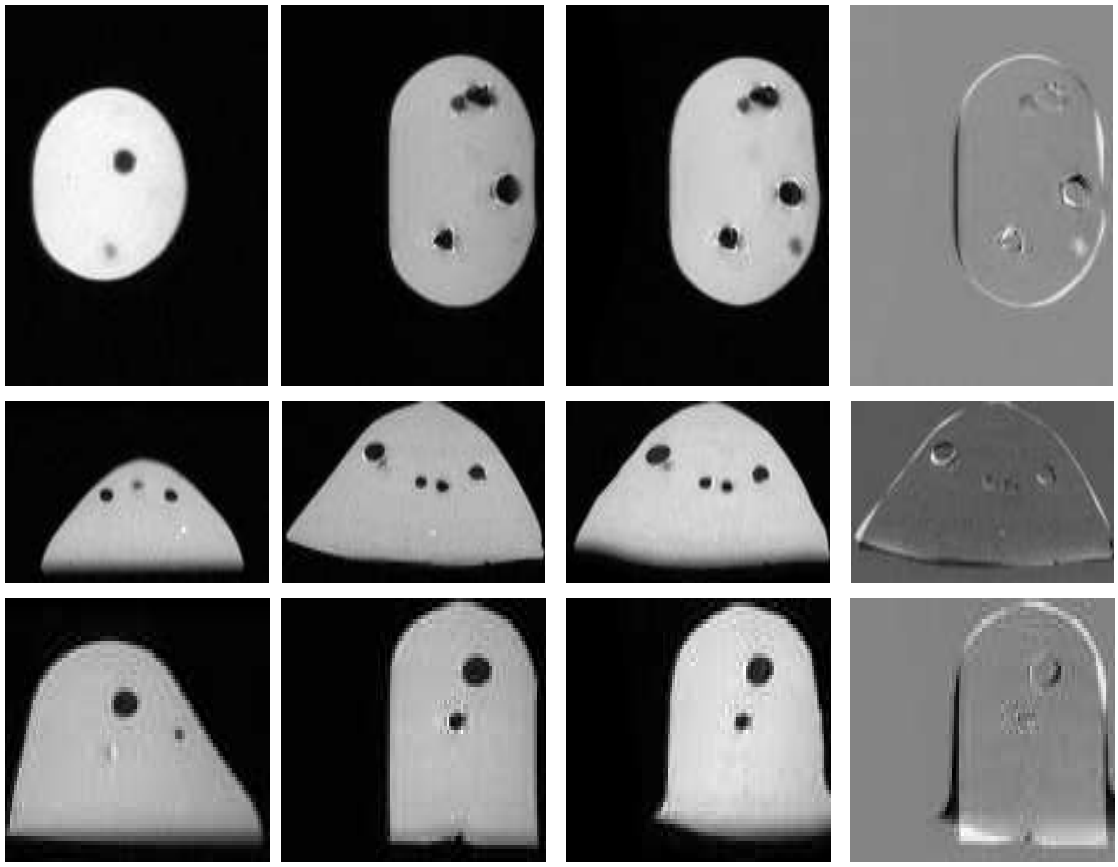

(a) (b) (c) (d)

Figure 4.3: Coronal (top row), axial (middle row) and sagittal (bottom row) views of the template (a), reference (high-resolution) (b), registered deformed template (c) and the difference images (d) in 3D-3D SSD-based registration of the breast phantom image data.

the estimated deformation of the FE mesh is different from the actual physical deformation of the breast phantom. While the breast phantom is compressed, the FE mesh is decompressed which provides a reverse deformation for backward mapping from the reference image R coordinateds to the template image T coordinates.

The size of the reduced dynamic model is $m = 500$ where only 5.4% of modes of the full deformation model is considered in the dynamic model. The effect of the number of bins N in the calculation of the joint probability density function on the quality of registration

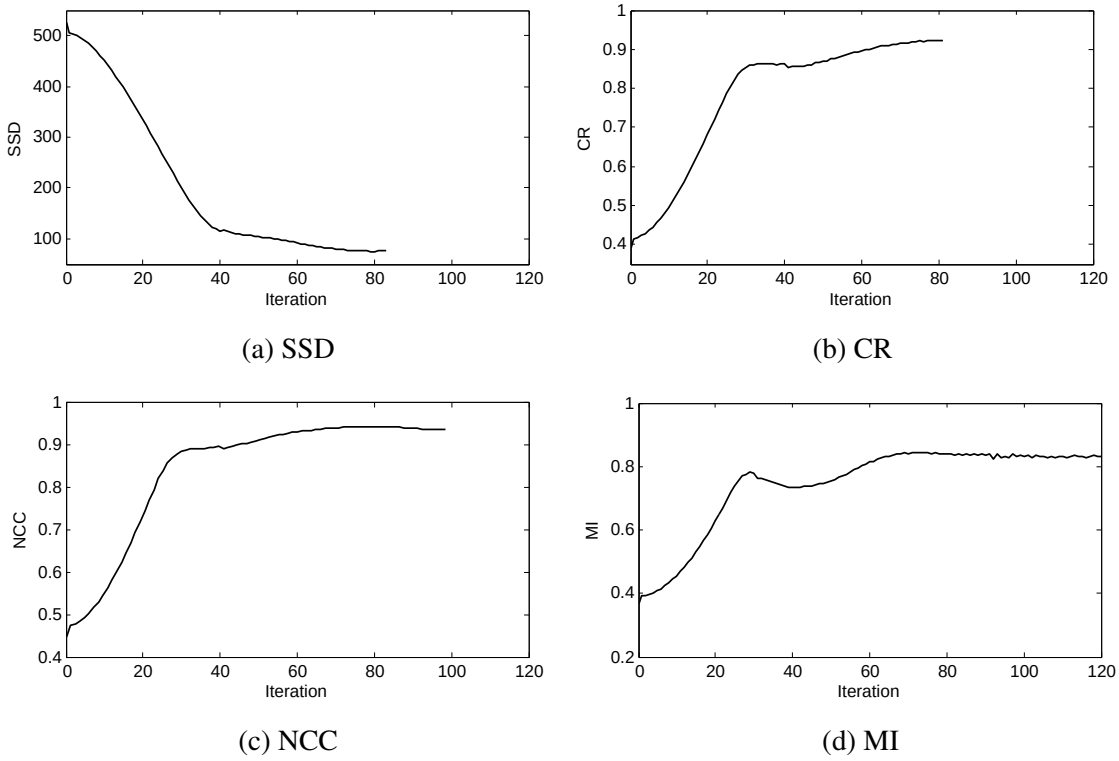

(a) SSD (b) CR

(c) NCC (d) MI

Figure 4.4: The evolution of the similarity/distance measures in the iterative registration method using high-resolution compressed phantom images as the reference image. Number of bins $N = 64$.

is also examined. This is specially important in registration methods using MI, NCC, and CR as the similarity/distance metric. Different values are tested for N, e.g., 256, 128, 64, 32 and 16, among which the registration based on 32 and 64 bins produce equally better results than others.

A quantitative comparison of registration performance based on different similarity/distance metrics is given in Table 4.3. Eight pairs of fiducial points are identified in both uncompressed and compressed phantom image data using 3DSlicer [181]. These points are mostly chosen to be the center of cystic masses in the images. In Table 4.3, the average (mean), standard deviation (std) and median of distances between fiducial points before

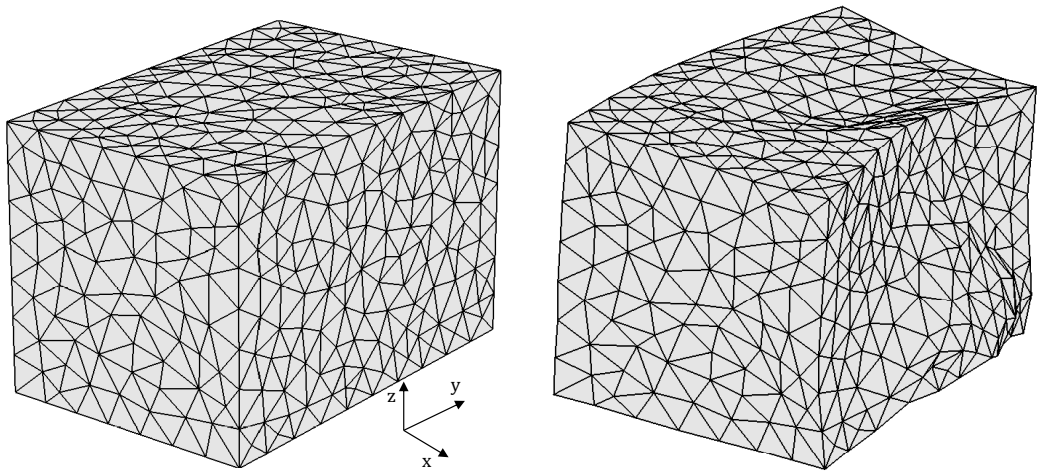

(a) Undeformed mesh (b) Deformed mesh

Figure 4.5: Undeformed and deformed FE mesh for phantom image registration.

and after the registration are given. These distances which are also called target registration error (TRE) for registered images are analyzed in different axes as well as in terms of root mean square (RMS) distances. It can be concluded from this table that, the RMS distance between fiducial points is decreased from about 15.3 mm before registration to about 2.4 mm after registration.

As was expected, most of the deformation correction is done in the x direction in which the deformation was larger. Registration results show that CR-based registration outperforms other metrics. SSD-based registration provides acceptable results considering that its computational load is less than other methods. SSD-based registration does not compute the joint histogram between images. Furthermore, the computation of the deformation of image grid and interpolation of the deformed image at each iteration are not required. MI has a poor performance in the registration. Phantom image data has less information

Table 4.3: 3D-3D registration results in terms of TRE (in mm) using different similarity/distance measures. Reference images are *high-resolution* compressed phantom images. Coordinate frames are given in Figure 4.2a.

Registration using	SSD	CR	NCC	MI	Before
Mean±std in x	1.70±1.32	1.60±1.05	1.65±1.25	2.11±1.92	14.70±1.72
Mean±std in y	0.64±0.46	0.58±0.51	0.73±0.53	0.77±0.53	2.85±1.91
Mean±std in z	1.15±1.17	0.90±0.90	0.99±0.84	1.37±1.13	2.08±1.43
Mean±std	2.41±1.41	2.11±1.15	2.24±1.29	2.85±1.97	15.31±1.37
Median	3.01	2.60	2.44	2.14	15.82

content than actual tissue images which provides a joint histogram with less dispersion. MI-based registration is sensitive to the information content of the overlapping area between images. Hence, low information content and low spatial intensity correlation between images are reasons for poor performance of the MI-based registration.

In another experiment, high-resolution images of the uncompressed phantom (template) are registered to low-resolution images of the compressed phantom (reference). Low-resolution 3D images can be obtained faster than high-resolution images. Therefore, registering high-resolution preoperative images to the low-resolution intraoperative (nearly real-time) images would be of great interest for real-time image-based interventions. The results of registration based on CR are given in Figure 4.6. In Figure 4.6d the deformed template images are compared to the high-resolution compressed phantom images, i.e, the difference image is the intensity difference between the high-resolution compressed breast images and the deformed template images. All the registration parameters are the same as the previous experiment except for the gain γ which is tuned to improve the performance. The comparative results for this experiment in terms of TRE are also given in Table 4.4. It can be concluded that, the average TRE is decreased from about 15.3 mm before registration to about 3.2 mm after registration. It is also evident that CR and NCC-based registrations outperformed those based on SSD and MI. Comparing the results in Table 4.3

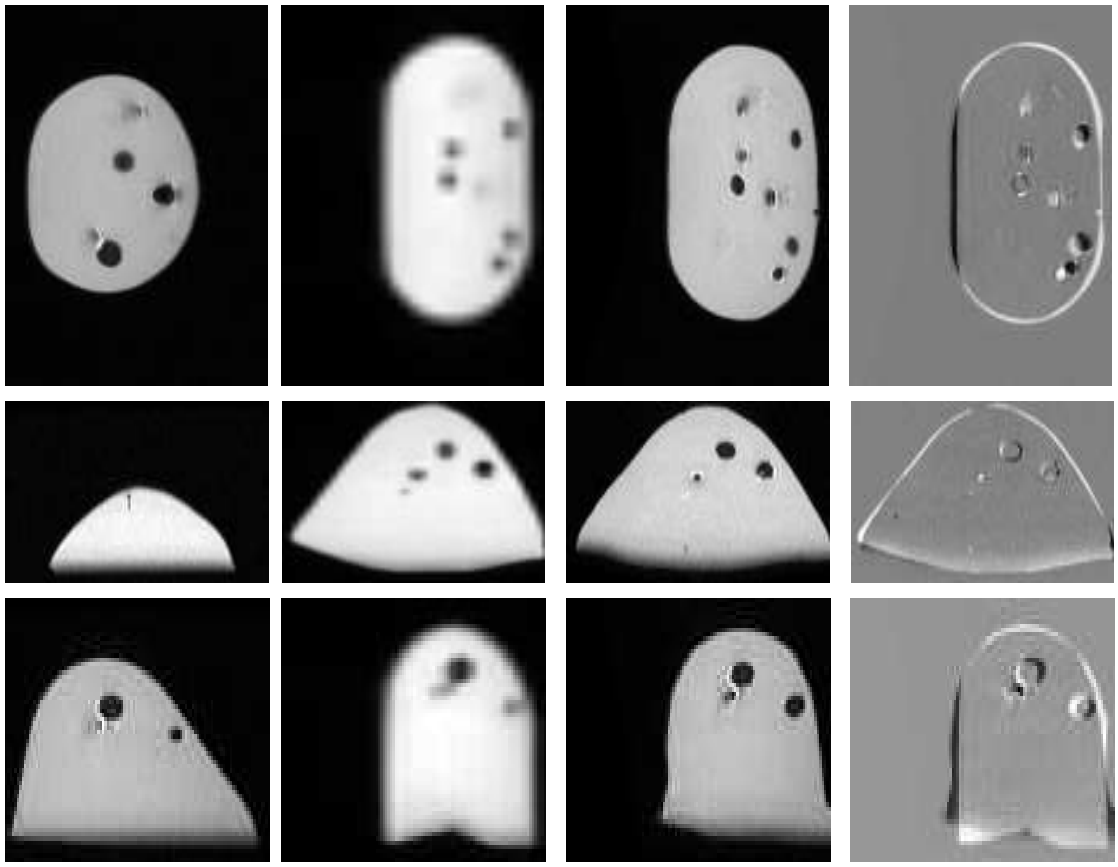

(a) (b) (c) (d)

Figure 4.6: Coronal (top row), axial (middle row) and sagittal (bottom row) views of the template (a), reference (low-resolution) (b), registered deformed template (c) and the difference images (d) in 3D-3D CR-based registration of the breast phantom image data.

and Table 4.4, the average TRE is increased in the low-resolution case by about 0.8 mm in different cases.

4.3.2 Registration of MR images of Real Breast Tissue

In this section, 3D MR images of normal and compressed actual breasts are registered together using the proposed method. MR images of the breast tissue of a middle-aged healthy

Table 4.4: 3D-3D registration results in terms of TRE (in mm) using different similarity/distance measures. Reference images are *low-resolution* compressed phantom images. Coordinate frames are given in Figure 4.2a.

Registration using	SSD	CR	NCC	MI	Before
Mean±std in x	2.79±1.70	2.03±1.80	2.25±1.52	2.99±1.80	14.70±1.72
Mean±std in y	0.77±0.56	0.66±0.34	0.64±0.28	0.73±0.57	2.85±1.91
Mean±std in z	1.03±0.76	1.08±0.66	1.25±0.88	1.03±0.88	2.08±1.43
Mean±std	3.37±1.23	2.94±1.11	2.86±1.37	3.58±1.34	15.31±1.37
Median	2.99	2.57	2.73	2.87	15.82

volunteer have been acquired under uncompressed and compressed conditions. The images have been captured using a GE 1.5 T Signa HDx (GE Healthcare, Milwaukee, WI) MRI scanner and a Sentinelle Medical 8 channel phased array (PA) coil. The coils were placed 4 per breast to give lateral compression with 2 coils per side. Compression variation was also done using these coils. The MRI volumes have been taken in prone position and are 512×512×240 with voxel size of 0.7×0.7×1.1 mm. Other imaging parameters are as follows: field-of-view: 360×360 mm, number of signal averages: 0.7097, repetition time: 5.8 ms, echo time: 2.8 ms, flip angle: 10°, receiver bandwidth: 63.9 kHz and 162.8 Hz/pixel. Figure 4.7 shows axial (x-y) views of the compressed and uncompressed breast. The compression is in the x direction, 14.6 mm for the right and 24.6 mm for the left breast images. Registration algorithm is applied to both right and left breast images separately and the experimental results on both image data are presented.

A cubic finite element mesh of tetrahedral elements which encompasses the entire volume of the compressed breast images is created using COMSOL software [178]. The mesh has 21151 elements with 4206 nodal points. The same FE mesh has been used for the registration of both right and left breast images. Like previous experiment, an isotropic linear elastic model of deformation with the Young's elasticity modulus $E = 3$ kPa, the Poisson's ratio $\nu = 0.49$ and a mass density of $\rho = 0.95$ g/cm^3 is created. With this mesh,

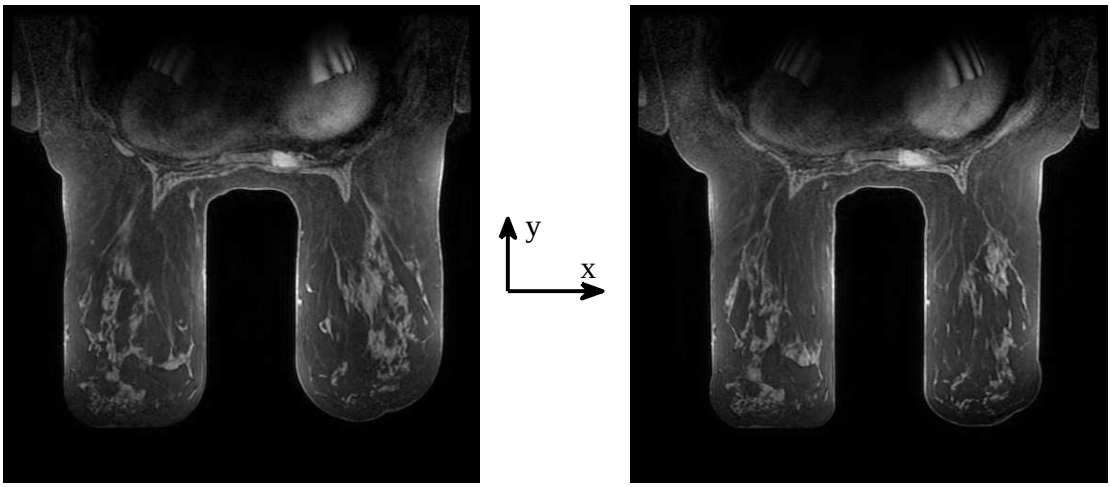

Figure 4.7: Axial(x-y) views of the uncompressed (left) and compressed (right) breast images taken from a healthy middle-aged woman in prone position.

the length of the vector of nodal displacements **u** in (4.2) is 3×4206=12618, accounting for displacements in x, y and z directions. The undeformed and deformed FE mesh is shown in Figure4.8.

The size of the reduced dynamic model is m = 500 where only 3.96% of modes of the full deformation model is considered in the dynamic model. Like previous experiment, an smoothing Gaussian kernel with variable standard deviation σ is employed to reduce noise and control the amount of details used in the computation of the gradient of the template image $\nabla T[\mathbf{u}]$. A regular grid of 30×40×40 is considered as control points, a grid twice this size, i.e., 60×80×80, is used as the image grid in the iterative registration algorithm.

An axial view of the left compressed breast image (reference) is shown in Figure 4.9a where the grid of control points overlaid. Figure 4.9b shows the uncompressed breast image (template) with the deformed grid of control points. The deformed image which is computed based on interpolating the deformed image grid from template image is shown

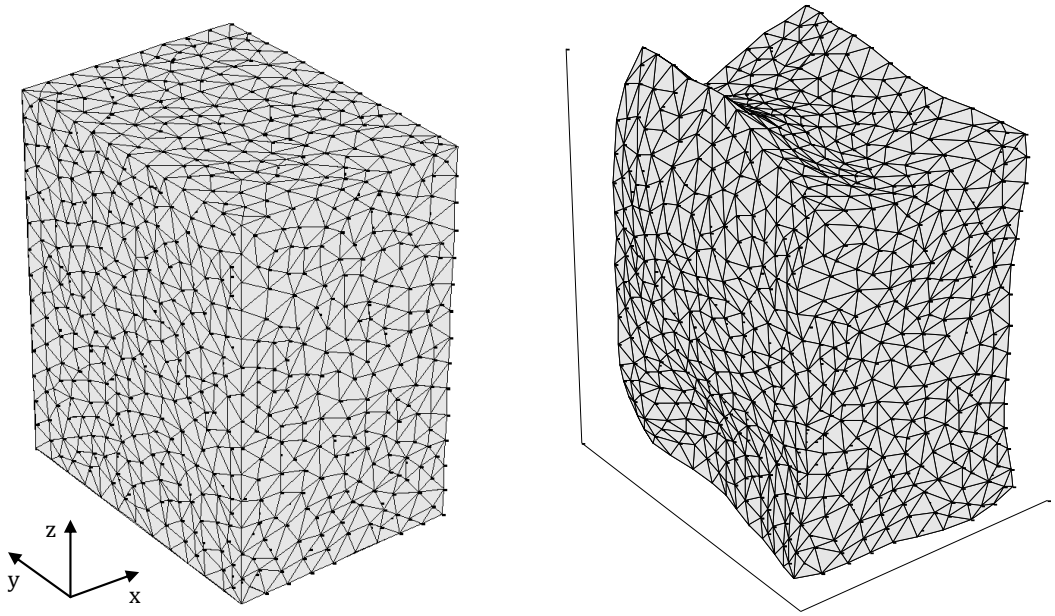

(a) Undeformed mesh

(b) Deformed mesh

Figure 4.8: Undeformed and deformed FE mesh for breast image registration.

Table 4.5: 3D-3D registration results for the *right* breast images in terms of TRE (in mm) using different similarity/distance measures. Coordinate frames are given in Figure 4.7.

Registration using	SSD	CR	NCC	MI	Before
Mean±std in x	1.62±1.36	1.75±1.48	1.7±1.36	1.62±1.31	8.65±4.52
Mean±std in y	0.67±0.49	0.76±0.54	0.7±0.51	0.61±0.50	1.83±1.79
Mean±std in z	0.66±0.44	0.52±0.43	0.67±0.48	0.66±0.49	5.50±3.70
Mean±std	2.08±1.18	2.11±1.44	2.14±1.22	2.07±1.12	11.29±4.01
Median	2.10	1.92	2.21	2.21	12.94

in Figure 4.9c. CR-based registration of the *left* breast images are shown in Figure 4.10. In this figure, images of the normal breast (Figure 4.10a) are deformed to match the images of the compressed breast (Figure 4.10b). The deformed template images are shown in Figure 4.10c and the difference between the reference images and the deformed template images are given in Figure 4.10d.

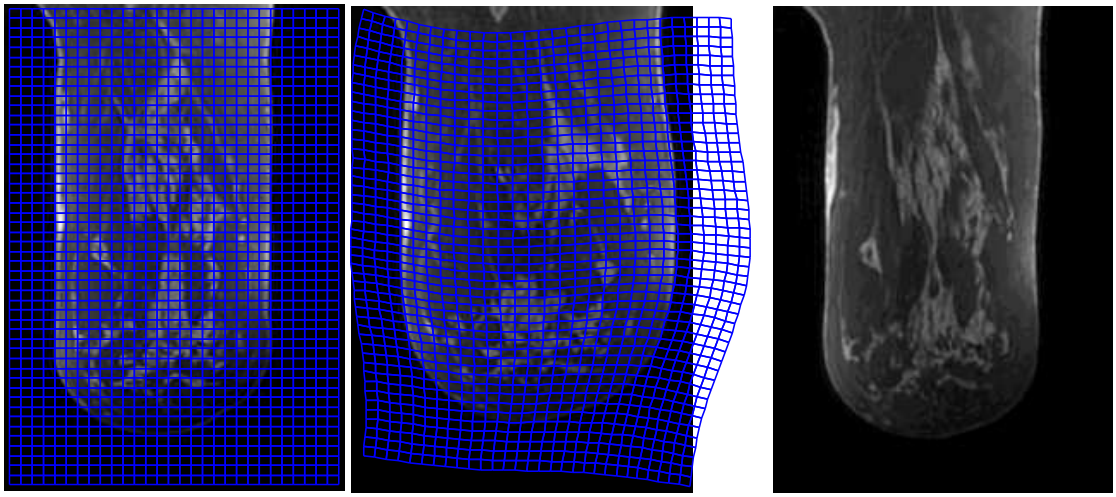

(a) (b) (c)

Figure 4.9: Reference image R with the original grid of control points (a), template image T with the deformed grid of control points (b), deformed template image $T[\mathbf{u}]$ (c); deformation of the left breast in axial plane is only shown.

Table 4.6: 3D-3D registration results for the *left* breast images in terms of TRE (in mm) using different similarity/distance measures. Coordinate frames are given in Figure 4.7.

Registration using	SSD	CR	NCC	MI	Before
Mean±std in x	1.15±0.84	1.12±0.87	1.15±0.80	1.17±0.87	10.05±5.60
Mean±std in y	1.40±1.16	1.34±1.08	1.23±1.29	1.11±0.97	2.25±2.01
Mean±std in z	2.34±2.27	2.16±2.28	2.08±1.84	2.42±2.44	8.91±6.19
Mean±std	3.47±1.88	3.31±1.88	3.17±1.57	3.39±2.07	14.78±6.11
Median	3.15	2.9	2.64	2.73	16.43

The performance of the registration method is also evaluated based on TRE. Ten pairs of evenly distributed fiducial points are identified in both uncompressed and compressed breast images (10 points for each breast) using "rview" graphical gadget of the image registration toolkit (IRTK) software package [182]. Table 4.5 and Table 4.6 summarize the average, standard deviation and median of the TRE for fiducial points in the right and the left breast images, respectively. These statistics are also given for the distances of fiducial points before the registration. As can be seen from the data in these tables, most of the

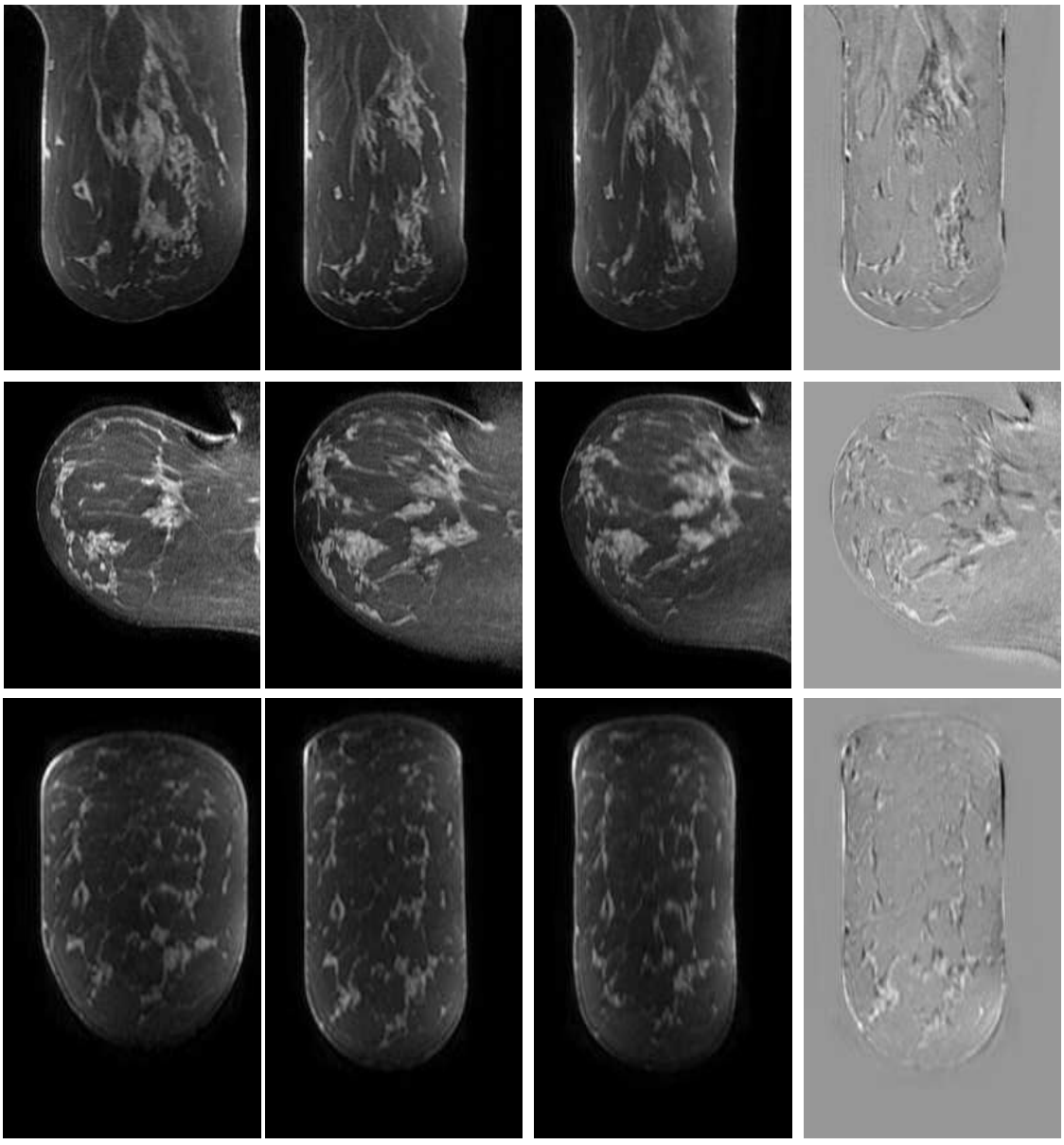

(a) (b) (c) (d)

Figure 4.10: Axial (top row), sagittal (middle row) and coronal (bottom) views of the template (a), reference (b), registered deformed template (c) and the difference images (d) in 3D-3D CR-based registration of the *left* breast images.

errors are in the x direction (the direction of compression) and z directions. Different similarity/distance measures perform almost the same in terms of TRE in the single modality

MR image registration. The average TRE in the left breast images is bigger than that of the right breast images because there is a larger compression in the left breast.

Chapter 5

Volumetric Elastic Registration of Breast MR Images Based on State Estimation for Dynamical Systems

In this chapter, the problem of non-rigid image registration is approached from a new perspective, namely "state estimation" for dynamical systems. The dynamic linear elastic deformation model, developed in Chapter 3, is assumed to describe the deformation behavior of the tissue under unknown external disturbance forces. A state estimator is developed to estimate the deformation of the tissue using an intensity-based similarity/distance metric, comparing the reference image with the predicted deformed template image. This new registration method is evaluated in volumetric registration of images from a breast phantom as well as real breast tissue.

5.1 The Registration Method

In model-based image registration, the deformation of the tissue model yields the displacement field for matching the images to each other. In the previous chapter, the deformation of the model was iteratively updated based on the forces computed from similarity/distance between the reference and template images. In this chapter, the problem of registering two set of images using a deformation model is posed as a state estimation problem. The objective is to obtain an estimate of the deformation of the actual tissue based on a model of deformation and information obtained from the reference images. To achieve this goal, the state estimator compares the reference and the deformed template images using a matching criterion to update the state estimates of the deformation.

Assume that the dynamics of the tissue deformation are governed by the following general nonlinear state-space equations in discrete-time

$$\mathbf{x}_k = a(\mathbf{x}_{k-1}, \tilde{\mathbf{f}}_{k-1}) + \mathbf{w}_{k-1} \tag{5.1a}$$

$$\mathbf{z}_k = h(\mathbf{x}_k) + \mathbf{v}_k \tag{5.1b}$$

where $\mathbf{x}_k$ is the vector of deformation states to be estimated at time step k; the state vector $\mathbf{x}$ is usually comprised of the displacement and velocities of the nodal points of a 3D FE mesh which is constructed to represent the deformable tissue. The input vector $\tilde{\mathbf{f}}$ represents external applied forces which are summed into a vector of nodal forces. In the state-space model of (5.1b), $\mathbf{z}$ is the observation or measurement vector. In the proposed image registration framework, the measurement vector $\mathbf{z}$ could be raw grayscale pixel/voxel values over the intraoperative image grid, the displacement field of the template image grid points

compared to those in the reference images, or any other form of information/feature derived from post-processing of the raw image data. $a(\cdot)$ and $h(\cdot)$ are two nonlinear vector mappings in general; $a(\cdot)$ can be obtained from the physics of tissue deformation, and $h(\cdot)$, which determines the relationship between the states of the deformation model and the measurement vector, can be defined based on the preoperative/intraoperative image formation. Moreover, the vectors $\mathbf{w}$ and $\mathbf{v}$ are process and measurement noises, and represent uncertainty/error in the deformation dynamics and imaging model, respectively.

Equations (5.1a) and (5.1b) together provide a general formulation of the deformation model. (5.1a) establishes a relation between the states of deformation at different sample times, while (5.1b) defines the mapping between the states of deformation and the measurement vector. Existing linear and nonlinear state estimation techniques can be employed to compute the unknown states of the tissue deformation based on the information obtained from the intraoperative images. The general flow of the registration algorithm based on the concept of state estimation is shown in Figure 5.1. In this approach, the current states of the tissue deformation are estimated using the physical model and the information obtained from comparing the reference and template images based on a similarity/distance measure. Combining the model and observation information in order to obtain unknown states of a dynamical system is the underlying principle of most state estimation methods. The state estimation framework presents a rather straightforward mechanism for tuning the registration algorithm based on the user's relative confidence in the deformation model versus the image observation, reflected in the choice of statistical properties for the process and measurement noises.

The registration algorithm shown in Figure 5.1 iteratively estimates the deformation of the tissue and computes the deformation of the template image T to match it as closely

as possible with the reference image R. It starts from an initial estimate of the deformation state, e.g., the initial undeformed configuration of tissue. At each time step, the current state estimate, i.e., positions and velocities of the nodal points in a FE mesh, are propagated to the next time step using the model of deformation, i.e., Equation (5.1a). The new position of any point (x, y, z) in the original undeformed image can be computed based on the predicted mesh deformation and using the interpolation (shape) functions of the element containing (x, y, z). The deformed template image $T[\mathbf{u}_k^-]$ is then projected into the space of the reference image and the resulting images are compared based on a similarity/distance measure. This comparison yields an observation prediction error based on which the deformation state estimates are updated to compute nodal point displacements of the FE mesh. The iterative algorithm continues until the relative change in the similarity/distance measure becomes less than a small number ϵ or the number iterations reaches a given maximum.

5.1.1 Model of Deformation

Biological tissues in the body have a very complex deformation behaviour that is best described by highly nonlinear models. However, developing a nonlinear model with an accurate geometry and inhomogeneous tissue structures is very difficult. It requires determination of complex boundary conditions possibly involving soft-tissue to soft-tissue interaction and applied external forces. Furthermore, regardless of their computational complexity, nonlinear state estimation methods are not as developed as their linear counterpart. Therefore, a rather simple linear elastic deformation model constructed over a volumetric cubic mesh is employed in this thesis. The state estimation framework for linear systems allows for disturbance terms in the model, representing uncertainty and modelling errors.

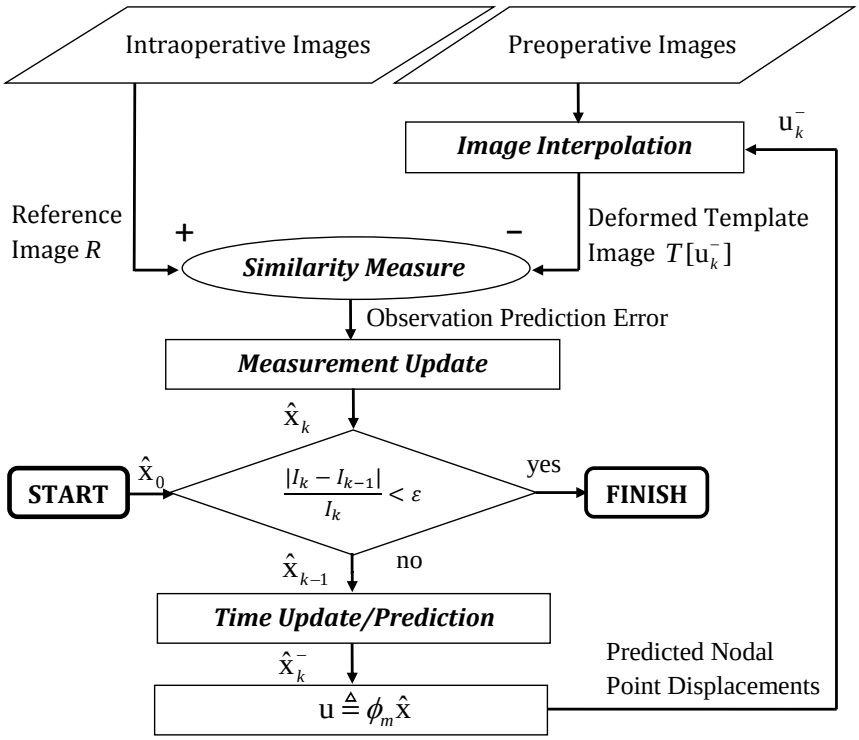

Figure 5.1: Block diagram of the iterative 3D-3D registration algorithm based on the concept of dynamic state estimation.

The aggregate error due to inaccurate geometry, unknown boundary conditions, unknown external forces, and model and parameter mismatches can be presented by the process noise vector **w**.

The general form of dynamic linear elastic deformation model is given in Equation (3.15). Fast vibrational modes of this model are disregarded using a modal analysis as discussed in Section 3.4. Only m slower modes of the decoupled equations in (3.17) are used in estimation of deformation states. The reduced model approximates the full model behaviour in a low dimension space which significantly lowers the computations involved in the algorithm and improves the efficiency and robustness of the state estimation process. The continuous-time dynamics in Equation (3.17) are transformed into discrete-time equations

with sample time of T_s, using the central difference method [26]. T_s is chosen as was explained in Equation (4.11). The discrete-time reduced dynamics can be represented in state-space form as

$$\mathbf{x}_k = \mathbf{A}\mathbf{x}_{k-1} + \mathbf{G}\tilde{\mathbf{f}}_{k-1} + \mathbf{w}_{k-1} \tag{5.2}$$

where x is the $2m \times 1$ vector of states to be estimated, $\mathbf{w}_k$ is the process noise which accounts for uncertainties in the modelling. Furthermore, $\mathbf{A}$ and $\mathbf{G}$ are defined as

$$\mathbf{A} = \begin{bmatrix} 0 & \mathbf{I} \\ -\mathbf{W}_1^{-1}\mathbf{W}_3 & -\mathbf{W}_1^{-1}\mathbf{W}_2 \end{bmatrix}; \ \mathbf{G} = \begin{bmatrix} 0 \\ -\mathbf{W}_1^{-1} \end{bmatrix} \tag{5.3}$$

with

$$\mathbf{W}_1 = \frac{\tilde{\mathbf{M}}_1}{T_s^2} + \frac{\tilde{\mathbf{C}}_1}{2T_s} \tag{5.4}$$

$$\mathbf{W}_2 = \tilde{\mathbf{K}}_1 - \frac{2\tilde{\mathbf{M}}_1}{T_s^2} \tag{5.5}$$

$$\mathbf{W}_3 = \frac{\tilde{\mathbf{M}}_1}{T_s^2} - \frac{\tilde{\mathbf{C}}_1}{2T_s} \tag{5.6}$$

where $\tilde{\mathbf{M}}_1$, $\tilde{\mathbf{C}}_1$, $\tilde{\mathbf{K}}_1$ are $m \times m$ matrices out of the original $\tilde{\mathbf{M}}$, $\tilde{\mathbf{C}}$, and $\tilde{\mathbf{K}}$ matrices corresponding to m slowest modes of the full deformation model. The sizes of $\mathbf{A}$ and $\mathbf{G}$ matrices are $2m \times 2m$ and $2m \times m$, respectively. The state-space dynamics model in Equation (5.2) is a linear version of the one in Equation (5.1a).

5.1.2 Observation Model

The observation model relates the states of the deformations model to the sensor measurements, which are the intraoperative (reference) images. This model produces the expected (predicted) deformed template image corresponding to the reference images for a given tissue deformation state. The predicted image is compared to the actual reference images and based on the computed error (observation prediction error), the predicted states are updated. For example, in a 3D-3D registration scenario, one can obtain the expected intraoperative image by interpolating the preoperative image using the deformation state of the the tissue. While conceptually simple, this sensor modelling approach may not be practical and/or straightforward in some image registration scenarios. First, the dimensions of the observation vector, i.e., the number of pixels/voxels in the image, can be excessively large leading to prohibitive computations. Second, in multiple-modality registration the mapping from the preoperative image domain (e.g., MR) to the intraoperative image domain (e.g., US) can be complex, nonlinear, and computationally intensive. Some of these issues can be addressed by pre-processing of the imaging data to extract information that is in a reduced-dimensional space and is independent of the imaging modality. Such "feature" extraction methods can reduce the dimension of the observation vector and enable comparison of preoperative and intraoperative imaging data. However, it is likely that the resulting observation model involves a nonlinear mapping from the deformation state domain to the processed observation vector, requiring application of nonlinear filtering techniques.

In this thesis, in order to simplify the observation model, the displacement at some control points, i.e., $\mathbf{x}_c$, are considered as the measurement vector. Control points in 3D-3D registration stem from a 3D regular grid in the domain of the reference image and coarser than the actual image grid. The states of the reduced dynamic model $\mathbf{x}$ are mapped to the

nodal displacements of the FE mesh using the relation $\mathbf{u} = \phi_m \mathbf{x}$ in which ϕ_m is formed of m columns of ϕ that correspond to m slowest modes of the original model. The displacements of the control points $\mathbf{u}_c$ then can be computed based on the displacements of the nodal points of the FE mesh using the elements interpolation functions in (3.7), i.e.,

$$\mathbf{u}_c = \mathbf{\Lambda u} = \mathbf{\Lambda} \phi_m \mathbf{x} \tag{5.7}$$

where $\mathbf{\Lambda}$ is assembled from the elements shape functions for individual points and $\mathbf{u}$ is the nodal points displacement vector of the FE mesh. With this representation, the observation model can be expressed as

$$\mathbf{z}_k = \mathbf{u}_c = \mathbf{H}\mathbf{x}_k + \mathbf{v}_k \tag{5.8}$$

$$\mathbf{H} \triangleq \mathbf{\Lambda} \phi_m \tag{5.9}$$

where $\mathbf{v}_k$ is measurement noise. The output matrix $\mathbf{H}$ is a $3n \times 2m$ matrix with n equal to the number of control points. The observation model in Equation (5.8) is also a linear version of the one in Equation (5.1b). The spacing of the control points which determines the length of the measurement vector (i.e., $3n$) can be chosen by the user depending on the registration application requirements. However, the main question remains as how to process intraoperative and preoperative images to obtain the measurement vector $\mathbf{z}_k$, which will be answered in the next subsection.

5.1.3 State Estimation

The state (5.2) and observation model (5.8) together are in standard form for application of a discrete-time linear state estimator such as the *Kalman* filter [183]. This iterative estimation process involves two different updates. The time update provides an *a priori* estimate of the states, i.e., $\hat{\mathbf{x}}_k^-$ given knowledge of the process prior to that time. The measurement update computes an *a posteriori* state estimate, i.e., $\hat{\mathbf{x}}_k$, as a linear combination of the *a priori* estimate $\hat{\mathbf{x}}_k^-$ and a weighted difference between the actual measurement vector $\mathbf{z}_k$ and the measurement prediction [183]. The equations for the time and measurement updates of the filter are presented in Table 5.1. Here Γ_k is the Kalman gain, $\mathbf{P}_k^-$ and $\mathbf{P}_k$ are *a priori* and *a posteriori* estimate error covariance matrices, and $\mathbf{Q}$ and $\mathbf{S}$ are process and measurement noise covariance matrices. In (5.2), the term $\tilde{\mathbf{f}}$ is due to the applied forces $\mathbf{f}$ on the tissue and is usually unknown; it is modelled as part of the process disturbance $\mathbf{w}$ as white Gaussian noise with a normal probability distribution of $p(\tilde{\mathbf{f}}) = N(0, \mathbf{Q})$. The power of the process noise reflects the user confidence in the accuracy of the model, i.e., the stronger the noise is the less accurate the model is.

The state estimates are updated based on the observation prediction error, i.e., $\mathbf{z}_k - \mathbf{H}\hat{\mathbf{x}}_k^-$, using $\hat{\mathbf{x}}_k = \hat{\mathbf{x}}_k^- + \Gamma_k(\mathbf{z}_k - \mathbf{H}\hat{\mathbf{x}}_k^-)$ where Γ_k is the filter gain. In the context of image registration, the measurement vector in Equation (5.8) is the displacement of the control points from their initial positions. The measurement vector and its prediction need to be

Table 5.1: Time and measurement updates of the discrete time state estimator.

Time Update/Prediction	Measurement Update
$\hat{\mathrm{x}}_k^- = \mathrm{A}\hat{\mathrm{x}}_{k-1}$	$\Gamma_k = \mathrm{P}_k^-\mathrm{H}^t\left(\mathrm{H}\mathrm{P}_k^-\mathrm{H}^t + \mathrm{S}\right)^{-1}$
$\mathrm{P}_k^- = \mathrm{A}\mathrm{P}_{k-1}\mathrm{A}^t + \mathrm{Q}$	$\hat{\mathrm{x}}_k = \hat{\mathrm{x}}_k^- + \Gamma_k(\mathrm{z}_k - \mathrm{H}\hat{\mathrm{x}}_k^-)$
	$\mathrm{P}_k = (\mathrm{I} - \Gamma_k\mathrm{H})\mathrm{P}_k^-$

calculated based on the reference and the deformed template images. Instead of calculating these two vectors separately and then subtracting them to compute the error, a method is employed to directly *approximate* the observation prediction error based on the image similarity/distance measures.

Many registration methods work based on the principle of increasing similarity/reducing distance between two images. This is often achieved through formulating and solving an optimization problem with a cost function that consists of the similarity/distance measure plus a regularization term. Focusing on the similarity/distance measure and ignoring the regularization term, a deformation correction along the gradient of the similarity/distance measure would represent a step in the gradient-decent search towards the minimum of the similarity/distance measure. This is also equivalent to finding the optical flow field between the reference R and template T images based on the employed similarity/distance measure. This search direction can be used as an approximate observation prediction error in the state estimation framework. In an ideal case, i.e., a convex function over a convex set, a few steps in the negative direction of the gradient with a proper step size would lead to optimizing the similarity/distance measure between the two images.

Assume that a control point in the domain of the reference image R is represented by (x_r, y_r, z_r) and its corresponding point in the domain of the template T image is (x_t, y_t, z_t). The observation prediction error is basically the displacement needed to apply to predicted control points in the domain of template image T, i.e., (x_t^-, y_t^-, z_t^-), in order to match the reference image R at (x_r, y_r, z_r) with the template image T at (x_t, y_t, z_t). This correction displacement is computed based on the gradient of the similarity/distance measure at control

points as

$$\mathbf{dx}_c = \mathbf{z}_k - \mathbf{H}\hat{\mathbf{x}}_k^- = -\frac{1}{\gamma}\nabla I_{\mathbf{x}_c}(R, T[\mathbf{u}_k^-]) \tag{5.10}$$

where $\mathbf{u}_k^- = \phi_m \hat{\mathbf{x}}^-$ is the predicted nodal point displacements of the FE mesh and $T[\mathbf{u}_k^-]$ is the predicted deformed template image. A variational approach for computing the gradient of several well-established similarity/distance measures was discussed in Section 4.2, see Equation (4.3), Table 4.1 and Table 4.2.

It is worth pointing out that the choice of the steepest descent direction with a tunable gain γ is not the only or the best possible approximation for the observation prediction error. Alternatively, one can run a full optimization loop trying to optimize the similarity/distance measure between the two images at the current estimation time step and use the final displacement correction as the observation prediction error. While this latter process would likely produce more accurate results, it would also be much more computationally intensive.

Equations (5.2) and (5.8) represent the deformation and the observation models and both are linear. In 3D-3D registration, control points in the reference image R domain are fixed and do not change in the iterative registration algorithm. Therefore, the output matrix $\mathbf{H}$ is fixed which makes the deformation and the observation models time-invariant. In such case, the steady-state Kalman gain Γ can be computed off-line and used in the registration, eliminating the need for on-line calculation of of the time-varying gain in Table 5.1 [184]. This would reduce the on-line computations of the algorithm. To compute the Kalman gain,

process **Q** and measurement noise **S** covariances are given as

$$\mathbf{Q} = q\, I_{2m\times 2m} \tag{5.11}$$

$$\mathbf{S} = s\, I_{3n\times 3n} \tag{5.12}$$

where I is an identity matrix, m is the number of vibrational modes used in the reduced model, and n is the number of control points; q and s determine the power for the process and measurement noises respectively. It is the relative power of the process and measurement noises, i.e., q/s that determines the Kalman gain. The choice of q/s depends on the user's relative confidence in the deformation model versus the observation obtained from the similarity/distance measure between images. Since the linear elastic FE model is developed for small deformations, it would not be accurate for large deformations. In this case a larger q/s should be considered to account for the modelling uncertainty and inaccuracy. Noisy images with artifacts especially in multi-modality registration would increase the uncertainties in the computation of the approximate observation prediction error. In this case the q/s needs to be decreased to accounts for the effect of the uncertainties in image measurements.

Other than q/s, γ is another tuning parameter that determines the size of the observation prediction error in Equation (5.10). The Kalman gain, which is computed offline for a given q/s, can be used for all image data sets from the same type, e.g., breast compression MR images. The registration algorithm can be further tuned by adjusting γ for different data sets or different similarity/distance measures.

At the end of the iterative process, the deformation model reaches at an equilibrium with a nodal point displacements vector of **u**. It is shown in Appendix B that the steady-state

equilibrium equation becomes

$$\mathbf{K}\mathbf{u} = -\frac{1}{\gamma}\mathbf{M}\Gamma_2\nabla I_{\mathbf{x}_c}(R, T[\mathbf{u}_k^-]). \tag{5.13}$$

where $\Gamma = [\Gamma_1; \Gamma_2]$. Comparing this equation with Equation (4.9), it can be concluded that the left side of the equations is $\mathbf{K}\mathbf{u}$ in both cases. The only difference is in the image derived forces that are applied to the elastic body to establish a balance between the internal and external forces. Therefore, similar to Equation (4.9), at the steady-state equilibrium, the internal strain-stress forces of the model are in a balance with the external applied forces which are derived from the similarity/distance measure between images. Tuning γ in Equation (5.13) is basically equivalent to the tuning of the weighting factor of the regularization function in the cost function given in (2.2).

5.1.4 Step by Step Description of the Registration Algorithm

The proposed state estimation-based registration algorithm involves the following steps.

1. *Time Update/Prediction*: At each iteration, the vector of state estimates from the previous step $\hat{\mathbf{x}}_{k-1}$ is updated to $\hat{\mathbf{x}}_k^-$ according to the time update equation, $\hat{\mathbf{x}}_k^- = \mathbf{A}\hat{\mathbf{x}}_{k-1}$. This is the vector of predicted deformation states of the tissue based on which the predicted displacements for the nodal points of the FE mesh can be computed using $\mathbf{u}_k^- = \phi_m\hat{\mathbf{x}}_k^-$.

2. *Find Deformed Grids*: The deformation for the grid of control points is computed based on the deformation of the FE mesh using elements' interpolation function. This would provide the predicted position of the control points in the domain of the template image T. The deformation for grid of template image is also computed similarly.

3. *Interpolate the Predicted Deformed Template Image*: The predicted image grid in the

previous step is used to compute the predicted deformed template image $T[\mathbf{u}_k^-]$ from the template image data using the trilinear interpolation method.

4. *Compute the Observation Prediction Error*: The observation prediction error is computed at control points using Equation (5.10).

5. *Measurement Update*: The state estimates are updated based on the observation prediction error using $\hat{\mathbf{x}}_k = \hat{\mathbf{x}}_k^- + \Gamma \mathbf{d}\mathbf{x}_c$ where Γ is the steady-state Kalman gain. This gain is computed offline.

The algorithm terminates when the relative change in the similarity/distance measure between the reference R and the deformed template image $T[\mathbf{u}]$ (i.e., $I(R, T[\mathbf{u}])$) is less than a given small number ε, i.e., $|I_k - I_{k-1}|/I_k < \varepsilon$, or the total iterations exceeds a maximum number. At the end of the iterations, a deformed template image $T[\mathbf{u}]$ with the resolution of the actual preoperative image is computed in the similar way explained in steps 2 and 3 of the algorithm.

5.2 Experiments and Results

5.2.1 Registration of 3D MR Images of a Breast Phantom

In this section, high-resolution 3D MR images of a breast phantom are registered to its compressed high and low resolution 3D images using the proposed registration method. Details on acquiring high and low-resolution MR images of the compressed and uncompressed breast phantom were given in Section 4.3.1. Also, the same FE dynamic model as the one in Section 4.3.1 is used here.

The control points are from a 20×30×10 grid inside the domain of reference image R and the image grid is 40×60×20. The output matrix and the time-invariant observation model in (5.8) are constructed based on the grid of control points. The Kalman gain is computed offline. For this experiment, $q/s = 10000$ and γ is manually tuned to achieve a desirable outcome. A 3D Gaussian filter with a variable standard deviation σ is employed to smoothen the image for the computation of the gradient of the template image $\nabla T[\mathbf{u}]$. Similar to the experiments in Chapter 4, the registration algorithm starts with a 23×23×23 kernel and $\sigma = 5$ and reduces to a 3×3×3 kernel with $\sigma = 0.5$ towards the end. The size of the reduced dynamic model is $m = 500$ where only 5.4% of modes of the full deformation model are considered in the dynamic model. Furthermore, the number of bins $N = 32$ in this experiment.

Using the proposed algorithm, uncompressed phantom images are registered to its compressed high- and low resolution images separately based on four different similarity/distance measures. The same observation model and Kalman gain are employed in both experiments and γ is tuned to achieve acceptable outcomes using different similarity/distance measures. In Figure 5.2, the result of registering high-resolution uncompressed images (template) to low-resolution compressed images (reference) are depicted in which NCC is employed as the similarity/distance measure. In this figure, three different views of the template (a), reference (b), deformed template (c) and the difference images (d) are given. The difference image is the intensity difference between the high-resolution compressed breast images and the deformed template image.

The registration results based on TRE for eight pairs of manually identified fiducial points are given in Table 5.2 and Table 5.3. The image axes are shown in Figure 4.2a. Fiducial points are mostly chosen in the center of cystic masses in the images using 3DSlicer [181].

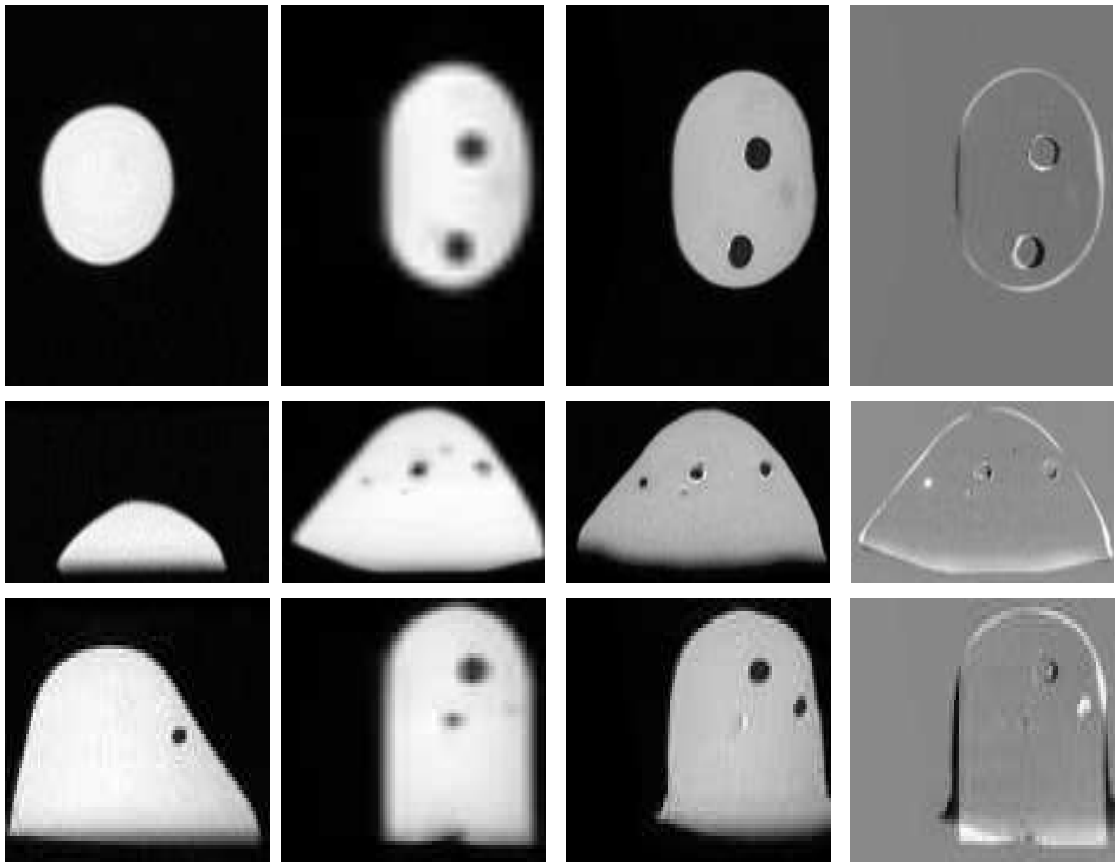

(a) (b) (c) (d)

Figure 5.2: Coronal (top row), axial (middle row) and sagittal (bottom row) views of the template (a), reference (low-resolution) (b), registered deformed template (c) and the difference images (d) in 3D-3D NCC-based registration of the breast phantom image data using the method of state estimation for dynamical models.

In 3DSlicer, template and reference images can be visualized together in three different views. Pairs of fiducial points can be identified, chosen and saved as a text file. Then, the deformation field, computed from registration of images, can be applied to the points in the coordinate of the template image. The TRE is computed as the RMS distance between the deformed points and their pairs in the reference image coordinates.

Table 5.2 shows the registration results when high-resolution compressed phantom images are considered as reference images, and Table 5.3 presents the results of low-resolution reference images. In these tables, the average (mean), standard deviation (std) and median of distances between fiducial points before and after the registration are given. It can be concluded from these results that the average TRE is decreased from about 15.3 mm before registration to about 2.4 mm after registration using high-resolution reference images, and to about 3.3 mm using low-resolution images. It is also evident from these tables that CR and NCC-based registration outperform those based on SSD and MI.

Table 5.2: 3D-3D registration results in terms of TRE (in mm) using different similarity/distance measures. Reference images are *high-resolution* compressed phantom images. Coordinate frames are given in Figure 4.2a.

Registration using	SSD	CR	NCC	MI	Before
Mean±std in x	2.11±1.73	1.64±1.29	1.35±1.24	1.91±1.44	14.70±1.72
Mean±std in y	0.78±0.45	0.61±0.56	0.51±0.48	0.61±0.50	2.85±1.91
Mean±std in z	1.17±0.95	0.89±0.77	0.84±0.83	1.17±1.23	2.08±1.43
Mean±std	2.77±1.66	2.20±1.23	1.89±1.27	2.69±1.33	15.31±1.37
Median	2.24	2.02	2.1	2.93	15.82

Table 5.3: 3D-3D registration results in terms of TRE (in mm) using different similarity/distance measures. Reference images are *low-resolution* compressed phantom images. Coordinate frames are given in Figure 4.2a.

Registration using	SSD	CR	NCC	MI	Before
Mean±std in x	3.22±1.49	2.29±1.58	1.87±1.37	3.38±1.57	14.70±1.72
Mean±std in y	0.72±0.66	0.59±0.28	0.60±0.43	0.85±0.72	2.85±1.91
Mean±std in z	0.93±0.81	1.14±0.83	1.07±0.99	1.05±0.75	2.08±1.43
Mean±std	3.69±1.09	2.93±1.18	2.59±1.08	3.9±1.14	15.31±1.37
Median	3.2	2.74	2.42	3.67	15.82

Comparing the results in Table 5.2 and Table 5.3 to those of Table 4.3 and Table 4.4, the state estimation-based registration in this chapter and the registration method proposed in Chapter 4 perform similarly in terms of average TRE for the same fiducial points. However,

the real-time computational load involved in the state estimation-based registration method is less than that of the method proposed in Chapter 4. However, it will be shown in next two chapters that the state estimation-based registration approach yields a unified framework for co-registration of images of different dimensinality, i.e., 3D-2D registration.

5.2.2 Registration of MR images of Real Breast Tissue

Volumetric MR images of normal and compressed actual breasts are registered together in this section using the state estimation-based registration method. The breast MR images are identical to those of the previous chapter, which have been acquired under uncompressed and compressed conditions (see Section 4.3.2 for more details). Also, the same FE mesh and the deformation model are employed here. Registration algorithm is applied to right and left breast images separately and the experimental results on both image data sets are reported.

The size of the employed reduced dynamic model is $m = 500$ where only 3.96% of modes of the full deformation model is considered in the dynamic model. In the computation of the gradient of the template image $\nabla T[\mathbf{u}]$, a smoothing Gaussian kernel with variable standard deviation σ is employed to reduce noise and control the amount of details used in each iteration. A regular grid of 30×40×40 is considered as control points in which the observation prediction errors are computed. An image grid of 60×80×80 is also used in the iterative registration algorithm. This resolution for images in the registration algorithm provides a good balance between the registration quality and the computational load. NCC-based registration of the *right* breast images are shown in Figure 5.3. In this figure, images of the normal breast (Figure 5.3a) are deformed to match the images of the compressed breast (Figure 5.3b). The deformed template images are shown in Figure 5.3c and

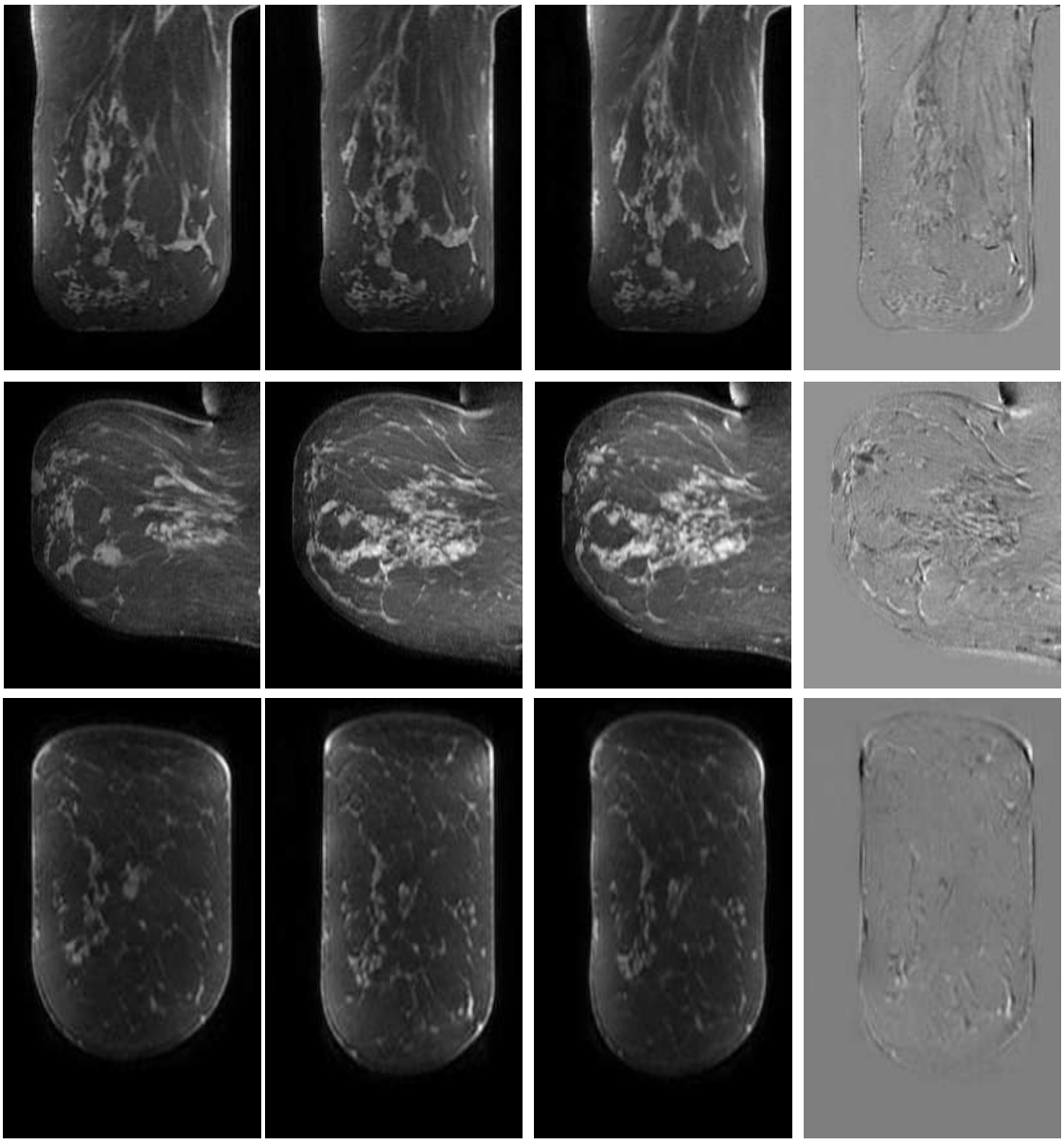

(a) (b) (c) (d)

Figure 5.3: Axial (top row), sagittal (middle row) and coronal (bottom) views of the template (a), reference (b), registered deformed template (c) and the difference images (d) in 3D-3D MI-based registration of the *right* breast images using the method of state estimation for dynamical models.

the difference between the reference images and the deformed template images are given in Figure 5.3d.

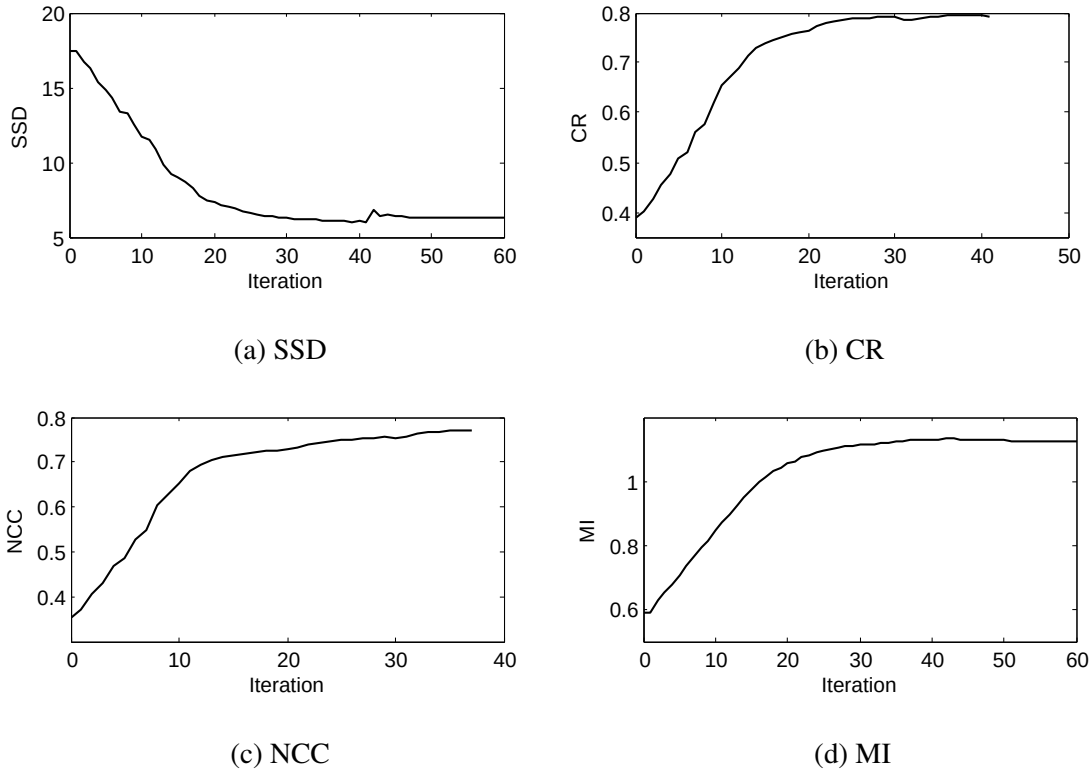

(a) SSD (b) CR

(c) NCC (d) MI

Figure 5.4: The evolution of the similarity/distance measures in the iterative registration of breast images. Number of bins $N = 32$.

The iterative evolution of four similarity/distance measures based on which the registration is performed are shown as a function of iteration number in Figure 5.4. The CR and NCC-based registrations are terminated before reaching the maximum number of iterations (i.e., 60). All values in this figure are computed based on the formula given in Table 4.1 except for SSD which is normalized by the number of voxel points. Number of bins for computing the joint histogram of images and the similarity/distance measures is $N = 32$. Furthermore, to obtain displacement of the control points $\mathbf{dx}_c$, the joint histogram function is smoothed using a 2D Gaussian filter.

Registration results in terms of TRE for ten fiducial points are given in Table 5.4 and Table 5.5 for the right and left breast images, respectively. It is evident form these results

Table 5.4: 3D-3D registration results for the *right* breast images in terms of TRE (in mm) using different similarity/distance measures. Coordinate frames are given in Figure 4.7.

Registration using	SSD	CR	NCC	MI	Before
Mean±std in x	1.53±1.48	1.47±1.36	1.46±1.48	1.58±1.63	8.65±4.52
Mean±std in y	0.69±0.39	0.55±0.43	0.62±0.41	0.75±0.35	1.83±1.79
Mean±std in z	0.77±0.65	0.73±0.62	0.67±0.57	0.79±0.65	5.50±3.70
Mean±std	2.08±1.32	1.95±1.24	1.95±1.34	2.15±1.48	11.29±4.01
Mean±std (IRTK)	2.35±1.21	2.32±1.37	2.29±1.50	2.07±1.10	11.29±4.01
Median	1.79	1.78	1.65	1.6	12.94

Table 5.5: 3D-3D registration results for the *left* breast images in terms of TRE (in mm) using different similarity/distance measures. Coordinate frames are given in Figure 4.7.

Registration using	SSD	CR	NCC	MI	Before
Mean±std in x	1.35±1.18	1.27±1.10	1.27±1.27	1.03±0.95	10.05±5.60
Mean±std in y	0.66±0.60	0.70±0.60	0.67±0.52	0.75±0.60	2.25±2.01
Mean±std in z	2.28±1.99	2.23±1.93	2.16±1.40	2.42±2.16	8.91±6.19
Mean±std	3.11±1.80	2.98±1.81	2.87±1.48	3.02±2.01	14.78±6.11
Mean±std (IRTK)	3.94±2.24	2.88±1.92	2.75±1.65	2.92±1.82	14.78±6.11
Median	2.78	2.62	2.26	2.15	16.43

that four different similarity/distance measures yield very similar TREs. The reason for better performance of MI in actual breast images in comparison with the phantom images is the richer information content of the real tissue images, which provides a disperse joint histogram between images. It can be also concluded from these tables that the average TRE is decreased from about 11.3 mm and 14.8 mm before registration to about 2.0 mm and 3.0 mm after registration in the right and left breast images, respectively. Considering the voxel size of the image data, i.e., 0.7×0.7×1.1 mm, the average TREs in x,y, and z directions are reasonable in both right and left breast images. The average TRE is almost twice the voxel size in x, and z directions and it is almost the size of the voxel in y direction.

The registration results in this section are also compared to those of the IRTK [182].

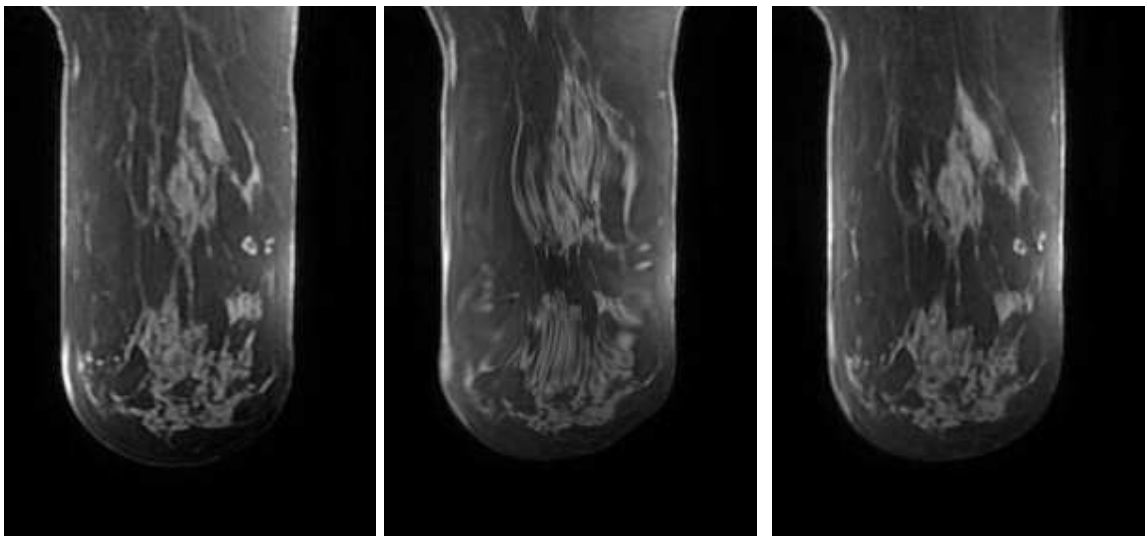

(a) (b) (c)

Figure 5.5: An axial view of the reference (a), and the deformed template image using IRTK method (b), and state estimation-based method (c) in the left breast images.

IRTK is one of the well-established deformable image registration tools which originally was developed for non-rigid registration of breast MR images. As discussed in Section 2.4, IRTK uses a free-form deformation based on B-splines for non-rigid registration [8]. For this experiment, the IRTK algorithm is implemented at three resolution levels. The control points spacing is chosen as 30, 40 and 40 in x, y and z direction, respectively, which is identical to the resolution of the grid of control points used as the vector of observation prediction error in the proposed method of this thesis. IRTK employs the gradient descent method for optimization and linear interpolation mode for registration. It is evident from Table 5.4 and Table 5.5 that the result of the state estimation-based registration method are similar to those of IRTK in terms of average TRE. IRTK performs better in MI-based registration than the state estimation-based registration method, while it performs poorly in SSD-based registration.

Qualitatively, the IRTK algorithm is more effective on the boundaries of the breast tissue while the proposed method in this thesis performs better in the internal region of the breast tissue, e.g., see Figure 5.5. As is shown in Figure 5.5b, IRTK produces unrealistic deformations for internal structures in some cases especially in the left breast image data which has undergone a larger deformation. To fix this problem, weighting values for regularization penalty terms need to be increased. However, this degrades the algorithm performance especially on the edges and increases the TRE. To achieve the results in Table 5.4 and Table 5.5, the regularization weights are tuned to minimize the TRE.

Chapter 6

Registration of 3D Images to a Sequence of 2D Images with Static Deformation

In this chapter, the state estimation-based registration method is further developed to register 3D preoperative images to a sequence of 2D intraoperative images with static deformations. The states of tissue deformation are estimated using a limited number of intraoperative images acquired from different orientations. The developed registration method is evaluated in the registration of the breast phantom as well as real breast MR images.

6.1 Background and Motivation

Registration of preoperative diagnostic and planning image volumes to 2D intraoperative images is of great importance in image-guided biopsies and interventions. Acquiring real-time 3D high-resolution intraoperative images is not possible due to technological shortcomings, incompatibility of imaging equipment with surgical tools, and the long acquisition and processing times. Among existing imaging modalities, MRI has superior performance in differentiating soft-tissue structures, and has very few harmful effects on both

the patient and the operator compared to, for example X-ray imaging. Therefore, interventional MRI systems have become the modality of choice for minimally invasive surgeries and image-guided biopsies where soft tissue is involved.

Interventional MRI systems, however, provide one or a few image slices from certain orientations covering a limited area of the body during the operation. Also, the SNR of intraopertive images are lower than that of diagnostic images due to the weaker magnetic field of the open magnets used in interventional MRI systems [15]. Registration of high-resolution preoperative MR volumes to one or a few 2D intraoperative images could be instrumental in updating surgical plans and localizing the target during the operation. In image-guided biopsy, it can potentially improve the target hit rate and reduce the duration of the intervention [185].

In most of the prior work, the intraoperative image slices are registered either separately or all together to the preoperative volume using a rigid transformation. The registration framework based on state estimation for dynamical systems proposed in this thesis provides the possibility of spatially correlating image information from different directions and cross-sections of the body. Using this method, the preoperative volume can be non-rigidly updated using the deformation model to match sparse intraoperative image slices. The Kalman filtering approach for estimating deformation states would allow considering the effect of intraoperative image noise and motion artifact as measurement noise.

6.2 The Registration Method

The method for 3D-2D registration is based on the same general framework presented in Chapter 5. Similar to experiments in Chapter 5, it is assumed here that the tissue undergoes a static deformation between imaging sessions. This means that, although the tissue is

deformed between pre and intraoperative imaging sessions, it remains static during the time intraoperative images are acquired. The only difference in the registration methods of this chapter and that of Chapter 5 is in the definition of the observation model which depends on the position and orientation of the intraoerative image slices. The grid of control points is defined on the plane of intraoperative 2D image slices. Since the position and orientation of the intraoperative images might change in different registration problems, the observation model would not be time-invariant. Therefore, the steady-state Kalman gain can not be used in this case. Instead, the Kalman gain is updated along with other matrices at each iteration according to the time and measurement update equations given in Table 5.1.

In time-varying systems, other than process $\mathbf{Q}$ and measurement noise $\mathbf{S}$ covariances, an initial value for the *a posteriori* estimate error covariance matrix $\mathbf{P}_k$ should be provided. This matrix is usually given as a diagonal matrix as

$$\mathbf{P}_0 = p\, I_{2m\times 2m} \tag{6.1}$$

where I is an identity matrix and m is the number of vibrational modes used in the reduced dynamic model. $\mathbf{P}_0$ is a measure of the estimated accuracy of the initial state estimates. As given in Table 5.1, the Kalman Γ_k at each iteration is computed using following equation.

$$\Gamma_k = \mathbf{P}_k^- \mathbf{H}^t \left(\mathbf{H}\mathbf{P}_k^- \mathbf{H}^t + \mathbf{S}\right)^{-1} = \frac{\mathbf{P}_k^- \mathbf{H}^t}{\mathbf{H}\mathbf{P}_k^- \mathbf{H}^t + \mathbf{S}} \tag{6.2}$$

Looking at Equation (6.2), as the measurement error covariance $\mathbf{S}$ approached zero, the Kalman gain Γ_k weights more heavily the actual image measurement $\mathbf{z}_k$ in the measurement

update, i.e.,

$$\lim_{\mathbf{S}\to 0} \Gamma_k = \mathbf{H}^{-1} \quad \Rightarrow \quad \lim_{\mathbf{S}\to 0} \hat{\mathbf{x}}_k = \lim_{\mathbf{S}\to 0} \hat{\mathbf{x}}_k^- + \Gamma_k(\mathbf{z}_k - \mathbf{H}\hat{\mathbf{x}}_k^-) = \mathbf{H}^{-1}\mathbf{z}_k \tag{6.3}$$

On the other hand, as the *a priori* estimate error covariance $\mathbf{P}_k^-$ approaches zero, the Kalman gain Γ_k weights the observation prediction error less heavily and gives more weights to the dynamics of the deformation model, i.e.,

$$\lim_{\mathbf{P}_k^-\to 0} \Gamma_k = 0 \quad \Rightarrow \quad \lim_{\mathbf{P}_k^-\to 0} \hat{\mathbf{x}}_k = \lim_{\mathbf{P}_k^-\to 0} \hat{\mathbf{x}}_k^- + \Gamma_k(\mathbf{z}_k - \mathbf{H}\hat{\mathbf{x}}_k^-) = \hat{\mathbf{x}}_k^- = \mathbf{A}\hat{\mathbf{x}}_{k-1} \tag{6.4}$$

In other words, when the *a priori* estimate error covariance $\mathbf{P}_k^-$ has larger values than the measurement error covariance $\mathbf{S}$, the actual image measurement $\mathbf{z}_k$ is trusted more than the predicted measurement $\mathbf{H}\hat{\mathbf{x}}_k^-$. Initial state estimates are considered to be zero in all experiments. Since the initial state estimates (positions and velocities of the FE mesh nodal points) are not accurate, the covariance matrix $\mathbf{P}_0$ should be initialized with a suitably large number p on its diagonal. In this case, at the beginning of the iterative estimation process, the filter would prefer the information of the actual image measurement over the information already in the model, i.e., zero displacements and velocities. However, $\mathbf{P}_0$ should not be too large in which case the dynamics of the deformation model will be ignored.

Before starting the non-rigid 3D-2D iterative registration, the coordinates of the reference and template images are co-registered using a rigid transformation. This registration can be done based on fiducial markers that are seen in both pre and intraoperative images. Therefore, for any 2D reference image slice (intraoperative image), its transformed grid to the coordinates of the template image (preoperative image volume) is the best initial match before deformable registration. In other words, the 2D image interpolated from the volume

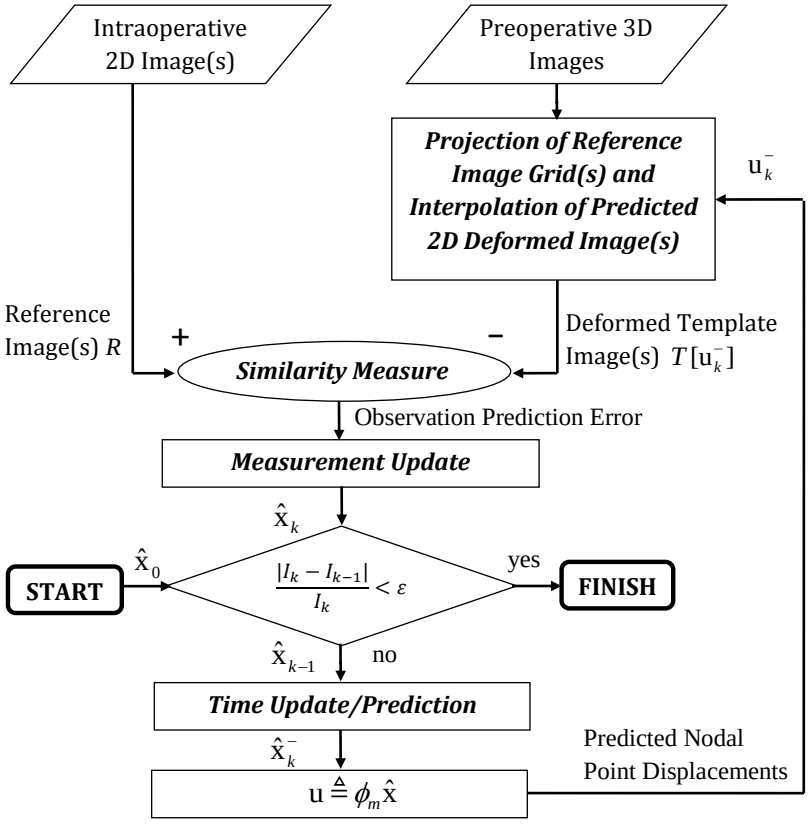

Figure 6.1: Block diagram of the iterative 3D-2D registration algorithm with static tissue deformation based on the concept of dynamic state estimation.

of the template image at transformed 2D image grid is the corresponding image slice to the 2D reference image.

The flow of the iterative registration algorithm is given in Figure 6.1 which is slightly changed with respect to Figure 5.1. The registration steps of the proposed registration algorithm are as follows.

1. *Time Update/Prediction*: At each iteration, the vector of state estimates from the previous step $\hat{\mathbf{x}}_{k-1}$ is updated to $\hat{\mathbf{x}}_k^-$ according to the time update equation, i.e., $\hat{\mathbf{x}}_k^- = \mathbf{A}\hat{\mathbf{x}}_{k-1}$.

This is the vector of predicted deformation states based on which the predicted displacements for the nodal points of the FE mesh can be computed using $\mathbf{u}_k^- = \phi_m \hat{\mathbf{x}}_k^-$. The *a priori* estimate error covariance matrix $\mathbf{P}_k^-$ is also updated in this step using the equation given in Table 5.1. The update of $\mathbf{P}_k^-$ was not required in 3D-3D registration (Chapter 5) since the steady-state Kalman gain was computed before starting the iterative algorithm.

2. *Find Deformed Image Grids*: For any 2D intraoperative slice (the reference image), the deformation of the image grid is computed based on the predicted deformation of the FE mesh using elements interpolation function. Then, the deformed mesh is transformed to the coordinates of the template image.

3. *Interpolate the Predicted Deformed Template Images*: The deformed image grids in the previous step are used to compute the predicted deformed template 2D images $T[\mathbf{u}_k^-]$ from the preoperative image volume using the trilinear interpolation method.

4. *Compute the Observation Prediction Error*: In 3D-2D registration, instead of using a separate control points grid, some of the image grid points are considered as control points at which the observation prediction errors are computed. This eliminates the extra computations needed to deform a separate control points grid. The observation prediction errors are computed at control points using Equation (5.10). Based on the formula given in Equation (4.3) for the computation of the gradient of the similarity/distance measure, Equation (5.10) can be rewritten as

$$\mathbf{dx}_c = \mathbf{z}_k - \mathbf{H}\hat{\mathbf{x}}_k^- = -\frac{1}{\gamma} g(T[\mathbf{u}_k^-], R)\, \nabla T_{\mathbf{x}_c}[\mathbf{u}_k^-] \tag{6.5}$$

Here, $g(T[\mathbf{u}_k^-], R)$ is a scalar and $\nabla T_{\mathbf{x}_c}[\mathbf{u}_k^-]$ is a 3×1 vector at each control point. Since the direction of the computed displacement at each control point depends on the gradient of

the template image (the 3D volume) at that point, the computed observation prediction error is not restricted to the plane of the 2D intraoperative image. This makes it possible to compute out of plane displacement vectors to update the state estimates.

5. *Measurement Update*: The state estimates are updated based on the vector of observation prediction errors using $\hat{\mathbf{x}}_k = \hat{\mathbf{x}}_k^- + \Gamma_k \mathbf{dx}_c$ where Γ_k is the update Kalman gain at iteration k. The Kalman gain Γ_k and the *a posteriori* estimate error covariance matrix $\mathbf{P}_k$ are updated using the equations in Table 5.1. It should be noted that, the update of Γ_k and $\mathbf{P}_k$ are not required when the steady-state Kalman gain is computed before starting the iterative algorithm, e.g., in 3D-3D registration.

The iterative algorithm terminates when the relative change in the similarity/distance measure between the 2D reference R images and their corresponding 2D deformed template images $T[\mathbf{u}]$ (i.e., $I(R, T[\mathbf{u}])$) is less than a given small number ε, i.e., $|I_k - I_{k-1}|/I_k < \varepsilon$, or the total iterations exceeds a maximum number.

At the end of the iterative algorithm, the whole volume of template images (preoperative images) can be deformed based on the estimated tissue deformation. Deformation of the 3D grid (with desired resolution for the image volume) in the coordinates of the reference image is computed based on the deformation of the FE mesh using elements interpolation (shape) function. The deformed grid is transformed to the coordinates of the template image using the rigid transformation for coordinates matching. Finally, the deformed template image is interpolated at deformed grid points from the preoperative (template) image volume. As discussed in Chapter 2, in backward mapping, the regular grid of the reference image is transformed to the coordinates of the template image using the inverse of the estimated tissue deformation. In this thesis, the inverse of the tissue deformation is directly estimated using the FE-based deformation model.

6.3 Experiments and Results

6.3.1 Registration of 3D MR Images of a Breast Phantom to a Sequence of 2D Images

In this section, the 3D MR images of the breast phantom are registered to a sequence of 2D images acquired from different orientations of the compressed phantom using the the proposed method. In Section 4.3.1, the details on acquiring 3D MR images from the uncompressed and compressed phantom were given. Reference images in the registration are 15 2D slices which are computed from the 3D compressed phantom images. All planes of 2D images pass through the center point of the phantom image volume having different orientations. The normal vector to the plane of each 2D image is given as

$$\vec{n}_i = [0\ ;\ \cos(\frac{i\pi}{15})\ ;\ \sin(\frac{i\pi}{15})]; \quad i = 0, 1, ..., 14 \tag{6.6}$$

The grid for 2D images is 90×120 among which a regularly distributed 30×40 points are employed as control points. The pixel size for 2D images is 1×1 mm.

The same FE dynamic model as Section 4.3.1 is used in this section to construct the deformation model. In Figure 6.2, the cubic FE mesh which is used for registration is depicted before (Figure 6.2a) and after (Figure 6.2b) deformation with two 2D image planes across the mesh. The two 2D planes across the FE mesh are demonstrating two different 2D intraoperative MR planes (reference images) in Figure 6.2a, and the corresponding 2D image planes in the volume of deformed template images in Figure 6.2b. The mesh has 15112 elements with 3067 nodal points. The size of the reduced dynamic model is m = 1000 where only 10.8% of modes of the full deformation model is considered in the

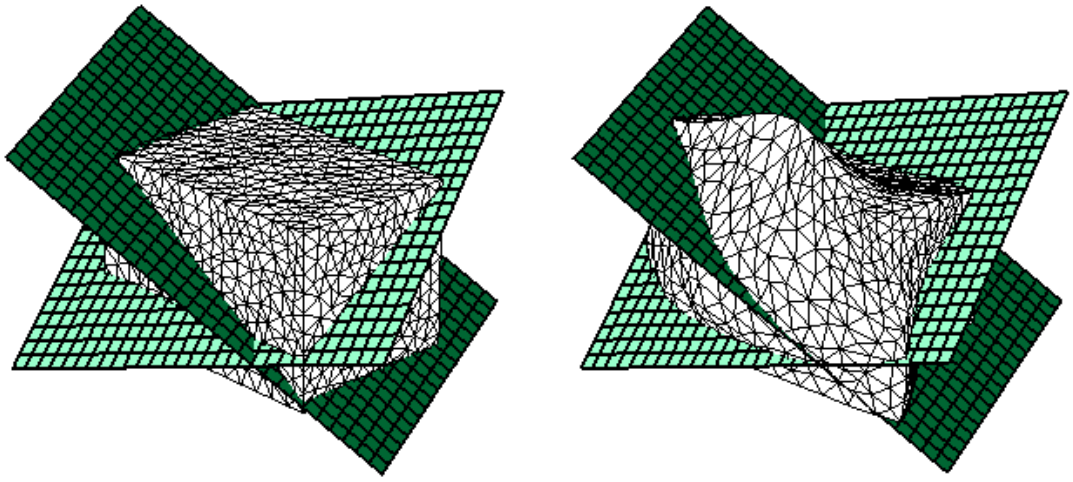

(a) Undeformed mesh (b) Deformed mesh

Figure 6.2: Undeformed and deformed FE mesh for phantom image registration.

dynamic model. Furthermore, the number of bins N is 256 in this experiment. p, q and s for the initial estimate error $\mathbf{P}_0$, process $\mathbf{Q}$ and measurement noise $\mathbf{S}$ covariances are considered 0.5, 100, and 0.01 respectively. A 3D Gaussian filter with a 8×8×8 kernel and $\sigma = 2$ is employed to smoothen the image in the computation of the gradient of the template image $\nabla T[\mathbf{u}]$.

In order to update the states of deformation based on 3D-2D registration method proposed in this chapter, the 2D images could be used either altogether after they all are acquired, or one by one as they are obtained by the imager. While the two approaches would yield similar results in the case of a static tissue deformation, the second method should be used if the tissue is dynamically deforming during the imaging process. In this experiment, 2D images are registered separately while the deformation model spatially correlates information of different 2D images. Figure 6.3 shows the evolution of three different similarity/distance measures between the reference and deformed template images as functions of iteration number. The volume of preoperative image is independently registered to the

Table 6.1: 3D-2D registration results in terms of TRE (in mm) using different similarity/distance measures. Coordinate frames are given in Figure 4.2a.

Registration using	SSD	CR	MI	Before
Mean±std in x	2.32±1.59	1.84±1.54	3.11±1.89	14.70±1.72
Mean±std in y	0.67±0.49	0.63±0.54	1.10±0.53	2.85±1.91
Mean±std in z	1.28±1.31	1.00±1.01	1.43±1.07	2.08±1.43
Mean±std	3.19±1.19	2.55±1.31	3.80±1.83	15.31±1.37
Median	3.2	2.44	3.30	15.82

sequence of 2D intraoperative images. The algorithm iterates 15 times for each image slice.

In Figure 6.3a, the change of similarity/distance measures between the 2D reference images and their corresponding 2D deformed template images are plotted as a function of iteration steps. The final state estimates from registering each image slice are used as initial conditions for the estimation using the next image slice. It takes 225 iterations to register all 15 image slices. It can be seen from Figure 6.3a that, during 15 iterations for each image slice, SSD between 2D images is decreasing while CR and MI are increasing. In Figure 6.3b, the similarity/distance measures between the 3D reference volume (from which the intraoperative 2D slices are interpolated) and the volume of deformed template images is plotted as a function of iteration steps. Using the sequence of 15 2D image slices, the deformation of the breast phantom is gradually estimated. Finally, the volume of the preoperative (template) images is warped based on the final estimated tissue deformation using the FE-based deformation model.

In Figure 6.4, the resulting images from SSD-based registration are shown. In this figure, three different views of the template volume (a), reference volume (from which the 2D images are computed) (b), deformed template volume (c) and the difference images (d) are given. The difference image is the intensity difference between the deformed template volume and the reference volume. The registration results based on TRE for eight pairs

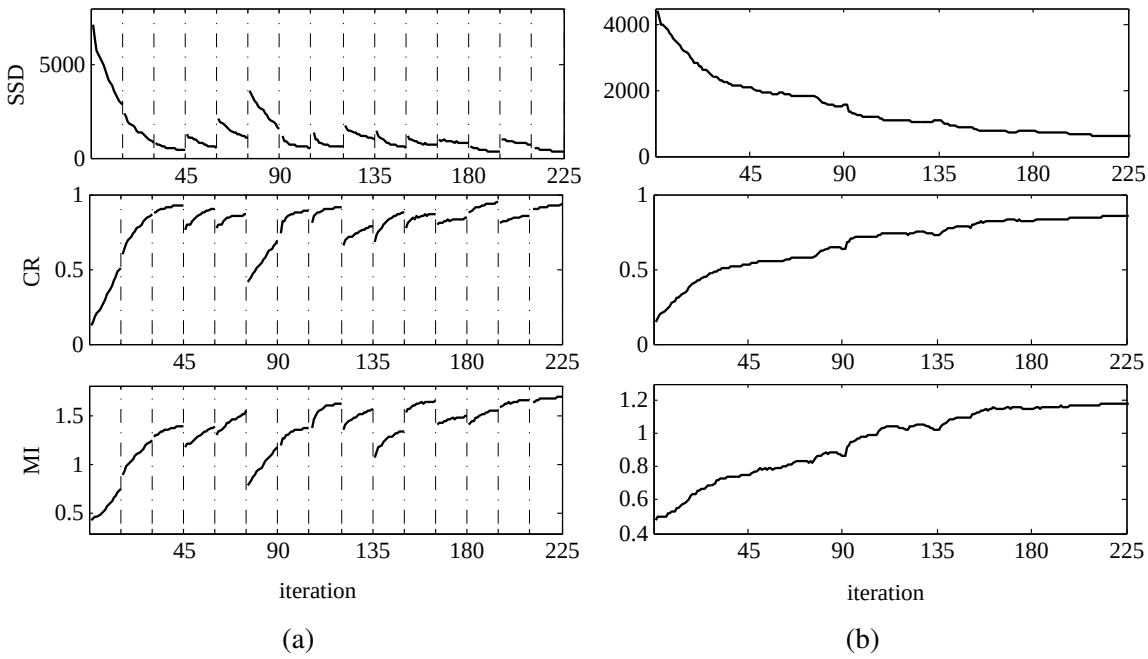

Figure 6.3: The evolution of similarity/distance measures in the iterative 3D-2D registration, (a) between 2D reference image and its corresponding 2D deformed template image, and (b) between the original 3D volume of reference images and the 3D deformed template images.

of manually identified fiducial points (see Section 5.2.1) are given in Table 6.1. In this table, the average (mean), standard deviation (std) and median of distances between fiducial points before and after the registration are given. The image axes are shown in Figure 4.2a. The average TRE is decreased from about 15.3 mm before registration to about 3.18 mm after registration. Similar to the registration results in previous chapters, CR-based registration outperforms SSD- and MI-based registrations. In this experiment, only the low information content of the pair of 2D slices are employed to compute the joint histogram at each iteration. This is one of the reasons for the relatively poor performance of the MI-based registration. TERs in 3D-2D registration is higher than those of 3D-3D registration results Chapters 4 and 5. However, these results are expected to improve when more 2D images from different cross-sections are employed.

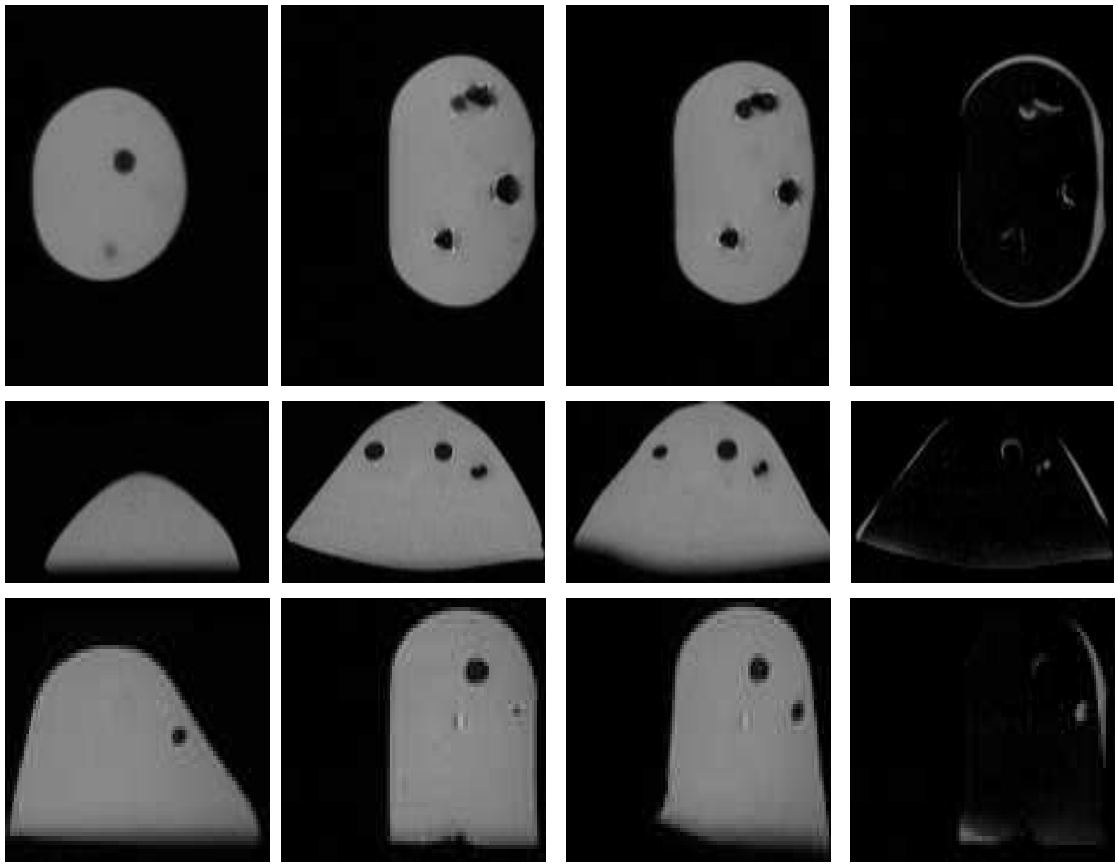

(a) (b) (c) (d)

Figure 6.4: Coronal (top row), axial (middle row) and sagittal (bottom row) views of the template (a), reference (b), registered deformed template (c) and the difference images (d) in 3D-2D SSD-based registration of the breast phantom images.

6.3.2 Registration of 3D MR Images of the Actual Breast to a Sequence of 2D Interventional Images

In this section, the 3D MR images of uncompressed breast (template/preoperative) are registered to a sequence of simulated 2D interventional MR images of compressed breast (reference/intraoperative). The breast MR images are identical to those of the Chapter 4 which were acquired under normal and compressed conditions (see Section 4.3.2 for more

details). Registration method explained in this chapter is applied to both right and left breast images separately and the experimental results on both image data sets are presented.

Interventional MR images are thicker and noisier than diagnostic MR images, and are degraded by the receiver coil inhomogeneity [15]. In this chapter, the actual 3D high-resolution MR images of the compressed breast are used to simulate the 2D interventional MR images. The voxel size for the high-resolution MR images is 0.7×0.7×1.1 mm. First, an isotropic MRI volume with voxel size of 1.4×1.4×1.4 mm is created from the original compressed breast image data using trilinear interpolation. Then, three thin 1.4 mm adjacent slices are averaged to form a thick 4.2 mm slice. Also, Gaussian noise is added to the thick averaged slices to reduce their SNR defined as

$$\text{SNR} = \frac{P_{\text{image}}}{P_{\text{noise}}} = \frac{P_{\text{image}}}{P_{\text{image-iMRI}}} \tag{6.7}$$

where P_{image} is the average power of the middle image slice and $P_{\text{image-iMRI}}$ is the average power of the difference between the middle thin slice and the simulated interventional MR image slice. With this definition, SNR for the average image is about 20 which becomes about 15 [15] after the addition of noise. Figure 6.5 shows a sample of the simulated interventional MR image, the average image slice as well as the middle thin slice.

The same FE mesh and the deformation model as Section 4.3.2 are employed in this experiment. The size of the employed reduced dynamic model is $m = 500$ which is equal to 3.96% of modes of the full deformation model. In this experiment, the 3D volume of uncompressed breast images are registered to nine 2D interventional MR images of the compressed breast. As shown in Figure 6.6, these 2D images are acquired from different positions and orientations, i.e., three slices in each of the axial, coronal and sagittal planes. The 2D interventional MR images are used all together in the iterative registration

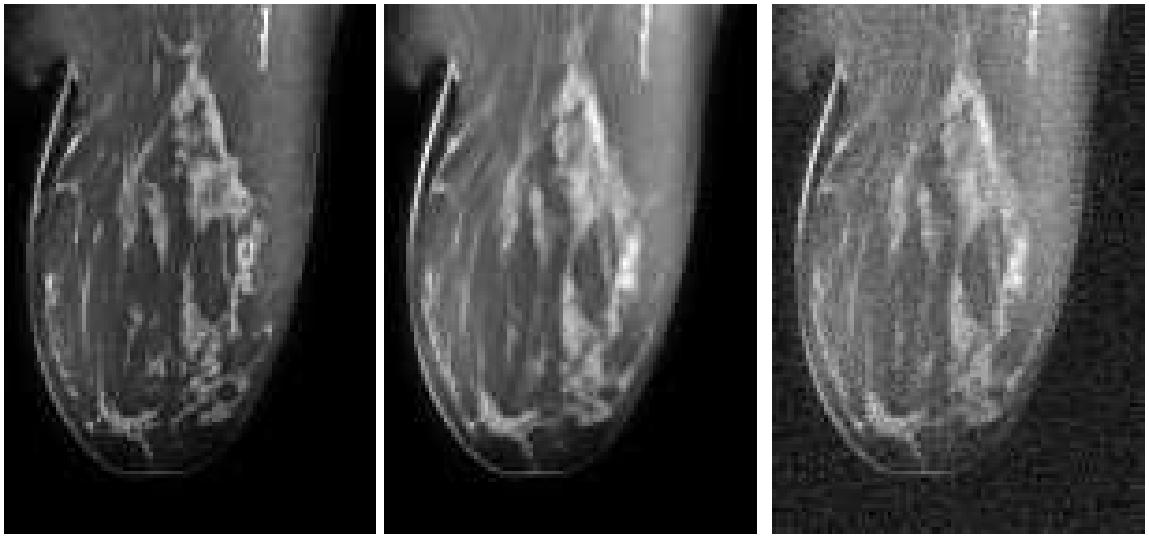

(a) (b) (c)

Figure 6.5: A thin image slice (a), the average image slice (b), and the simulated interventional MR image slice of the left breast (c).

algorithm after they have been acquired.

The resolution of the simulated interventional MR images is 100, 142 and 170 in the x (sagittal), y (coronal) and z (axial) direction respectively. Control points spacing is also considered to be 40, 50 and 60 in the direction of x, y and z, respectively. This means that, for instance, the observation prediction error vector is computed at a 40×50 grid points out of 100×142 image grid points in the axial (x-y) plane. It should also be emphasized that the observation prediction error $\mathbf{dx}_c$ in Equation (6.5), which is computed at any control point on the 2D interventional image planes, is a 3D vector and in general is not limited to the 2D plane of the interventional image. p, q and s for the initial estimate error $\mathbf{P}_0$, process $\mathbf{Q}$ and measurement noise $\mathbf{S}$ covariances are set to 0.1, 20, and 0.01 respectively. As was discussed in Section 4.3.1, a smoothing Gaussian kernel with a variable standard deviation σ is employed in the computation of the gradient of the template image $\nabla T[\mathbf{u}]$ to reduce noise and control the amount of details used in each iteration.

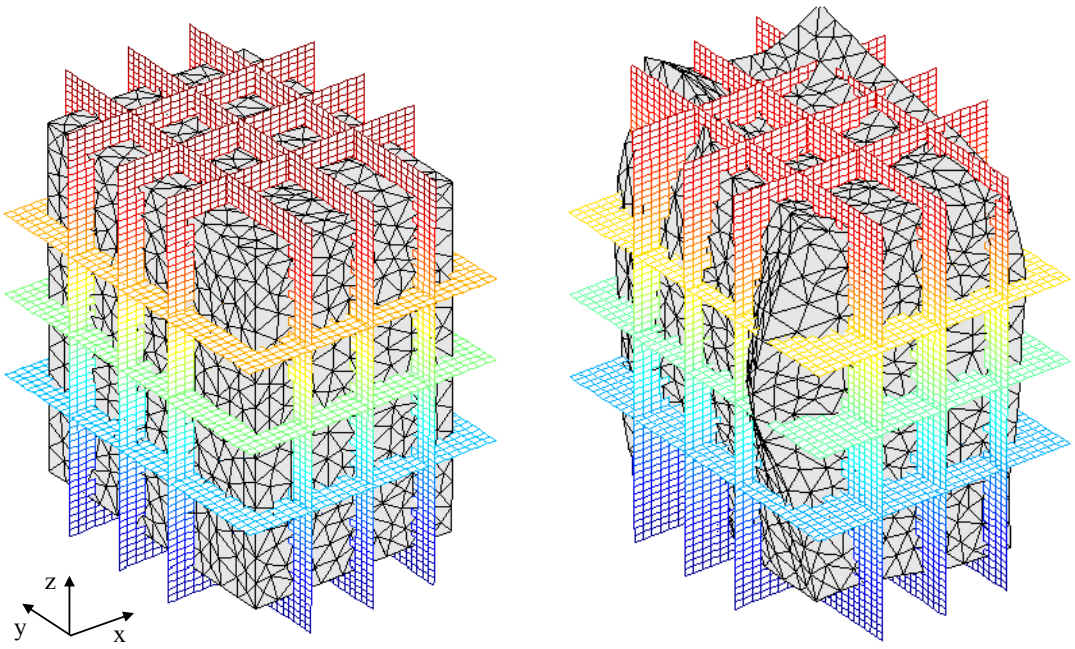

(a) Undeformed mesh (b) Deformed mesh

Figure 6.6: Deformed and undeformed FE meshes with nine simulated interventional MR image planes in 3D-2D registration of the breast images.

Table 6.2: 3D-2D sequence registration results for the *right* breast images in terms of TRE (in mm) using different similarity/distance measures. Coordinate frames are given in Figure 4.7.

Registration using	SSD	CR	NCC	MI	Before
Mean±std in x	1.45±1.71	1.07±1.38	1.16±1.44	1.10±1.45	8.65±4.52
Mean±std in y	0.84±0.73	0.85±0.67	0.75±0.51	1.74±1.76	1.83±1.79
Mean±std in z	0.75±0.57	0.68±0.56	0.71±0.62	0.86±0.64	5.50±3.70
Mean±std	2.10±1.63	1.76±1.35	1.76±1.39	2.53±2.02	11.29±4.01
Mean±std (IRTK)	—	2.74±2.02	2.81±1.95	2.65±1.63	11.29±4.01
Median	1.81	1.63	1.34	1.83	12.94

Table 6.2 and Table 6.3 summarize the registration results in terms of TRE for ten fiducial points for the right and left breast images, respectively. It is evident that NCC and CR-based registration outperform SSD and MI-based registrations. The average TRE is decreased from about 11.3 mm and 14.8 mm before registration to about 2.1 mm and 4.3 mm after registration in the right and left breast images, respectively. Comparing the

Table 6.3: 3D-2D sequence registration results for the *left* breast images in terms of TRE (in mm) using different similarity/distance measures. Coordinate frames are given in Figure 4.7.

Registration using	SSD	CR	NCC	MI	Before
Mean±std in x	0.91±0.90	1.24±1.39	1.17±1.38	1.71±1.66	10.05±5.60
Mean±std in y	1.33±1.32	1.74±1.17	1.53±1.30	1.96±1.50	2.25±2.01
Mean±std in z	2.48±2.86	3.03±2.83	2.95±2.54	4.16±3.35	8.91±6.19
Mean±std	3.44±2.70	4.14±2.76	4.04±2.40	5.54±3.00	14.78±6.11
Mean±std (IRTK)	—	6.33±3.37	6.44±3.02	5.92±3.07	14.78±6.11
Median	3.19	3.68	2.4	5.40	16.43

results of this section with the TREs given in Table 5.4 and Table 5.5, it can be concluded that 3D-2D sequence registration results in similar results as 3D-3D registration in the right breast images. But, in the left breast images that the compression is larger than the right breast images, the average TREs are about 1.3 mm larger than 3D-3D registration. However, the outcome is still acceptable considering that only 9 thick and noisy slices have been used for the registration of images with a large deformation. More interventional 2D slices are expected to reduce TREs.

The registration results in this section are also compared to those of the IRTK [182] (see Section 5.2.2 for more details). For this experiment, the IRTK algorithm is implemented at three resolution levels. The control points spacing is chosen as 40, 50 and 60 in x, y and z direction, respectively, which is identical to the resolution of the grid of control points used as the vector of observation prediction errors in the proposed method of this thesis. For IRTK implementation, simulated 2D interventional MRI slices are assembled in a 3D matrix. In the reference image volume, voxel points which are not on the interventional MRI slices are padded -1 and are ignored (masked) in the registration. Therefore, IRTK employs all slices together in the registration as a 3D volume.

The results given in Table 6.2 and Table 6.3 show that the average TREs of the state estimation-based registration method are better than those of IRTK in most cases. Average

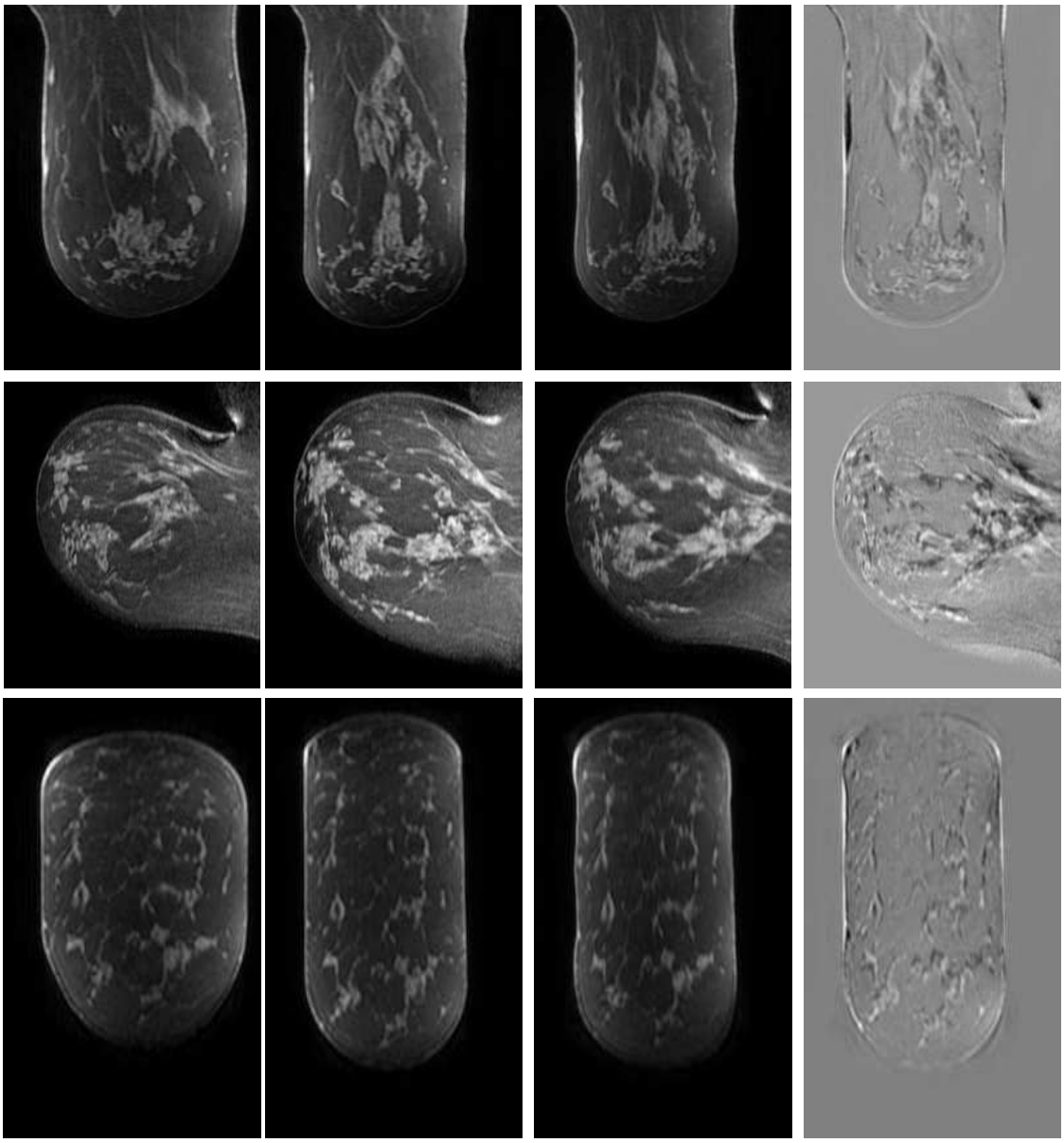

(a) (b) (c) (d)

Figure 6.7: Axial (top row), sagittal (middle row) and coronal (bottom) views of the template (a), reference (b), registered deformed template (c) and the difference images (d) in 3D-2D sequence NCC-based registration of the *left* breast images using the method of state estimation for dynamical systems.

TREs in state estimation-based registration method are 1 mm and 2 mm less than those in IRTK in the right and left breast images, respectively. Furthermore, IRTK in SSD-based

registration produces unrealistic deformations in both right and left breast images. Hence, the TRE of fiducial points have not been computed for these cases.

The resulting images for 3D-2D sequence NCC-based registration of the left breast images are given in Figure 6.7. In this figure, images of the normal breast (Figure 6.7c) are deformed to match the images of the compressed breast (Figure 6.7b). The deformed template images are shown in Figure 6.7c and the difference between the reference images and the deformed template images are given in Figure 6.7d. It is evident from this figure that the deformed template images are very similar to those of the actual compressed breast.

Chapter 7

Dynamic tracking of tissue deformation based on registering 3D preoperative images to real-time 2D intraoperative images

In this chapter, the proposed state estimation-based registration method is further developed to register 3D preoperative images to 2D intraoperative images of a dynamically deforming tissue. The states of tissue deformation are estimated over time using a sequence of real-time 2D images acquired from the deforming tissue. The developed registration method is evaluated in tracking a target inside the breast tissue similar to what is required in MRI-guided breast biopsy. Also, the dynamic deformation of the breast phantom is tracked based on 3D-2D MR-US image registration using the proposed method.

7.1 Background and Motivation

Recent developments in medical imaging and interventional tools have made image-guided minimally invasive therapy a reliable alternative to open surgery in medical practice. Modern CT and MRI systems can provide informative details of the human anatomical structures in the form of 3D high-resolution images. However, high operational cost and incompatibility with other equipment in the operating room render these imaging modalities less suitable for real-time applications and interventional procedures. Dedicated interventional MRI systems and non-magnetic equipment have been developed in recent years for minimally invasive surgeries [17, 186]. However, the long acquisition and processing times of these imaging systems prevents surgeons from having real-time high-resolution volumetric images during the intervention. Hence, in MRI-guided breast biopsy procedures, for instance, 3D images are acquired before inserting the biopsy needle for localization of the lesions. Other image sets are acquired to verify the needle position when the needle is already inside the breast and it usually takes a few minutes [17, 187].

With existing technologies, nearly real-time MR imaging is feasible in the form of either one or a few 2D slices from certain orientations, or low-resolution and low-contrast 3D images which do not require long processing time. Although real-time 2D images provide limited spatial information about the organ, over time acquisition of these images could be helpful in conjunction with preoperative image data in image-guide biopsies and interventions. 3D high-resolution preoperative images can be dynamically registered to the real-time intraoperative 2D images. Based on the registration of images, preoperative surgical plans can be updated intraoperatively using the real-time information about the position of the lesion and surgical tools. *a priori* US is another imaging technique which is widely used

in procedures such as image guided needle biopsy and ablation therapy due to its low cost, compatibility with other equipment, and fast acquisition time. Unfortunately, US imaging is handicapped by a confined field of view, poor image quality and low sensitivity and specificity in detecting relatively small regions (e.g., lesions or tumours). Co-registration of preoperative MR/CT images with intraoperative US images can take advantage of the strengths of each these imaging modalities and provide a more comprehensive picture of the tissue than what would be available using only one imaging modality.

The registration method proposed in Chapter 5 is employed here to register preoperative image volumes to real-time 2D intraoperative images of a dynamically deforming tissue. The states of tissue deformation are estimated over time based on real time 2D images providing a spatial and temporal correlation between images acquired from different orientations at different times. The proposed method is evaluated in two different experiments of 3D-2D MR-MR and MR-US image registration.

7.2 The Registration Method

The method for 3D-2D registration in this chapter is based on the same registration framework proposed in Chapter 6. However, intraoperative 2D images are acquired from a tissue undergoing dynamic deformation. Preoperative images are registered to the real-time intraoperative images over time to dynamically follow the tissue deformation and provide high-resolution 3D images during the operation. Similar to registration method discussed in Chapter 6, the grid of control points is defined on the plane of the intraoperative 2D image. The position and orientation of the intraoperative 2D image plane can change at any time depending on the interventional MR or US imaging system. Therefore, the observation model needs to be updated any time and the Kalman gain has to be computed with

other matrices at each iteration according to the time and measurement update equations given in Table 5.1.

The flowchart of the registration algorithm is given in Figure 7.1. At each iteration, the coordinates of the real-time 2D MR/US image are first registered to the coordinates of the preoperative image volume using a rigid transformation. This rigid registration is not image-based. The rigid transformation depends on the position and orientation of the image detectors in imaging systems with respect to the patient. In US imaging, for instance, the transformation can be obtained using an optical, mechanical or electromagnetic localizer connected to the US probe. Based on this transformation, the intraoperative (reference) image grid is projected to the domain of the preoperative image data. The image slice interpolated from the preoperative image volume at the projected grid is the best initial match for the intraoperative 2D image before deformable registration.

The registration steps at each iteration are as follows.

1. *Time Update/Prediction*: The *a priori* estimates of the states $\hat{\mathbf{x}}_k^-$ is computed based on the vector of state estimates from the previous step according to the time update equation, i.e., $\hat{\mathbf{x}}_k^- = \mathbf{A}\hat{\mathbf{x}}_{k-1}$. The predicted displacements for the nodal points of the FE mesh can be computed using $\mathbf{u}_k^- = \phi_m \hat{\mathbf{x}}_k^-$. The *a priori* estimate error covariance matrix $\mathbf{P}_k^-$ is also updated in this step using the equation given in Table 5.1. The update of $\mathbf{P}_k^-$ was not required in 3D-3D registration (Chapter 5) since the steady-state Kalman gain was computed before starting the iterative algorithm.

2. *Find Deformed Image Grids*: The deformation of the intraoperative 2D image grid is computed based on the deformation of the FE mesh using elements' interpolation function. Then, the deformed 2D image grid is projected to the coordinates of the preoperative image volume.

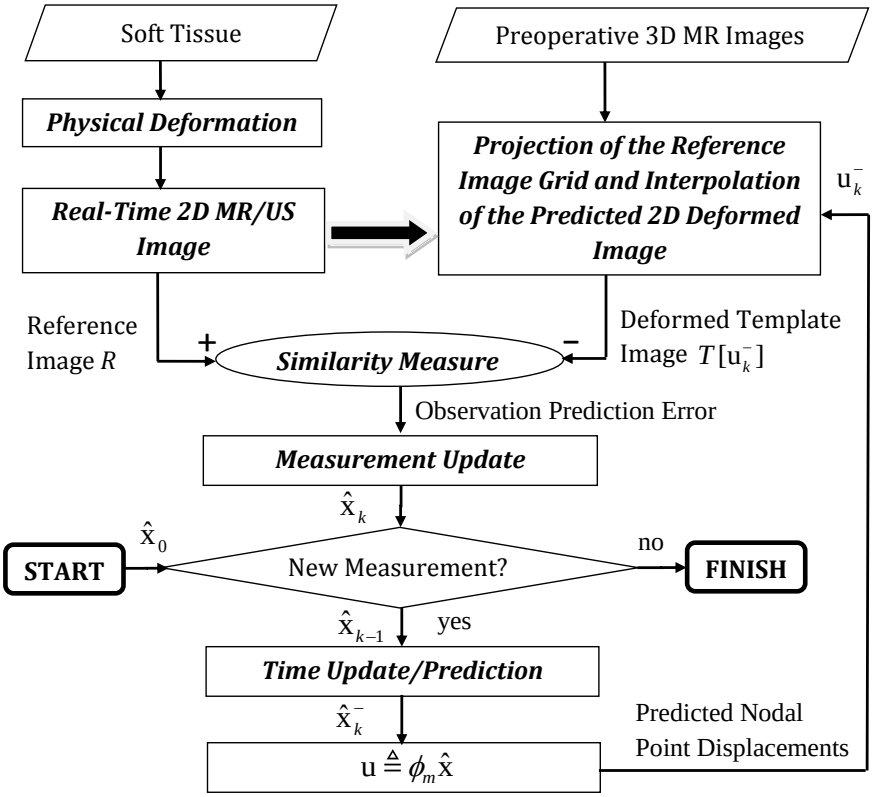

Figure 7.1: Block diagram of the iterative 3D-2D registration algorithm with dynamic tissue deformation based on the concept of dynamic state estimation.

3. *Interpolate the Predicted Deformed Template Image*: The predicted image grid in the previous step are used to compute the predicted deformed template 2D image $T[\mathbf{u}_k^-]$ from the preoperative image volume using the trilinear interpolation method.

4. *Compute the Observation Prediction Error*: Some of image grid points are considered as control points for computing the observation prediction errors. The observation prediction errors are computed at control points using Equation (5.10). As discussed in Section 6.2, for the similarity/distance measures given in Table 4.1, the displacement

computed at grid points (observation prediction error) is a 3×1 vector which is not restricted to the plane of the 2D intraoperative image. In MR-US registration another similarity/distance measure is employed in this thesis which is not given in Table 4.1. This metric which is based on MIND [98] will be explained later in this chapter.

5. *Measurement Update*: The state estimates are updated based on the vector of observation prediction errors using $\hat{\mathbf{x}}_k = \hat{\mathbf{x}}_k^- + \Gamma_k \mathbf{dx}_c$ where Γ_k is the update Kalman gain at iteration k. The Kalman gain Γ_k and the *a posteriori* estimate error covariance matrix $\mathbf{P}_k$ are updated using equations given in Table 5.1. The update of Γ_k and $\mathbf{P}_k$ were not required in 3D-3D registration presented in Chapter 5 when the steady-state Kalman gain was computed before starting the iterative algorithm.

Since the soft tissue is dynamically deforming over time, the iterative registration algorithm continues to follow the deformation as long as new measurements (images) are available. When the tissue reaches to an steady-state deformation point, the iterative algorithm is expected to stop similar to the criterion discussed in Section 6.2. However, since the simulations in this thesis are not real-time, a certain number of iterations is carried out for each 2D reference image. The whole volume of preoperative (template) images can be deformed at any time based on the estimated tissue deformation. For a desired resolution, the 3D image grid in the coordinates of the reference image is deformed based on the deformation of the FE mesh using elements interpolation function. The deformed grid is then transformed to the coordinates of the preoperative images. Finally, the volume of deformed template image is interpolated at deformed grid points from the preoperative images.

7.3 Similarity/Distance Measure for MR-US Registration

A different intensity-based similarity/distance measure is employed in this chapter for MR-US registration. For the single modality image registration experiments presented previously in this thesis, four similarity/distance measures, namely SSD, CR, NCC and MI were used. These metrics with a few other similarity/distance measures were discussed in Section 2.3.4. SSD is the simplest distance measure between images which works best for single-modality images. CR, NCC and MI have been employed in the literature for single and multi-modality image registration problems. However, these metrics do not perform as well in the registration of preoperative MR or CT images to intraoperative US images as they do in the registration of other modalities. US images have lower SNR than other diagnostic imaging modalities such as MRI, CT, PET and SPECT. US images suffer from a type of acoustic noise called speckles caused by the scattering of the US beam from microscopic tissue inhomogeneities [188]. Speckles in US images are the main source of image degradation. Furthermore, US images usually have artifacts and shadows which do not exist in other imaging modalities.

Various intensity-based similarity/distance measures were considered for MR-US registration among which MIND outperformed other metrics for the intended application of this thesis. MIND, which stands for modality independent neighbourhood descriptor, was proposed by Heinrich *et al.* [98] and originally was evaluated in the registration of 3D thoracic CT scans between inhale and exhale as well as the registration of 3D CT and MRI scans. MIND extracts distinctive structures in a local neighbourhood based on the similarity of small image patches within the image. The extraction of structures using this method is independent from image modalities, contrast, noise and intensity levels of the

images [98]. However, it is sensitive to different types of image features such as corner points, edges and textures. The method benefits from the concept of image self-similarity which first was introduced for non-local means filtering for image denoising [189]. In the proposed denoising method, structural similarities in an extended non-local region of an image feature are found. The denoised central voxel is determined based on a weighted average of values of similar patches in the non-local search window.

MIND is basically a multi-dimensional image descriptor which represents the distinctive image structures in a local neighbourhood [98]. MIND is extracted based on patch distances in each image separately (different modalities). Extracted descriptors are then compared using simple single-modality similarity/distance measures such as SSD. MIND can be formulated based on a distance D_p, a variance estimate Var and a spatial search region $\mathcal{R}$ at any point $\mathbf{y}$ of image Im as [98]

$$\text{MIND}(Im, \mathbf{y}, \mathbf{r}) = \frac{1}{n} \exp\left(-\frac{D_p(Im, \mathbf{y}, \mathbf{y}+\mathbf{r})}{\text{Var}(Im, \mathbf{y})}\right); \quad \mathbf{r} \in \mathcal{R} \tag{7.1}$$

where n is a normalization constant for having the maximum value equal to 1 and $\mathcal{R}$ is the search region. Therefore, using MIND, the image will be represented by a vector of size $|\mathcal{R}|$ at any pixel/voxel point. The distance between two pixels/voxels $\mathbf{y}_1$ and $\mathbf{y}_2$ of image Im is defined as the SSD of all pixels/voxels between two patches P of size $(2\mathbf{p}+1)^d$ (d is the image dimension) centered at $\mathbf{y}_1$ and $\mathbf{y}_2$ as

$$D_p(Im, \mathbf{y}_1, \mathbf{y}_2) = \sum_{\mathbf{p} \in P} (Im(\mathbf{y}_1 + \mathbf{p}) - Im(\mathbf{y}_2 + \mathbf{p}))^2 \tag{7.2}$$

Different methods are proposed in [98, 189] for computing Var among which the simplest way is to use the mean of the patch distances within a six-neighbourhood $\mathcal{N}$ in 3D images

(four-neighbourhood in 2D images) as

$$\mathrm{Var}(Im, \mathbf{y}) = \frac{1}{6} \sum_{\mathbf{i} \in \mathcal{N}} D_p(Im, \mathbf{y}, \mathbf{y} + \mathbf{i}). \tag{7.3}$$

Therefore, for any pixel/voxel point of the image, MIND can be calculated given two parameters, i.e., $\mathbf{r}$ and $\mathbf{p}$. Then, the similarity/distance measure between the reference image R and the deformed template image $T[\mathbf{u}]$ at point $\mathbf{x}_c$ can be defined as the SSD of MINDs calculated from two images at that point, i.e.,

$$I(R, T[\mathbf{u}], \mathbf{x}_c) = \frac{1}{|\mathcal{R}|} \sum_{\mathbf{r} \in \mathcal{R}} (\mathrm{MIND}(R, \mathbf{x}_c, \mathbf{r}) - \mathrm{MIND}(T[\mathbf{u}], \mathbf{x}_c, \mathbf{r}))^2 \tag{7.4}$$

Unlike similarity/distance measures in Table 4.1 which are defined for whole image volume, the measure in Equation (7.4) is defined locally at point $\mathbf{x}_c$. Therefore, the observation prediction error at each control point $\mathbf{x}_c$ can be computed using Equation (5.10) as

$$\mathbf{dx}_c = \mathbf{z}_k - \mathbf{H}\hat{\mathbf{x}}_k^- = -\frac{1}{\gamma} \nabla I(R, T[\mathbf{u}_k^-], \mathbf{x}_c) \tag{7.5}$$

In 3D-2D registration, the reference image R and the deformed template image $T[\mathbf{u}]$ (projected reference image in the coordinates of the template image) are both 2D. A numerical method is employed to compute the derivative of the similarity/distance measure defined based on MIND, i.e., $\nabla I(R, T[\mathbf{u}_k^-], \mathbf{x}_c)$. The computed derivative at each control point is a 2×1 vector on the plane of the reference (US) image. This vector represents a 3D displacement vector when projected to the coordinates of the template image. Although the measured observation prediction error at each iteration is on the plane of the reference

(US) image at each iteration, the final computed deformation is not limited to this plane because the whole volume the FE mesh is deformed at each iteration based on the estimated deformation states using the 3D model.

7.4 Experiments and Results

7.4.1 Dynamic Target Tracking in Image-Guided Breast Biopsy based on 3D-2D MR-MR Registration

In this experiment, a moving/deforming sub-volume inside the breast tissue is tracked using 2D intraoperative MR images while the tissue deforms due to the biopsy needle insertion forces. The application of interest is real-time MR image-guided breast biopsy. A sequence of interventional 2D MR images in the direction of needle insertion is employed over time to estimate deformation states based on the model presented in Section 5.1.1. The tissue is dynamically deforming as the intraoperative 2D images are acquired. To produce the intraoperative images, tissue deformation during the needle insertion is simulated using a commercial software. The deformation of the breast tissue is recorded and used with the pre-insertion image data to simulate a sequence of 2D images taken in the plane of the needle at consecutive sample times during insertion. MR image artifacts due to the presence of the needle are also simulated. Details concerning the actual breast MR images used in this experiment were given in Section 4.3.2.

The partial differential equations (PDE) solver FlexPDE 6 [190] simulates the tissue deformation. First, a FE mesh is created that encompasses the entire uncompressed breast image data, see Figure 7.2a. Loads are applied to the boundaries (y-z plane) of the mesh until they reach the borders of the compressed breast image data (Figure 7.2b). During

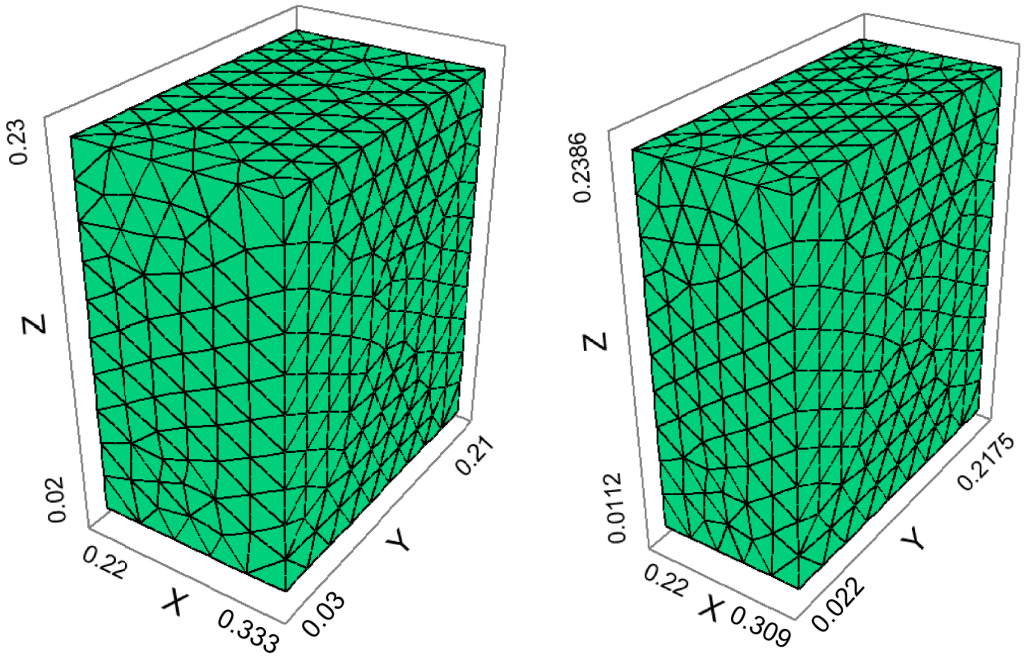

(a) (b)

Figure 7.2: FlexPDE FE mesh for the simulation of needle insertion: uncompressed (a) and compressed mesh (b) after application of boundary forces. Dimensions are in meters (m).

the biopsy, the breast tissue is immobilized using parallel compression plates [12]. Finally, needle forces are applied to the compressed mesh to simulate the effect of needle entering the tissue in the x (sagittal) direction from right to left in Figure 7.3. Two types of forces are considered: friction forces distributed along the portion of the needle inside the soft tissue, and cutting forces concentrated around the tip of the needle. A Gaussian profile is created for the needle forces along the needle path, as shown in Figure 7.3a. At each point the needle force is computed using

$$\mathbf{f}_n = \mathbf{f}_f + \mathbf{f}_c = \mathbf{f}_{fmax} e^{-d_f^2/2\sigma_f^2} + \mathbf{f}_{cmax} e^{-d_c^2/2\sigma_c^2} \tag{7.6}$$

where $\mathbf{f}_n$ is the amplitude of the total needle force which is the sum of friction $\mathbf{f}_f$ and

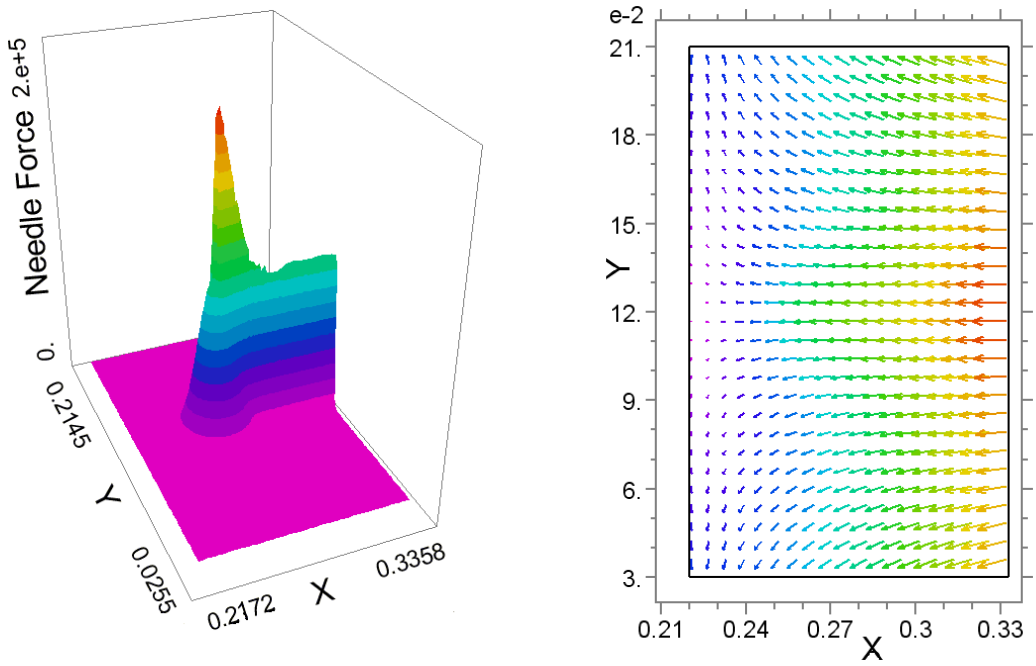

(a) (b)

Figure 7.3: Needle insertion simulation: force profile (a) and displacement field in the axial plane (b). Dimensions are in meters (m).

cutting $\mathbf{f}_c$ forces. This force is applied in the direction of insertion along the needle length. Furthermore, d_f is the distance from the needle, d_c is the distance from the needle tip, and $\mathbf{f}_{fmax}$, $\mathbf{f}_{cmax}$, σ_f and σ_c are real and constant positive numbers. Figure 7.3b also shows the deformation field in the axial plane after inserting the needle in the compressed FE mesh.

It should be noted that the FlexPDE simulation employs a large-deformation nonlinear model [191] whereas the registration is based on a linear elastic deformation model. Moreover, the FE meshes employed in the FlexPDE simulation and the registration process are completely different. The simulated deformation of the mesh (nonlinear model) during the needle insertion is recorded and used to produce intraoperative images of the breast. The model of the breast is compressed in the first four seconds of the simulation and then the

needle is inserted into the tissue over next six seconds with a speed of 7.33 mm/sec. 2D interventional MR images are simulated at a fixed orientation parallel to the needle insertion path. The interventional MR images are created by averaging three adjacent slices and adding Gaussian noise as discussed in Section 6.3.2. The susceptibility artifact of the needle inside the breast tissue is also considered when generating the images. The artifact depends on factors such as the diameter of the needle and its composition, magnetic field strength and the direction of the insertion [186, 192]. The size of the needle artifact has been reported in [186] to be 9.5 mm for a 14-gauge sterile biopsy needle surrounded by a 13-gauge needle holder used in a 3 T MRI-guided large-core-needle biopsy. In this experiment, an artifact of 10 mm in diameter is considered around the needle. Figure 7.4 shows four simulated interventional MR images as the needle progresses inside the breast tissue; the square marks a target sub-volume which is located to the left of the final needle tip position. The size of the target sub-volume is 21.1×21.1×33.0 mm.

The actual 3D pre-insertion images of the compressed breast are registered to the simulated 2D interventional MR images at each acquisition sample time in order to track a target sub-volume inside the breast tissue, e.g., the location of a hypothetical tumour. Interventional MRI acquisition time has been reported to be around 1.2 sec for a 256×256 image in [193] and approximately 1 sec and less in [194]. More recently, Roujol *et al.* [195] used a frame rate of 10 images/sec in real-time MR-thermometry and dosimetry for interventional guidance on the liver and the kidney. In this experiment, for the 6-sec period of needle insertion time, the deformation of FlexPDE mesh is recorded with a sampling period of $t_s = 1$ sec, resulting in seven 100×142, 4.2 mm thick interventional MR images with the pixel size of 1.4×1.4 mm. A regular grid of 40×60 out of the 100×142 interventional MR image grid points is considered as control points for the calculation of the observation

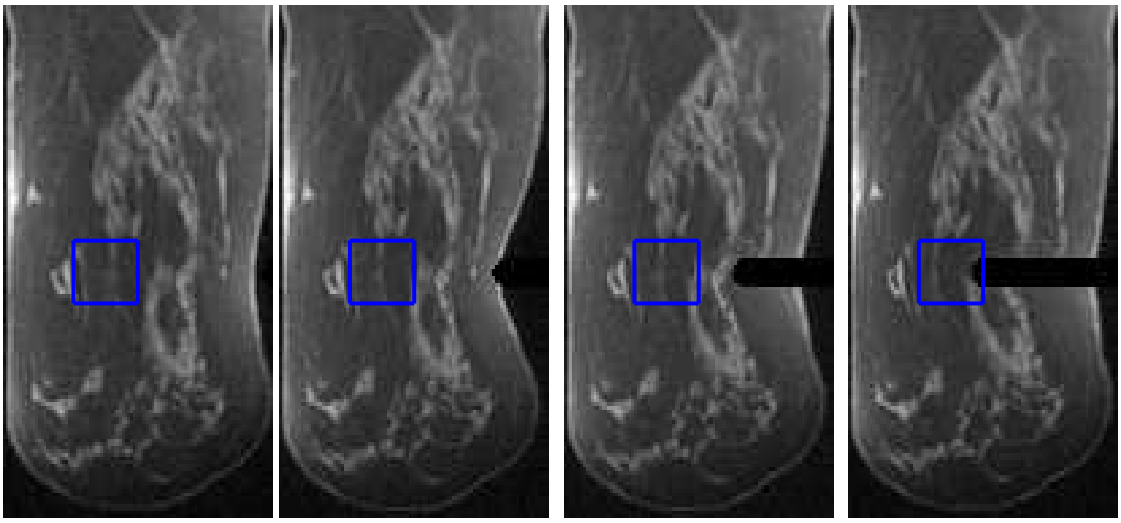

(a) (b) (c) (d)

Figure 7.4: Simulated interventional MR images with the susceptibility artifact during the needle insertion at acquisition times equal to 1 (a), 2 (b), 4 (c) and 6 (d) seconds, with the square showing the target region inside the left breast images. Coordinate frames are given in Figure 4.7.

prediction error $\mathbf{dx}_c$. The region of the needle artifact is predicted and excluded from the measurements. In information theoretic metrics-based registration, i.e., MI, NCC and CR, the corresponding 100×142 image from the template data is interpolated in each iteration to form the joint intensity histogram ignoring pixels in the needle artifact region.

A cubic FE mesh with 22717 tetrahedral elements and 4502 nodal points encompassing the entire volume of the compressed breast is generated using the COMSOL Multiphysics and Simulation software [178]. In the reduced dynamic deformation model $m = 500$. Using this mesh, the deformation model is constructed as discussed in Chapters 3, and 5. Figure 7.5 shows the FE mesh before (Figure 7.5a) and after registration (Figure 7.5b). The deformation caused by needle forces is evident in Figure 7.5b which is the inverse of the actual physical deformation of the breast tissue.

For the registration in this experiment, p, q and s for the initial estimate error $\mathbf{P}_0$, process

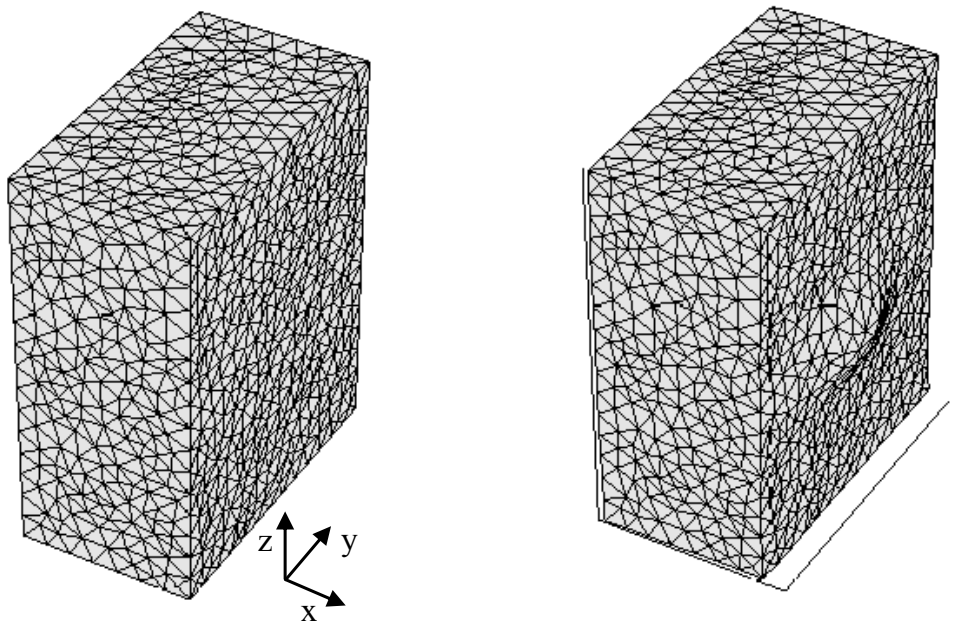

(a) Undeformed mesh (b) Deformed mesh

Figure 7.5: Deformed and undeformed FE meshes in the dynamic target tracking for image-guided breast biopsy.

Q and measurement noise **S** covariances are set to 0.02, 10, and 0.002, respectively. Similar to Section 4.3.1, a smoothing Gaussian kernel with a variable standard deviation σ is also employed in the computation of the gradient of the template image $\nabla T[\mathbf{u}]$ to reduce noise and control the amount of details used in each iteration. Figure 7.6 shows axial, sagittal and coronal views of the target sub-volume in the simulated (reference) and NCC-based registered images at the seven acquisition sample times during needle insertion. In this figure in any view, the left column (registered images) tracks the right column (reference images). The first row shows the target sub-volume in the compressed breast image data before needle insertion and the remaining seven rows display the target sub-volume in the reference (simulated) and registered image volumes. Since the reference image is in the axial plane, target tracking in this plane is better than the other two planes.

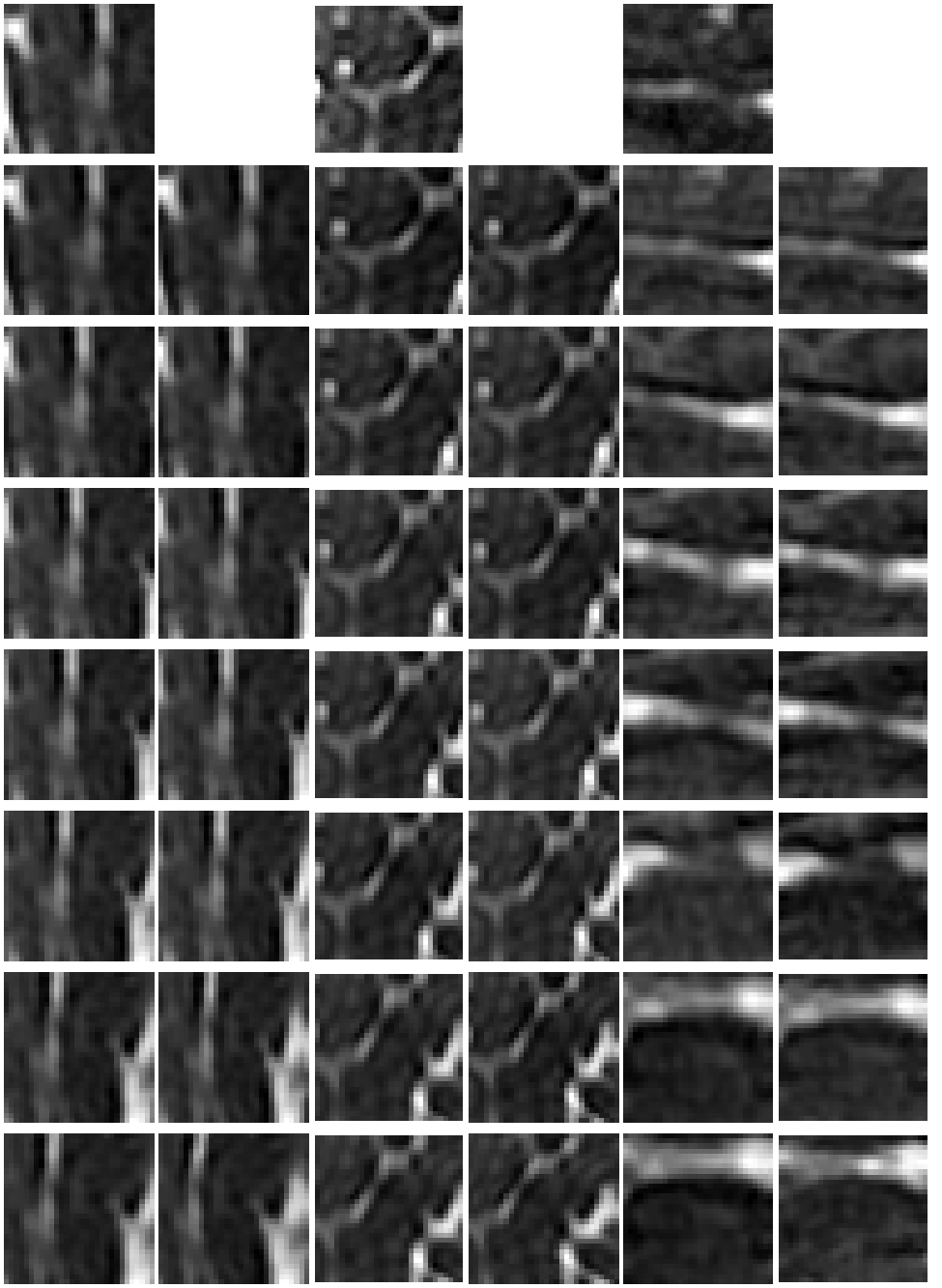

Figure 7.6: 3D view of the target sub-volume in the simulated and registered image data. For each view the right column shows the simulated images (reference image) and the left column shows the registered images (deformed template image). Seven rows (from top to bottom) are for $t = 4, 5, ..., 10$ sec during the insertion period. Coordinate frames are given in Figure 4.7.

Although only one axial image slice is employed as the reference image in the registration, the exact position of the voxel points of the target sub-volume in both simulated (reference) and registered (deformed template) images are known. Therefore, to evaluate the performance of the registration, rather than manually identifying fiducial points and computing TRE, the Euclidean distance between all voxel points of the target sub-volume in two images is computed as a measure of registration (tracking) error. Figure 7.7a depicts the average and standard deviation of the voxel point distances at each sample time using different similarity/distance measures. In this figure, the line with a circle on it shows the average and standard deviation of the total deformation of the voxel points at each sample time. As the needle goes through the breast, the target sub-volume moves and deforms further. When the needle reaches the target, the average displacement of the target is about 8 mm. However, with dynamic 3D-2D image registration the deformation of the target sub-volume is tracked and the average tracking error is about 1.5 mm. The results in Figures 7.6 and 7.7 demonstrate how the registration method allows for tracking of a target lesion inside the breast using real-time 2D intraoperative images of the breast tissue during a biopsy procedure.

The average and standard deviation of the voxel point distances of the target sub-volume are also analyzed in x, y, z axis separately in Figures 7.7b, 7.7c and 7.7d respectively. The maximum deformation occurs in the x (sagittal) direction which is the direction of for needle insertion, see Figure 7.7b. The reduction in the tracking error in this direction is also more than other two directions. As can be seen from Figure 7.7c, the registration method based on all similarity/distance measures compensates the target sub-volume deformation in y (coronal) direction as well. However, the tracking error in z (axial) direction after the registration is more than the actual deformation in this direction (especially the variance

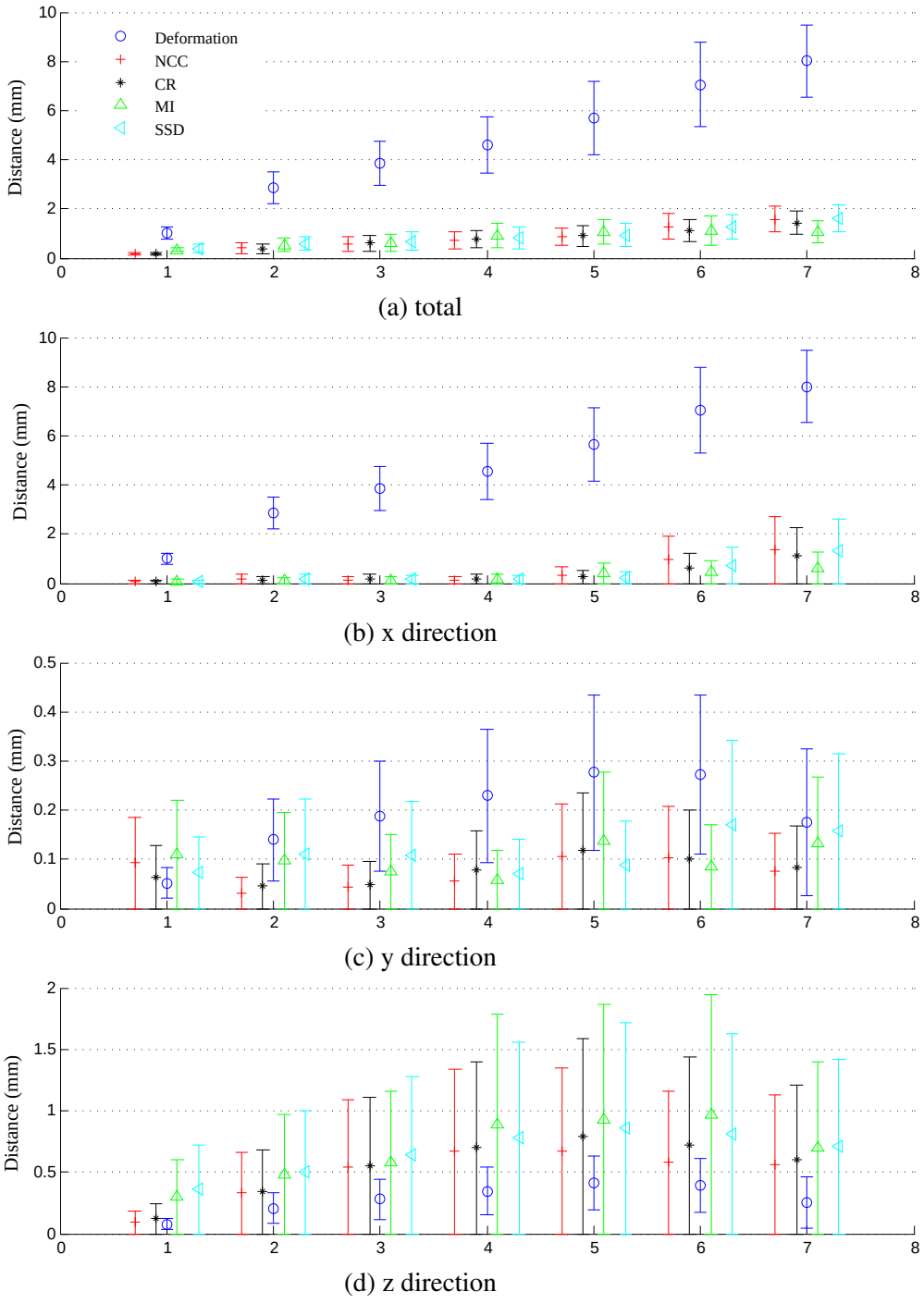

Figure 7.7: Averages and standard deviations of the voxel point distances (registration error) of the target sub-volume. Horizontal axes show seven sample times during the insertion period, i.e., $t = 4, 5, ..., 10$ sec.

of the error). Since the reference image is in the axial plane, there is not enough image information in the z (axial) direction for the registration. However, this error is less than half of the interventional image thickness, which is 4.2 mm.

As the needle penetrates through the tissue, the quality of the registration in the target sub-volume degrades. This effect can be primarily attributed to the needle artifact which approaches to the target sub-volume, resulting in information loss around this critical area. Comparing different similarity/distance measures, CR and NCC-based registrations outperforms MI and SSD-based registrations for small deformations (iterations 1-5). When the needle reaches the target, MI-based registration results in the smallest registration error.

7.4.2 Dynamic Tracking of a Deformable Tissue Based on 3D-2D MR-US Image Registration

In this section, 3D MR volume of a realistic breast phantom (CIRS model 051 [177]) is registered to its real-time 2D US images to dynamically track the deformation caused by pushing a linear US probe against the phantom. The phantom is mounted on an apparatus made of plexiglass shown in Figure 7.8. Eight fiducial markers which are visible in the MRI scan were employed for the registration of the MRI and optical tracker coordinate frames. A 3D image volume of 512×512×108 with voxel size of 0.47×0.47×1 mm was acquired from the phantom tissue using a GE Discovery MR750 3.0T machine. The MRI volume was rigidly registered to the real-time 2D US images using a system by Hologic Inc. [196] which integrates SonixTOUCH ultrasound [39] with Aegis Navigation (see Figure 7.9). In this system, the US transducer is tracked by an optical tracker allowing for examination of the same anatomical features under both US and MRI modalities. The accuracy of this registration quickly degrades when the tissue is deformed due to the force of the ultrasound

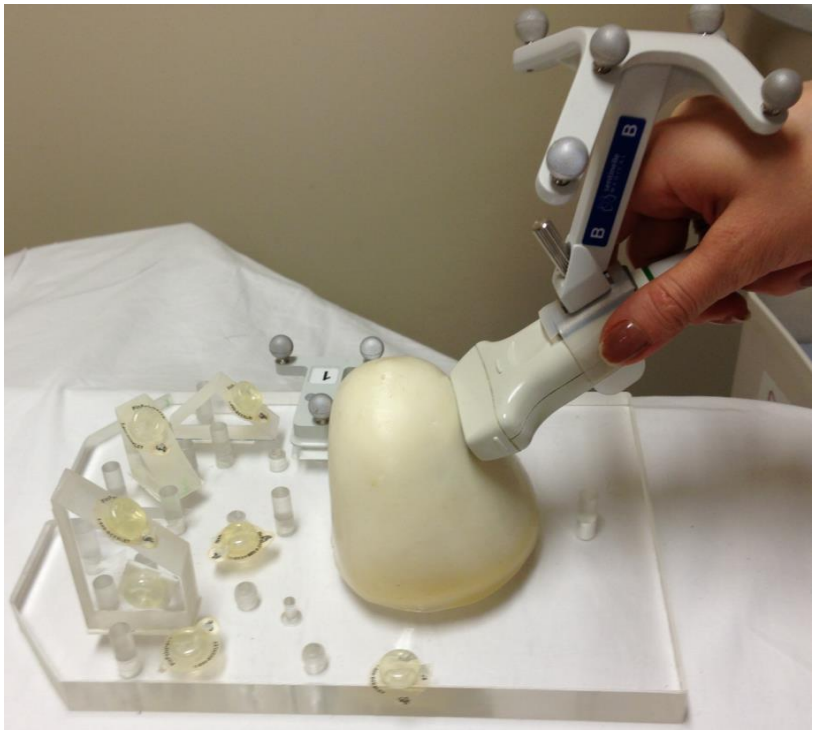

Figure 7.8: The breast phantom on the apparatus with fidicial markers and the US probe

probe. This is evident, for instance in Figure 7.9b, where the green horizontal line on the MR image that represents the transducer surface is well inside the phantom tissue boundary.

In these experiments, a linear US transducer is pushed and moved against the phantom in different scenarios to capture different features inside the phantom. In each experiment, the US images are recorded at the rate of 13 fps as well as synchronized navigation system data. Therefore, the 2D US image at any time can be projected to the coordinates of the MRI volume using the transformation given by the navigation system and the corresponding MR slice can be interpolated from the volume of MR images. A cubic FE mesh with 16732 tetrahedral elements and 3366 nodal points which encompasses the entire volume of

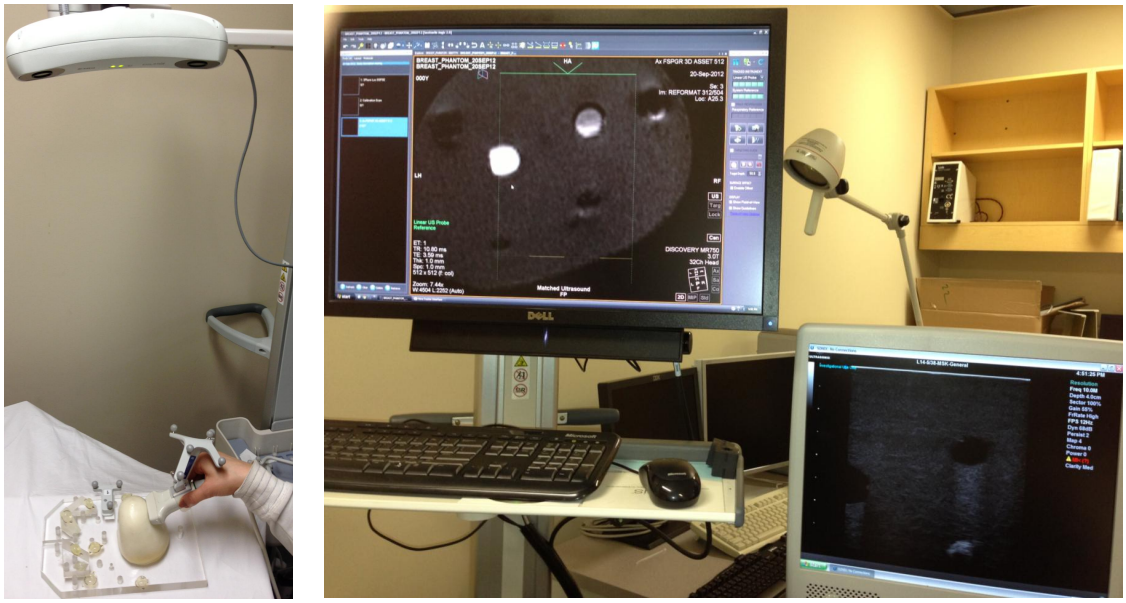

(a) (b)

Figure 7.9: Experimental setup: (a) a breast phantom and the tracking system, (b) real-time US and corresponding MR images out of the Aegis navigation system.

the breast phantom was generated using the COMSOL Multiphysics and Simulation software [178]. Using this mesh, an isotropic linear elastic model of deformation was created with the Young's elasticity modulus $E = 3$ kPa, the Poisson's ratio $\nu = 0.49$ and a mass density of $\rho = 0.95$ g/cm^3. In the reduced dynamic deformation model $m = 500$. Details concerning the deformation model based on FEM discretization were presented in Chapters 3 and 5.

The US image grid was extended with 0 (black) grayscale values in the direction normal to the transducer face. This extension allows the edges of the phantom to be considered in the MR images, providing extra features and facilitating the registration process. The extended US image grid (reference image) is 92×76 from which 23×19 points are used as control points for computing the observation prediction error. Before starting the iterative deformable registration, the first US frame was rigidly registered to the volume of MR

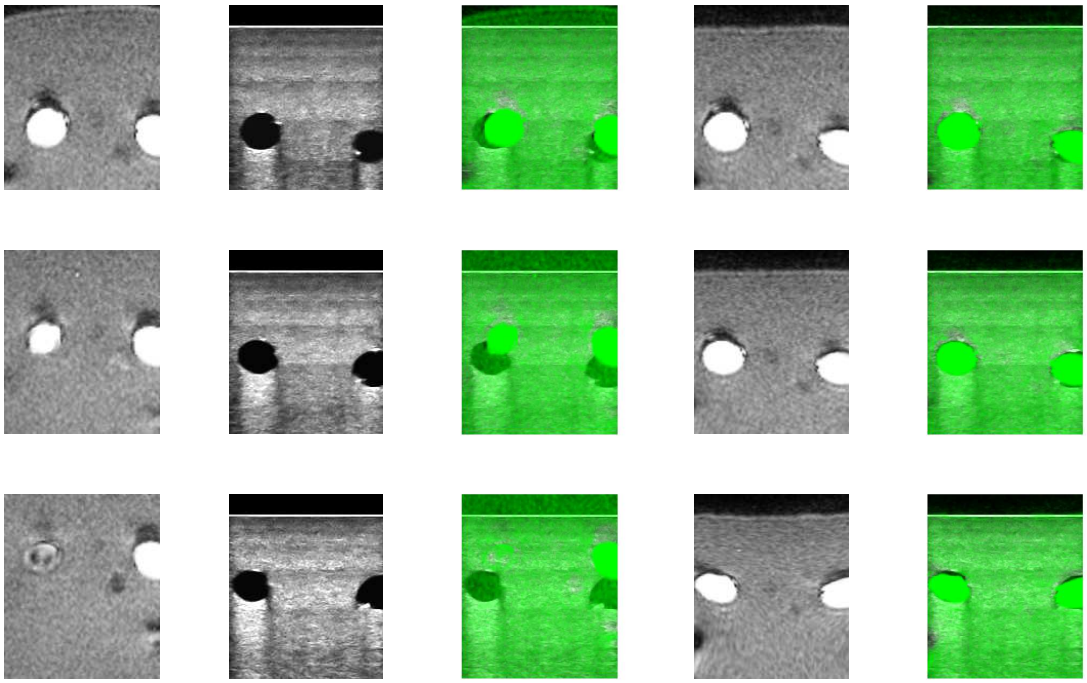

(a) (b) (c) (d) (e)

Figure 7.10: 3D-2D MR-UD registration results for three sample times: (a) MR image out of Aegis (registration based on the localizer) (b) US image, (c) US image laid over the MR image out of Aegis, (d) registered MR image, and (e) US image laid over registered MR image. Images are 45×38 mm. Top, middle and bottom rows are images for the results of the first, 11th and 21st slice registration, respectively.

images using the MIND-based similarity/distance metric defined in Equation 7.4. This reduces the number of iterations in the deformable registration algorithm for convergence to a solution. Both MRI and US images are filtered before registration using a Wiener filter to decrease image noise. Moreover, in this experiment, p, q and s for the initial states estimation error $\mathbf{P}_0$, process $\mathbf{Q}$ and measurement noise $\mathbf{S}$ covariances are set to 0.02, 100, and 0.1, respectively.

As is shown in Figure 7.10, the deformable registration aligns the preoperative MR and real-time US images and compensates the deformation and movement caused by the force of the US probe. The top row of the figure shows the first recorded slice where the probe is

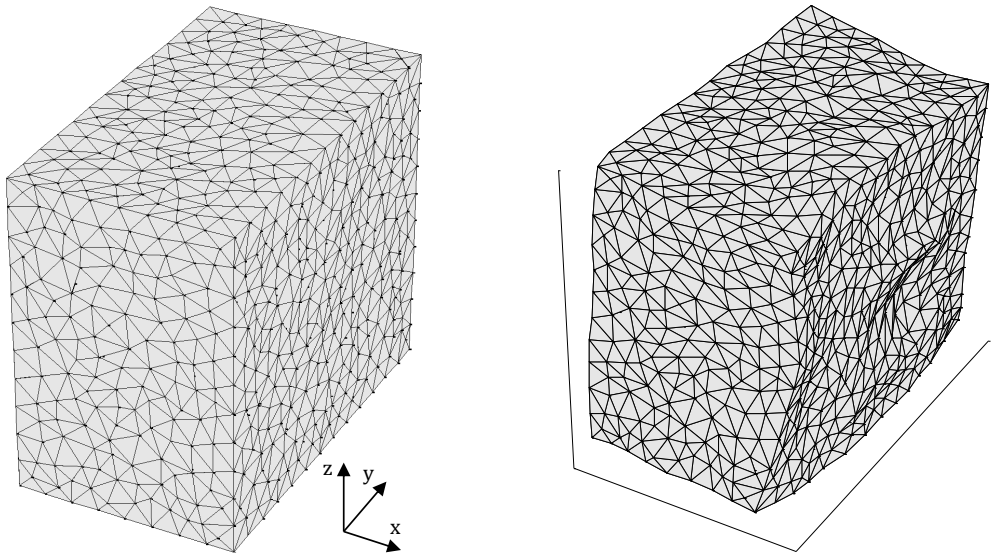

(a) Undeformed mesh (b) Deformed mesh

Figure 7.11: Deformed and undeformed FE meshes in the dynamic 3D-2D MR-US registration.

slightly pushed against the phantom whereas in the second and third rows the deformation increases. Although the US frame rate is 13 fps, only one from every five frames is recorded and employed for the registration, yielding an effective frame rate of 13/5 fps. Images shown in the second and third rows are after using 11 and 21 frames respectively, for updating the estimates of the deformation states. The average target registration error on the plane of 2D image for selected points on the edge (three points) and lesions inside the phantom (two points) depends on the size of deformation and was between 0.3 and 1.5 mm. As can be seen in Figure 7.10, both US and MR images are noisy with shadows and inhomogeneities. Furthermore, the internal structures of the phantom have different intensity levels for US (dark) and MR (bright), but the algorithm using the MIND-based similarity/distance metric could easily register these images.

The undeformed and deformed FE mesh employed in the registration are shown in

Figure 7.11. The whole area of the US image plane, i.e., the tissue and extended black area, is laid inside the FE mesh. The deformation happens in the phantom tissue, not in the extended black area. Therefore, most of the captured deformation in the FE mesh occurs actually inside the mesh and is not visible from the surface of the mesh in Figure 7.11b.

Chapter 8

Discussions

In this chapter a few important aspects of the proposed registration algorithms and their implementation including control points spacing, observability of the deformation model and their computations are discussed.

8.1 Control Points and Image Grids

Control points spacing has an important role in both the optimization-based (Chapter 4) and state estimation-based (Chapter 5–7) registrations methods. In order to estimate highly local non-rigid deformations of the tissue, a small spacing of control points is necessary. In the optimization-based registration method, nodal point forces are computed based on the gradient of the similarity/distance measure at the control points. A higher resolution grid of control points would provide a better estimate of image-derived forces which are computed using Equation (4.6). In the state estimation-based registration methods, the image measurement vector is computed at control points. With smaller spacing between control points, local information about tissue deformation can be incorporated in the estimation of the deformation states, which would potentially improve the registration outcome.

The resolution of the control points grid, however, has a direct effect on the number of computations. In all proposed registration methods in this thesis, the deformation of the control points are computed at each iteration based on the displacements of the nodal points of the FE mesh. In the optimization-based registration, the resolution of control points determines the number of rows of matrix Λ in Equation (4.5), which is used for the computation of nodal point forces in (4.6). In the state estimation-based registration methods, control points determine the size of the measurement vector, i.e., number of rows in the output matrix $\mathbf{H}$. This directly affects the computations involved in calculating the Kalman gain Γ, the *a posteriori* estimate error covariance matrix $\mathbf{P}_k$, and updating of the states based on the measurement vector.

The resolution of the reference R and template T images in the proposed registration algorithms is important in capturing fine scale information and local deformations. The reference and deformed template images are compared at each iteration based on the employed similarity/distance measure. High-resolution images would provide more information content in CR, NCC and MI-based registration methods to form the joint histogram between images and consequently compute a good approximate of the displacements of the control points. At the same time, high-resolution images impose high computational load in finding the deformation of the image grid, image interpolation, and calculation of the joint histogram between images at each iteration.

A good trade-off between the control points and/or image grids resolutions and computational load needs to be achieved empirically depending on the application requirements in terms of desired registration accuracy and available computation time and resources. Moreover, the voxel/pixel sizes of the original pre and intraoperative images need to be

considered in the control points spacing along different axes as well as interpolating low-resolution reference and template images in the registration algorithms.

A hierarchical multi-level approach can be employed in the estimation of non-rigid deformation of the tissue, resulting in an effective compromise between measured image information and the associated computations. In this paradigm, the iterative registration algorithm starts with low resolution reference and template images and large control points spacing. Image and control points resolutions increase in a coarse to fine fashion as the registration algorithm progresses. In such case, the steady-state Kalman gain in 3D-3D registration have to be computed offline for different levels of control points spacing. It should be noted that control points can be distributed unevenly over the domain of the reference image and they do not have to be on a regular grid.

8.2 Computations

The proposed registration methods in this thesis involve different tasks depending on the application of interest. These tasks can be categorized in three groups: tasks before starting the iterative registration algorithm, tasks during iterations, and those after iterations. Main computational tasks before starting the iterative registration algorithm are listed below with their computation times based on a MATLAB implementation on a 3.5 GHz Intel(R) Core(TM) i7-3970X processor with 64.0 GB RAM. The reported times here are for constructing the deformation model using a mesh with 21151 elements and 4206 nodal points, which is identical to the mesh employed for the registration of breast tissue images.

a) Constructing the stiffness matrix $\mathbf{K}$ and the mass matrix $\mathbf{M}$ based on the 3D cubic FE mesh. Computation time: 6 sec.

b) Computing ϕ based on the eigenvectors of $\mathbf{M}^{-1}\mathbf{K}$ and computing decoupled mass $\tilde{\mathbf{M}} = \phi^t\mathbf{M}\phi$, stiffness $\tilde{\mathbf{K}} = \phi^t\mathbf{K}\phi$ and damping $\tilde{\mathbf{C}} = \alpha\tilde{\mathbf{M}} + \beta\tilde{\mathbf{K}}$ matrices. Computation time: 5 min.

c) Computing the gradient of the template image T using a 3D Gaussian filter with different standard deviations σ. Computation time for an image of 512×512×240 with σ = 0.5, 1, 2 and 5: 7 sec, 18 sec, 64 sec and 4 min, respectively.

d) Search algorithm for finding the elements in which the output high-resolution image grid points are located. Computation time for an image grid of size 198×283×216: 34 min.

Above mentioned computations are common in all 3D-3D and 3D-2D registration methods. In 3D-3D registration problems, the following two tasks are also carried out before starting the iterations.

1. Search algorithm for finding the elements in which control and image grid points are located. Computation time for a grid of 30×40×40 control points and an image grid of size 60×80×80 : 24 sec, and 58 sec, respectively.

2. Computing the steady-state Kalman gain (only in state estimation-based 3D-3D registration). Computation time for a grid of 30×40×40 control points in a reduced-order model of size m = 200 and 500: 8 min and 20 min, respectively.

In 3D-2D registration problems, if the tissue deformation is static and all acquired 2D reference images are employed in the registration, the two above mentioned tasks are also carried out once before the start of the iterations and the steady-state Kalman gain is used in iterative estimation of the deformation states. In case the deformation is dynamic and the

Table 8.1: Computation times for tasks during iterations in state estimation-based 3D-3D registration of Section 5.2.2

Tasks		Computation Time (sec) SSD	CR	NCC	MI
1	*Time Update/Prediction*	0.02			
2	*Find Deformed Grids (Control, Image)*	(0.55, 4.03)			
3	*Interpolate Predicted Image*	0.44			
4	*Observation Prediction Error*	2.83	3.05	3.09	3.22
5	*Measurement Update*	0.03			
Total Computation Time for Each Iteration		3.6	8.6	8.7	9.1

position and orientation of the intraoperative images change over time, search algorithm, and Kalman gain computations are performed at each iteration.

Main computational tasks during the iterations in the state estimation-based 3D-3D registration were explained in Section 5.1.4. Computation times for these tasks as well as the total computation time at each iteration using different similarity/distance measures are listed in Table 8.1. The data in this table is based on a MATLAB implementation for the scenario described in Section 5.2.2. It should be noted that in the SSD-based registration, the observation prediction errors are computed directly based on intensities at the control points. Therefore, the deformation of the image grid, predicted image interpolation, and joint intensity histogram between images are not computed in SSD-based registration, which reduces the computation time.

Main computational tasks during the iterations in the optimization-based 3D-3D registration problems were discussed in Section 4.2.3. Computation times for these tasks as well as total computation time at each iteration using different similarity/distance measures are listed in Table 8.2. These times are based on a MATLAB implementation for the registration scenario presented in Section 4.3.2. As is evident from this table, the computation of the force vector in the third task consumes most of the time. As explained in Section 4.2.3,

Table 8.2: Computation times for tasks during iterations in optimization-based 3D-3D registration of Section 4.3.2

	Tasks	Computation Time (sec) SSD	CR	NCC	MI
1	*Image Interpolation*	0.44			
2	*Displacement at Control Points*	2.83	3.49	3.55	3.66
3	*Computation of the Force Vector*	147			
4	*Solution of Dynamic Equations*	1.7			
5	*Find Deformed Grids (Control, Image)*	(0.55, 4.03)			
Total Computation Time for Each Iteration		153.5	157.9	157.9	158.1

this task includes the inversion of a big matrix (4425×4425 in this case). Furthermore, comparing Table 8.1 and Table 8.2, the average computation time for each iteration in the state estimation-based 3D-3D registration is less than 5% of that in optimization-based 3D-3D registration. These two registration algorithms converge in comparable number of total iterations using identical deformation models and sample times.

After the iterations end, the deformation of the desired high-resolution image grid is computed based on the final estimated tissue deformation and the image is interpolated from the volume of the preoperative images at the deformed image grid points. It takes about 6 min to interpolate a high-resolution, 198×283×216 deformed template image in a "for loop" implementation in MATLAB. There is also the search algorithm for the high-resolution image grid points that consumes about 34 min, resulting in a significant computing time for obtaining the final high-resolution deformed image. One alternative approach to avoid these computations is to interpolate the high-resolution images using the TPS interpolation method [60, 117]. Nodal points of the FE mesh are used as control points in the TPS approximation, and the displacements field at these points are smoothly distributed to whole image grid points.

In the state estimation-based 3D-3D registration method, the deformation model and Kalman gain Γ can be computed once and used for the registration of different image sets. To this end,the control points at which the observation prediction errors are computed, are evenly distributed inside the finite element mesh and their position is fixed in the registration of different image sets. In Figure 8.1a, an axial view of the intraoperative (reference) MR images is shown. The reference image volume is scaled and transformed to be placed inside the FE mesh. As shown in Figure 8.1b, this is done in a way that the center of the reference image volume is placed at the center of the FE mesh volume and the domain of image fits the mesh volume in its largest axis, i.e., vertical axis in this case. With this configuration, the output matrix $\mathbf{H}$ in the observation model would be similar in the registration of different image sets. Therefore, the deformation and observation models in Equations (5.2) and (5.8) are those of standard linear time-invariant system. In such case, the steady-state Kalman gain Γ can be computed based on the process $\mathbf{Q}$ and measurement noise $\mathbf{S}$ covariance matrices. The registration algorithm can be further tuned by adjusting γ for different image data sets.

Most of the time consuming tasks in the proposed registration methods are highly amendable to parallelization using graphics processing units (GPUs). Previously, Mousazadeh *et al.* [197] implemented an earlier version of the SSD-based 3D-3D registration method proposed in Chapter 4 on a GPU. The 3D-3D registration of a 128×128×50 image volume was carried out in less than two seconds, achieving a 38-fold speedup over an optimized C-based CPU implementation. Similar to Table 8.2, in the GPU implementation more than 80% of the time was spent on the calculation of the force vector based on the displacements at the control points. Also, as reported in [197], speedup in GPU implementation of this task is less than others. Therefore, it is expected the state estimation-based registrations

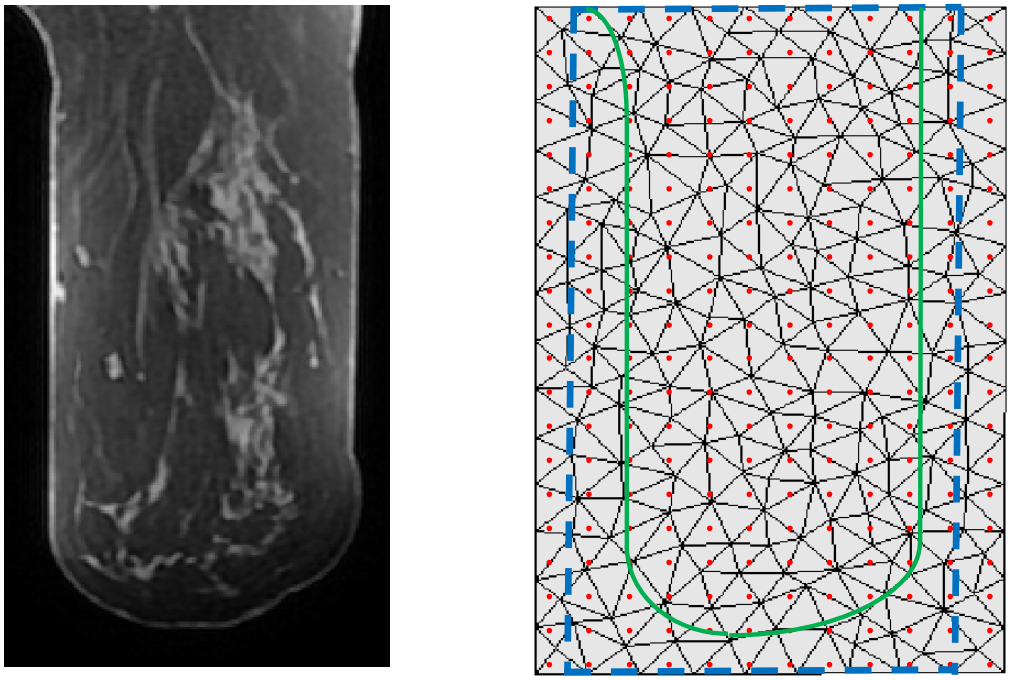

(a) Intraoperative breast image (b) FE mesh with control points

Figure 8.1: A 2D view of control points spacing inside the FE mesh. (a) An axial view of the reference breast image, (b) scaled breast inside the FE mesh with control points.

benefit even more from a GPU parallel implementation. A GPU implementation would enable applications of the proposed dynamic 3D-2D registration method for real-time tracking of tissue deformation.

8.3 Observability of the Deformation Model

It is known that state estimation for a dynamical system based on a particular set of outputs requires the system to be *observable* from those outputs [198]. In the dynamic 3D-2D registration problems presented in Chapter 7, for instance, the observability of the system guarantees that states can be estimated based on a measurement vector which contains data

from only one 2D image slice. The system model in Equations (5.2) and (5.8) is linear time-invariant for a constant set of measurements vector. Its observability can be checked based on the rank of the observability matrix of the system [198] which is defined as

$$O = \begin{bmatrix} \mathbf{H} \\ \mathbf{HA} \\ \mathbf{HA}^2 \\ \vdots \\ \mathbf{HA}^{2m-1} \end{bmatrix} \tag{8.1}$$

where m is the number of modes in the reduced dynamic deformation model which results in $2m$ states in the deformation model. The system is observable if the rank of O is equal to $2m$. The observability of the system for many different sets of measurements was examined in state estimation-based registration problems and the model was found to be observable in all these cases.

8.4 Discussion of the Results

In the single-modality registration experiments in this thesis, the simple similarity/distance measure, SSD, proved effective and robust, although not always as accurate as the other measures. CR and NCC-based registrations performed comparably well and outperformed the SSD and MI-based registrations in most cases. Consistent with previous reports, e.g., see [15, 80], it was observed that registration based on the MI would not work well for low-resolution images. To improve the performance of the MI-based registration, the resolution of the 3D image that is interpolated at each iteration must be increased; this obviously

would increase the amount of computations. Performance-wise, the proposed registration methods produced comparable results with that of IRTK in single-modality 3D-3D static registration. In 3D-2D sequence static registration, the proposed state estimation-based registration method yielded smaller TRE than IRTK registration for the identified fiducial points especially in large deformations.

The above mentioned similarity/distance measures did not perform well in dynamic 3D-2D MR-US registration. MIND-based similarity/distance metric was employed for this purpose which provided acceptable results in the registration of images acquired from a breast phantom with relatively large deformations. However, dynamic 3D-2D MR-US registration method should be evaluated on real tissue images, e.g., breast, prostate, etc., using MIND or other intensity-based similarity/distance measures to confirm the effectiveness of this approach.

Chapter 9

Conclusions and Future Work

9.1 Conclusions

Soft tissue organs undergo significant deformation between imaging sessions or during an intervention. Deformable image registration is a crucial task in combining information available in images acquired from soft tissue using similar or dissimilar imaging techniques at different times. A family of automatic elastic registration methods was proposed in this thesis which are applicable to 3D-3D and 3D-2D deformable registrations of single and multiple modality images. These methods employ a generic dynamic linear elastic continuum mechanics model of the tissue deformation which is discretized using FEM. Rather than constructing a FE model based on the actual geometry of the tissue, the deformation model is created using a cubic volume of tetrahedral elements. This generic deformation model can be employed in the registration of different image sets. Vibrational modes of the original dynamic model are decoupled using a canocial modal transformation and fast modes are isolated and discarded. The resulting reduced-order dynamic model contains only relatively slow vibrational modes of the original model. The modal reduction does not significantly affect the steady-state response of the system and facilitates estimating the

deformation field between the images with markedly reduced computations.

First, a 3D-3D registration algorithm was proposed in which the deformation field between images is estimated by balancing internal deformation forces of the elastic model against external forces derived from an intensity-based similarity/distance measure. The registration is achieved by iteratively solving the differential equations defining the deformation model based on the image-derived nodal forces. The steady-state equilibrium of the dynamic deformation model is equivalent to the minimum of a registration cost function comprised of an intensity-based similarity/distance measure, e.g., SSD, MI, CR or NCC, and the linear elastic energy of the model. This method was evaluated in the registration of 3D MR images of a realistic breast phantom to its compressed 3D high and low-resolution MR images. 3D MR images of uncompressed and compressed actual breast tissue were also registered using the proposed method.

Next, the problem of non-rigid image registration was approached from a new perspective in this thesis, namely "state estimation" for dynamical systems. A generic class of deformable registration algorithms were also proposed based on this philosophy which deal with different registration problems within a unified framework irrespective of the image modality and dimension. In this approach, static or dynamic deformation of the tissue is estimated through a Kalman-like filtering process using a generic linear elastic deformation model and an observation error computed from an intensity-based similarity/distance measure between template and reference images. With this formulation, 3D-3D and 3D-2D single and multimodality image registration problems can all be treated within the same framework. Different similarity/distance measures including CR, NCC, MI, MIND and SSD between images were employed to register single and multimodality images.

The proposed family of state estimation-based registration algorithms were evaluated in

a number of different registration scenarios. First, an instance of the general framework was developed and examined in 3D-3D registration of normal and compressed images acquired from a breast phantom as well as actual breast tissue. Another instance of the general state estimation-based registration algorithm was developed and examined in the registration of 3D MR images of a breast phantom to a sparse sequence of 2D images acquired from different cross-sections of the compressed phantom. Using a similar algorithm, 3D MR images of the actual breast tissue were also registered to a sequence of interventional 2D MR images acquired from a compressed breast. Furthermore, in the general state estimation-based registration framework, an algorithm was developed to register preoperative image volumes to real-time intraoperative 2D images of a dynamically deforming tissue. The algorithm was evaluated in tracking a target sub-volume inside the breast tissue based on registering 3D preoperative images to a sequence of real-time 2D images during a simulated MR-guided breast biopsy scenario. Using the same approach, the dynamic deformation of a breast phantom was also tracked over time based on 3D-2D MR-US image registration.

The experimental results showed that the proposed family of elastic registration methods can deal with large static and dynamic deformations of the tissue in 3D-3D, 3D-2D, single and multiple modality image registration problems. In 3D-3D registration of normal and compressed breast MR images, the average TREs were about 2 mm and 3 mm for 14.6 mm and 24.6 mm compression of the breast tissue. In the registration of 3D MR images to a sequence of nine interventional 2D MR images, the average TREs were about 2.5 mm and 4 mm for 14.6 mm and 24.6 mm compression. Furthermore, in dynamic 3D-2D MR-MR and MR-US registration scenarios in this thesis, the registration results showed that large deformation of the tissue due to inserting a biopsy needle into the breast tissue or pushing US probe against a breast phantom can be tracked with a TRE less than 2 mm.

A few key features of the proposed registration algorithms make them different from other deformable registration methods in the literature. Instead of a static model, a dynamic deformation model is employed allowing the registration algorithm to correlate information of images acquired from different orientations of deforming tissue over time. The proposed elastic model-based registration methods are automatic and directly employ gray-scale information of the images without explicit extraction of image features for the calculation of boundary conditions or external forces. Also, the formulation of image registration as state estimation of dynamical systems allows for a unified treatment of 3D-3D, 3D-2D, single and multiple modality image registration problems in static and dynamic tissue deformations within the same framework.

The employed deformation model in registration algorithms is generic and can be used for the registration of different image sets. The model is based on linear elasticity which does not use the specific geometry of the soft tissue, rather employs a generic cubic mesh of finite elements. Although the simple linear elastic deformation model is not accurate, its computational complexity in the modeling and estimation is less than complex nonlinear models which are based on the geometry of the imaged tissue. The state-estimation framework incorporates modelling and imaging uncertainties in the form of unknown process and measurement disturbances providing an acceptable trade-off between computations (time and costs) and the accuracy. However, accurate biomedical models of the soft tissue would provide better registration results in case all the applied forces and boundary conditions can be estimated. For instance, the position of the compression plates can be used as boundary conditions to find the deformation throughout the tissue having an accurate biomechanical model of the tissue deformation. In this case, the model is constructed based on the preoperative images and applied boundary conditions are computed based on the intraoperative

images as well as the user's knowledge about the anatomical structures of the the tissue and surrounding organs.

9.2 Future Work

The thesis made significant progress in the development and evaluation of a class of elastic image registration methods within a unified framework applicable to single and multimodal images of similar or dissimilar dimensions. However, it still leaves some challenging and interesting open problems for further investigations and developments. Some possible avenues for future research are discussed below.

- Evaluating the proposed state estimation-based elastic registration methods in other single and multimodality deformable image registration problems concerning different organs of the human body such as prostate, liver, lung, etc. One practical scenario is to register pretreatment high-filed high-resolution 3D MR images of the prostate to the intratreatment 2D/3D US images for motion and deformation compensation in TRUS-guided prostate cancer therapy.

- Investigating other methods in incorporating image intensity information and deformation model for estimating tissue deformation. One possible approach is to run a fast optimization loop to minimize the similarity/distance measure between images at the current predicted deformation states and then use the computed displacement correction as the observation prediction error.

- Developing other deformation models in the same framework proposed in this thesis for better estimation of large tissue deformations. Large deformation elastic or viscoelatic deformation models could be employed for this purpose.

- Integration of other image features, such as surfaces, curvatures and points, and intensity-based similarity/distance measures into the same registration framework in order to compute the observation prediction error can be investigated.
- The possibility of reducing the size of the measurement vector by developing an observation model based on preprocessed image information can be studied in future. This could reduce offline and real-time computations.
- Parallel implementation of the proposed registration methods on GPUs can also be pursued for speeding-up computationally intensive tasks. The registration algorithms can then be evaluated in real-time applications.

References

[1] P. Suetens, *Fundamentals of medical imaging*. Cambridge University Press, 2002.

[2] R. L. Galloway Jr, R. J. Maciunas, C. Edwards *et al.*, "Interactive image-guided neurosurgery," *Biomedical Engineering, IEEE Transactions on*, vol. 39, no. 12, pp. 1226–1231, 1992.

[3] A. Ardeshir Goshtasby and S. Nikolov, "Guest editorial: Image fusion: Advances in the state of the art," *Information Fusion*, vol. 8, no. 2, pp. 114–118, 2007.

[4] M. J. Gooding, K. Rajpoot, S. Mitchell, P. Chamberlain, S. H. Kennedy, and J. A. Noble, "Investigation into the fusion of multiple 4D fetal echocardiography images to improve image quality," *Ultrasound in medicine & biology*, vol. 36, no. 6, pp. 957–966, 2010.

[5] T. Beyer, D. W. Townsend, T. Brun, P. E. Kinahan, M. Charron, R. Roddy, J. Jerin, J. Young, L. Byars, R. Nutt *et al.*, "A combined PET/CT scanner for clinical oncology," *Journal of nuclear medicine*, vol. 41, no. 8, pp. 1369–1379, 2000.

[6] A. Boss, S. Bisdas, A. Kolb, M. Hofmann, U. Ernemann, C. D. Claussen, C. Pfannenberg, B. J. Pichler, M. Reimold, and L. Stegger, "Hybrid PET/MRI of intracranial masses: initial experiences and comparison to PET/CT," *Journal of Nuclear Medicine*, vol. 51, no. 8, pp. 1198–1205, 2010.

[7] S. Heywang-Köbrunner, P. Viehweg, A. Heinig, and C. Küchler, "Contrast-enhanced MRI of the breast: accuracy, value, controversies, solutions," *European journal of radiology*, vol. 24, no. 2, pp. 94–108, 1997.

[8] D. Rueckert, L. I. Sonoda, C. Hayes, D. L. G. Hill, M. O. Leach, and D. J. Hawkes, "Nonrigid registration using free-form deformations: application to breast MR images," *Medical Imaging, IEEE Transactions on*, vol. 18, no. 8, pp. 712–721, 1999.

[9] D. L. Wilson, A. Carrillo, L. Zheng, A. Genc, J. L. Duerk, and J. S. Lewin, "Evaluation of 3D image registration as applied to MR-guided thermal treatment of liver cancer," *Journal of Magnetic Resonance Imaging*, vol. 8, no. 1, pp. 77–84, 1998.

[10] S. K. Kyriacou, C. Davatzikos, S. J. Zinreich, and R. N. Bryan, "Nonlinear elastic registration of brain images with tumor pathology using a biomechanical model [MRI]," *Medical Imaging, IEEE Transactions on*, vol. 18, no. 7, pp. 580–592, 1999.

[11] U. Fischer, L. Kopka, and E. Grabbe, "Magnetic resonance guided localization and biopsy of suspicious breast lesions," *Topics in Magnetic Resonance Imaging*, vol. 9, no. 1, pp. 44–59, 1998.

[12] S. Heywang-Köbrunner, A. Heinig, D. Pickuth, T. Alberich, and R. Spielmann, "Interventional MRI of the breast: lesion localisation and biopsy," *European radiology*, vol. 10, no. 1, pp. 36–45, 2000.

[13] A. Bharatha, M. Hirose, N. Hata, S. K. Warfield, M. Ferrant, K. H. Zou, E. Suarez-Santana, J. Ruiz-Alzola, A. DAmico, R. A. Cormack *et al.*, "Evaluation of three-dimensional finite element-based deformable registration of pre-and intraoperative prostate imaging," *Medical Physics*, vol. 28, p. 2551, 2001.

[14] H. Wang, L. Dong, M. F. Lii, A. L. Lee, R. de Crevoisier, R. Mohan, J. D. Cox, D. A. Kuban, and R. Cheung, "Implementation and validation of a three-dimensional deformable registration algorithm for targeted prostate cancer radiotherapy." *International journal of radiation oncology, biology, physics*, vol. 61, no. 3, p. 725, 2005.

[15] B. Fei, J. L. Duerk, D. T. Boll, J. S. Lewin, and D. L. Wilson, "Slice-to-volume registration and its potential application to interventional MRI-guided radio-frequency thermal ablation of prostate cancer," *Medical Imaging, IEEE Transactions on*, vol. 22, no. 4, pp. 515–525, 2003.

[16] S. Xu, G. Fichtinger, R. H. Taylor, and K. R. Cleary, "Validation of 3D motion tracking of pulmonary lesions using CT fluoroscopy images for robotically assisted lung biopsy," in *Medical imaging*. International Society for Optics and Photonics, 2005, pp. 60–68.

[17] C. Meeuwis, R. M. Mann, R. D. Mus, A. Winkel, C. Boetes, J. O. Barentsz, and J. Veltman, "MRI-guided breast biopsy at 3T using a dedicated large core biopsy set: feasibility and initial results," *European journal of radiology*, vol. 79, no. 2, pp. 257–261, 2011.

[18] A. Chandler, R. Pinder, T. Netsch, J. Schnabel, D. Hawkes, D. Hill, and R. Razavi, "Correction of misaligned slices in multi-slice MR cardiac examinations by using slice-to-volume registration," in *Biomedical Imaging: Nano to Macro, 2006. 3rd IEEE International Symposium on*. IEEE, 2006, pp. 474–477.

[19] O. V. Solberg, F. Lindseth, H. Torp, R. E. Blake, N. H. TA *et al.*, "Freehand 3D ultrasound reconstruction algorithms–a review," *Ultrasound in medicine & biology*, vol. 33, no. 7, p. 991, 2007.

[20] K. Surry, W. Smith, L. Campbell, G. Mills, D. Downey, A. Fenster *et al.*, "The development and evaluation of a three-dimensional ultrasound-guided breast biopsy apparatus." *Medical image analysis*, vol. 6, no. 3, p. 301, 2002.

[21] S. C. Rose, T. I. Hassanein, D. W. Easter, R. A. Gamagami, M. Bouvet, D. H. Pretorius, T. R. Nelson, T. B. Kinney, and G. M. James, "Value of three-dimensional US for optimizing guidance for ablating focal liver tumors," *Journal of Vascular and Interventional Radiology*, vol. 12, no. 4, pp. 507–515, 2001.

[22] G. Penney, J. Blackall, M. Hamady, T. Sabharwal, A. Adam, D. Hawkes *et al.*, "Registration of freehand 3D ultrasound and magnetic resonance liver images," *Medical Image Analysis*, vol. 8, no. 1, pp. 81–91, 2004.

[23] J. Modersitzki, *Numerical methods for image registration (numerical mathematics and scientific computation)*. Oxford university press USA, 2004.

[24] P. Markelj, D. Tomaževič, B. Likar, and F. Pernuš, "A review of 3D/2D registration methods for image-guided interventions," *Medical image analysis*, vol. 16, no. 3, pp. 642–661, 2012.

[25] H. Tadayyon, A. Lasso, S. Gill, A. Kaushal, P. Guion, and G. Fichtinger, "Target motion compensation in MRI-guided prostate biopsy with static images," in *Engineering in Medicine and Biology Society (EMBC), 2010 Annual International Conference of the IEEE*. IEEE, 2010, pp. 5416–5419.

[26] K. Bathe, *Finite Element Procedures*. Englewood Cliffs, NJ: Prentice Hall, 1996.

[27] M. Ferrant, S. K. Warfield, C. R. Guttmann, R. V. Mulkern, F. A. Jolesz, and R. Kikinis, "3D image matching using a finite element based elastic deformation model," in *Medical Image Computing and Computer-Assisted Intervention–MICCAI99*. Springer, 1999, pp. 202–209.

[28] A. Samani, J. Bishop, M. J. Yaffe, and D. B. Plewes, "Biomechanical 3D finite element modeling of the human breast using MRI data," *Medical Imaging, IEEE Transactions on*, vol. 20, no. 4, pp. 271–279, 2001.

[29] M. Ferrant, S. K. Warfield, A. Nabavi, F. A. Jolesz, and R. Kikinis, "Registration of 3D intraoperative MR images of the brain using a finite element biomechanical model," in *Medical Image Computing and Computer-Assisted Intervention–MICCAI 2000*. Springer, 2000, pp. 19–28.

[30] K. Brock, M. Sharpe, L. Dawson, S. Kim, and D. Jaffray, "Accuracy of finite element model-based multi-organ deformable image registration," *Medical physics*, vol. 32, p. 1647, 2005.

[31] J. M. Hensel, C. Ménard, P. W. Chung, M. F. Milosevic, A. Kirilova, J. L. Moseley, M. A. Haider, and K. K. Brock, "Development of multiorgan finite element-based prostate deformation model enabling registration of endorectal coil magnetic resonance imaging for radiotherapy planning," *International Journal of Radiation Oncology, Biology and Physics*, vol. 68, no. 5, 2007.

[32] F. S. Azar, D. N. Metaxas, and M. D. Schnall, "A finite element model of the breast for predicting mechanical deformations during biopsy procedures," in *Mathematical Methods in Biomedical Image Analysis, 2000. Proceedings. IEEE Workshop on*. IEEE, 2000, pp. 38–45.

[33] W. G. Bradley, "History of medical imaging," *Proceedings of the American Philosophical Society*, vol. 152, no. 3, pp. 349–361, 2008.

[34] J. D. Houston and M. Davis, *Fundamentals of fluoroscopy*. Saunders, 2001.

[35] P. C. Gøtzsche and M. Nielsen, "Screening for breast cancer with mammography," *Cochrane Database Syst Rev*, vol. 4, no. 1, 2009.

[36] F. Peyrin and P. Douek, "X-ray tomography," *Photon-Based Medical Imagery*, pp. 161–205.

[37] S. I. Seldinger, "Catheter replacement of the needle in percutaneous arteriography: a new technique," *Acta Radiologica [Old Series]*, vol. 39, no. 5, pp. 368–376, 1953.

[38] R. A. Novelline and L. F. Squire, *Squire's fundamentals of radiology*. Belknap Press, 2004.

[39] "Touch screen ultrasound system," http://www.ultrasonix.com/ultrasound-systems/sonixtouch, note = Accessed: 2013-05-21.

[40] J. M. Theysohn, S. Maderwald, O. Kraff, C. Moenninghoff, M. E. Ladd, and S. C. Ladd, "Subjective acceptance of 7 Tesla MRI for human imaging," *Magnetic Resonance Materials in Physics, Biology and Medicine*, vol. 21, no. 1-2, pp. 63–72, 2008.

[41] T. Vaughan, L. DelaBarre, C. Snyder, J. Tian, C. Akgun, D. Shrivastava, W. Liu, C. Olson, G. Adriany, J. Strupp *et al.*, "9.4 T human MRI: preliminary results," *Magnetic resonance in medicine*, vol. 56, no. 6, pp. 1274–1282, 2006.

[42] J. H. Duyn, P. van Gelderen, T.-Q. Li, J. A. de Zwart, A. P. Koretsky, and M. Fukunaga, "High-field MRI of brain cortical substructure based on signal phase," *Proceedings of the National Academy of Sciences*, vol. 104, no. 28, pp. 11 796–11 801, 2007.

[43] C. R. Maurer and J. M. Fitzpatrick, "A review of medical image registration," *Interactive image-guided neurosurgery*, vol. 17, 1993.

[44] J. B. A. Maintz and M. A. Viergever, "A survey of medical image registration," *Medical Image Analysis*, vol. 2, no. 1, pp. 1–36, 1998.

[45] T. Peters, B. Davey, P. Munger, R. Comeau, A. Evans, and A. Olivier, "Three-dimensional multimodal image-guidance for neurosurgery," *Medical Imaging, IEEE Transactions on*, vol. 15, no. 2, pp. 121–128, 1996.

[46] L. Lemieux and R. Jagoe, "Effect of fiducial marker localization on stereotactic target coordinate calculation in CT slices and radiographs," *Physics in medicine and biology*, vol. 39, no. 11, p. 1915, 1994.

[47] C. R. Maurer Jr, G. B. Aboutanos, B. M. Dawant, R. A. Margolin, R. J. Maciunas, and J. M. Fitzpatrick, "Registration of CT and MR brain images using a combination of points and surfaces," in *Medical Imaging 1995*. International Society for Optics and Photonics, 1995, pp. 109–123.

[48] K. P. Gall, L. J. Verhey, and M. Wagner, "Computer-assisted positioning of radiotherapy patients using implanted radiopaque fiducials," *Medical physics*, vol. 20, p. 1153, 1993.

[49] W. D. Leslie, A. Borys, D. McDonald, J. O. Dupont, and A. E. Peterdy, "External reference markers for the correction of head rotation in brain single-photon emission tomography," *European journal of nuclear medicine*, vol. 22, no. 4, pp. 351–355, 1995.

[50] A. Krol, M. Z. Unlu, A. Magri, E. Lipson, I. L. Coman, J. A. Mandel, K. G. Baum, and D. H. Feiglin, "Iterative finite element deformable model for nonrigid coregistration of multimodal breast images," in *Biomedical Imaging: Nano to Macro, 2006. 3rd IEEE International Symposium on*. IEEE, 2006, pp. 852–855.

[51] V. R. Mandava, J. M. Fitzpatrick, C. R. Maurer Jr, R. J. Maciunas, and G. S. Allen, "Registration of multimodal volume head images via attached markers," *Medical Imaging VI: Image Processing*, vol. 1652, pp. 271–282, 1992.

[52] A. C. Evans, S. Marrett, L. Collins, and T. M. Peters, "Anatomical-functional correlative analysis of the human brain using three dimensional imaging systems," in *1989 Medical Imaging*. International Society for Optics and Photonics, 1989, pp. 264–274.

[53] C. R. Maurer Jr, J. J. McCrory, and J. M. Fitzpatrick, "Estimation of accuracy in localizing externally attached markers in multimodal volume head images," in *Medical Imaging 1993*. International Society for Optics and Photonics, 1993, pp. 43–54.

[54] R. Ellis, S. Toksvig-Larsen, M. Marcacci, D. Caramella, and M. Fadda, "Use of a biocompatible fiducial marker in evaluating the accuracy of computed tomography image registration," *Investigative Radiology*, vol. 31, no. 10, pp. 658–667, 1996.

[55] P. A. Van den Elsen, E.-J. Pol, and M. A. Viergever, "Medical image matching-a review with classification," *Engineering in Medicine and Biology Magazine, IEEE*, vol. 12, no. 1, pp. 26–39, 1993.

[56] D. L. Hill, D. Hawkes, J. Crossman, M. Gleeson, T. Cox, E. Bracey, A. Strong, and P. Graves, "Registration of MR and CT images for skull base surgery using point-like anatomical features," *British journal of radiology*, vol. 64, no. 767, pp. 1030–1035, 1991.

[57] S. Kimiaei, M. Noz, E. Jonsson, J. Crafoord, and G. Q. Maguire Jr, "Evaluation of polynomial image deformation using anatomical landmarks for matching of 3D-abdominal MR-images and for atlas construction," *Nuclear Science, IEEE Transactions on*, vol. 46, no. 4, pp. 1110–1113, 1999.

[58] N. Shusharina and G. Sharp, "Analytic regularization for landmark-based image registration," *Physics in medicine and biology*, vol. 57, no. 6, p. 1477, 2012.

[59] K. Rohr, H. S. Stiehl, R. Sprengel, T. M. Buzug, J. Weese, and M. Kuhn, "Landmark-based elastic registration using approximating thin-plate splines," *Medical Imaging, IEEE Transactions on*, vol. 20, no. 6, pp. 526–534, 2001.

[60] J. Modersitzki, *FAIR: flexible algorithms for image registration*. Society for Industrial and Applied Mathematics, 2009, vol. 6.

[61] N. Ayache, A. P. Gueziec, J.-P. Thirion, A. Gourdon, and J. Knoplioch, "Evaluating 3D registration of CT-scan images using crest lines," in *SPIE's 1993 International Symposium on Optics, Imaging, and Instrumentation*. International Society for Optics and Photonics, 1993, pp. 60–71.

[62] J. M. Balter, C. A. Pelizzari, and G. T. Chen, "Correlation of projection radiographs in radiation therapy using open curve segments and points," *Medical physics*, vol. 19, p. 329, 1992.

[63] A. Charnoz, V. Agnus, G. Malandain, L. Soler, and M. Tajine, "Tree matching applied to vascular system," in *Graph-based representations in pattern recognition*. Springer, 2005, pp. 183–192.

[64] C. Chen, C. Pelizzari, G. Chen, M. Cooper, and D. Levin, "Image analysis of PET data with the aid of CT and PMR images," in *Information processing in medical imaging*, 1987, pp. 601–611.

[65] D. N. Levin, C. Pelizzari, G. Chen, C. Chen, and M. Cooper, "Retrospective geometric correlation of MR, CT, and PET images." *Radiology*, vol. 169, no. 3, pp. 817–823, 1988.

[66] G. T. Chen and C. A. Pelizzari, "Image correlation techniques in radiation therapy treatment planning," *Computerized medical imaging and graphics*, vol. 13, no. 3, pp. 235–240, 1989.

[67] C. A. Pelizzari, G. T. Chen, D. R. Spelbring, R. R. Weichselbaum, and C.-T. Chen, "Accurate three-dimensional registration of CT, PET, and/or MR images of the brain," *Journal of computer assisted tomography*, vol. 13, no. 1, pp. 20–26, 1989.

[68] C. K. Chow, H. T. Tsui, and T. Lee, "Surface registration using a dynamic genetic algorithm," *Pattern recognition*, vol. 37, no. 1, pp. 105–117, 2004.

[69] M. A. Audette, F. P. Ferrie, and T. M. Peters, "An algorithmic overview of surface registration techniques for medical imaging," *Medical Image Analysis*, vol. 4, no. 3, pp. 201–217, 2000.

[70] M. Ferrant, A. Nabavi, B. Macq, P. Black, F. A. Jolesz, R. Kikinis, S. K. Warfield *et al.*, "Serial registration of intraoperative MR images of the brain," *Medical Image Analysis*, vol. 6, no. 4, pp. 337–359, 2002.

[71] M. R. Kaus, K. K. Brock, V. Pekar, L. A. Dawson, A. M. Nichol, and D. A. Jaffray, "Assessment of a model-based deformable image registration approach for radiation therapy planning," *International Journal of Radiation Oncology, Biology and Physics*, vol. 68, no. 2, 2007.

[72] P. A. Transformation-Alpert *et al.*, "The principal axes transformation-a method for image registration," *J Nucl Med*, vol. 31, pp. 1717–1723, 1990.

[73] L. Dong and A. L. Boyer, "A portal image alignment and patient setup verification procedure using moments and correlation techniques," *Physics in medicine and biology*, vol. 41, no. 4, pp. 697–723, 1996.

[74] P. Viola and W. M. Wells III, "Alignment by maximization of mutual information," *International journal of computer vision*, vol. 24, no. 2, pp. 137–154, 1997.

[75] F. Odille, A. Menys, A. Ahmed, S. Punwani, S. A. Taylor, and D. Atkinson, "Quantitative assessment of small bowel motility by nonrigid registration of dynamic MR images," *Magnetic Resonance in Medicine*, vol. 68, no. 3, pp. 783–793, 2012.

[76] D. L. Hill, P. G. Batchelor, M. Holden, and D. J. Hawkes, "Medical image registration," *Physics in medicine and biology*, vol. 46, no. 3, p. R1, 2001.

[77] D. Rueckert, P. Aljabar, R. A. Heckemann, J. V. Hajnal, and A. Hammers, "Diffeomorphic registration using B-splines," in *Medical Image Computing and Computer-Assisted Intervention–MICCAI 2006*. Springer, 2006, pp. 702–709.

[78] L. Lemieux, U. C. Wieshmann, N. F. Moran, D. R. Fish, and S. D. Shorvon, "The detection and significance of subtle changes in mixed-signal brain lesions by serial MRI scan matching and spatial normalization," *Medical Image Analysis*, vol. 2, no. 3, pp. 227–242, 1998.

[79] S. Kaneko, Y. Satoh, and S. Igarashi, "Using selective correlation coefficient for robust image registration," *Pattern Recognition*, vol. 36, no. 5, pp. 1165–1173, 2003.

[80] A. Roche, G. Malandain, N. Ayache, X. Pennec *et al.*, "Multimodal image registration by maximization of the correlation ratio," 1998.

[81] A. Roche, G. Malandain, X. Pennec, and N. Ayache, "The correlation ratio as a new similarity measure for multimodal image registration," in *Medical Image Computing and Computer-Assisted InterventationMICCAI98*. Springer, 1998, pp. 1115–1124.

[82] A. Roche, X. Pennec, M. Rudolph, D. Auer, G. Malandain, S. Ourselin, L. M. Auer, and N. Ayache, "Generalized correlation ratio for rigid registration of 3D ultrasound with MR images," in *Medical Image Computing and Computer-Assisted Intervention–MICCAI 2000*. Springer, 2000, pp. 567–577.

[83] C. E. Shannon and W. Weaver, "A mathematical theory of communication," 1948.

[84] J. P. W. Pluim, J. B. A. Maintz, and M. A. Viergever, "Mutual-information-based registration of medical images: a survey," *Medical Imaging, IEEE Transactions on*, vol. 22, no. 8, pp. 986–1004, 2003.

[85] F. Maes, A. Collignon, D. Vandermeulen, G. Marchal, and P. Suetens, "Multimodality image registration by maximization of mutual information," *Medical Imaging, IEEE Transactions on*, vol. 16, no. 2, pp. 187–198, 1997.

[86] J. P. Pluim, J. Antoine Maintz, and M. A. Viergever, "Interpolation artefacts in mutual information-based image registration," *Computer vision and image understanding*, vol. 77, no. 2, pp. 211–232, 2000.

[87] C. Studholme, D. L. Hill, D. J. Hawkes *et al.*, "An overlap invariant entropy measure of 3D medical image alignment," *Pattern recognition*, vol. 32, no. 1, pp. 71–86, 1999.

[88] D. Rueckert, C. Hayes, C. Studholme, P. Summers, M. Leach, and D. J. Hawkes, "Non-rigid registration of breast MR images using mutual information," in *Medical Image Computing and Computer-Assisted InterventationMICCAI98*. Springer, 1998, pp. 1144–1152.

[89] H. Luan, F. Qi, Z. Xue, L. Chen, and D. Shen, "Multimodality image registration by maximization of quantitative–qualitative measure of mutual information," *Pattern Recognition*, vol. 41, no. 1, pp. 285–298, 2008.

[90] R. Shekhar and V. Zagrodsky, "Mutual information-based rigid and nonrigid registration of ultrasound volumes," *Medical Imaging, IEEE Transactions on*, vol. 21, no. 1, pp. 9–22, 2002.

[91] D. Tomaževič, B. Likar, and F. Pernuš, "Multi-feature mutual information image registration," *Image Analysis & Stereology*, vol. 31, no. 1, pp. 43–53, 2012.

[92] A. Andronache, M. Von Siebenthal, G. Székely, and P. Cattin, "Non-rigid registration of multi-modal images using both mutual information and cross-correlation," *Medical image analysis*, vol. 12, no. 1, p. 3, 2008.

[93] A. Roche, X. Pennec, G. Malandain, and N. Ayache, "Rigid registration of 3D ultrasound with MR images: a new approach combining intensity and gradient information," *Medical Imaging, IEEE Transactions on*, vol. 20, no. 10, pp. 1038–1049, 2001.

[94] E. Haber and J. Modersitzki, "Intensity gradient based registration and fusion of multi-modal images," in *Medical Image Computing and Computer-Assisted Intervention–MICCAI 2006*. Springer, 2006, pp. 726–733.

[95] N. Papenberg, T. Lange, J. Modersitzki, P. M. Schlag, and B. Fischer, "Image registration for CT and intra-operative ultrasound data of the liver," in *Medical Imaging*. International Society for Optics and Photonics, 2008, pp. 691 808–691 808.

[96] D. Loeckx, P. Slagmolen, F. Maes, D. Vandermeulen, and P. Suetens, "Nonrigid image registration using conditional mutual information," *Medical Imaging, IEEE Transactions on*, vol. 29, no. 1, pp. 19–29, 2010.

[97] Y. Ou, A. Sotiras, N. Paragios, C. Davatzikos *et al.*, "DRAMMS: Deformable registration via attribute matching and mutual-saliency weighting," *Medical image analysis*, vol. 15, no. 4, p. 622, 2011.

[98] M. P. Heinrich, M. Jenkinson, M. Bhushan, T. Matin, F. V. Gleeson, S. M. Brady, and J. A. Schnabel, "MIND: Modality independent neighbourhood descriptor for multi-modal deformable registration," *Medical Image Analysis*, 2012.

[99] M. P. Heinrich, M. Jenkinson, M. Bhushan, T. Matin, F. V. Gleeson, J. M. Brady, and J. A. Schnabel, "Non-local shape descriptor: a new similarity metric for deformable multi-modal registration," in *Medical Image Computing and Computer-Assisted Intervention–MICCAI 2011*. Springer, 2011, pp. 541–548.

[100] L. G. Brown, "A survey of image registration techniques," *ACM computing surveys (CSUR)*, vol. 24, no. 4, pp. 325–376, 1992.

[101] E. De Castro and C. Morandi, "Registration of translated and rotated images using finite Fourier transforms," *Pattern Analysis and Machine Intelligence, IEEE Transactions on*, no. 5, pp. 700–703, 1987.

[102] J. Liu, B. C. Vemuri, and J. L. Marroquin, "Local frequency representations for robust multimodal image registration," *Medical Imaging, IEEE Transactions on*, vol. 21, no. 5, pp. 462–469, 2002.

[103] G. Tzimiropoulos, V. Argyriou, S. Zafeiriou, and T. Stathaki, "Robust FFT-based scale-invariant image registration with image gradients," *Pattern Analysis and Machine Intelligence, IEEE Transactions on*, vol. 32, no. 10, pp. 1899–1906, 2010.

[104] D. Tomazevic, B. Likar, T. Slivnik, and F. Pernus, "3D/2D registration of CT and MR to X-ray images," *Medical Imaging, IEEE Transactions on*, vol. 22, no. 11, pp. 1407–1416, 2003.

[105] R. J. Schneider, D. P. Perrin, N. V. Vasilyev, G. R. Marx, P. J. del Nido, and R. D. Howe, "Real-time image-based rigid registration of three-dimensional ultrasound," *Medical Image Analysis*, vol. 16, no. 2, pp. 402–414, 2012.

[106] P. Coupé, P. Hellier, X. Morandi, and C. Barillot, "3D rigid registration of intraoperative ultrasound and preoperative MR brain images based on hyperechogenic structures," *Journal of Biomedical Imaging*, vol. 2012, p. 1, 2012.

[107] T. Butz and J.-P. Thiran, "Affine registration with feature space mutual information," in *Medical Image Computing and Computer-Assisted Intervention–MICCAI 2001*. Springer, 2001, pp. 549–556.

[108] J. Feldmar, N. Ayache, and F. Betting, "3D–2D projective registration of free-form curves and surfaces," *Computer Vision and Image Understanding*, vol. 65, no. 3, pp. 403–424, 1997.

[109] A. Pitiot, E. Bardinet, P. Thompson, G. Malandain *et al.*, "Piecewise affine registration of biological images for volume reconstruction," *Medical image analysis*, vol. 10, no. 3, pp. 465–483, 2006.

[110] G. Seetharaman, G. Gasperas, and K. Palaniappan, "A piecewise affine model for image registration in nonrigid motion analysis," in *Image Processing, 2000. Proceedings. 2000 International Conference on*, vol. 1. IEEE, 2000, pp. 561–564.

[111] S. Zokai and G. Wolberg, "Image registration using log-polar mappings for recovery of large-scale similarity and projective transformations," *Image Processing, IEEE Transactions on*, vol. 14, no. 10, pp. 1422–1434, 2005.

[112] J. Feldmar and N. Ayache, "Rigid, affine and locally affine registration of free-form surfaces," *International journal of computer vision*, vol. 18, no. 2, pp. 99–119, 1996.

[113] R. P. Woods, S. T. Grafton, J. D. Watson, N. L. Sicotte, and J. C. Mazziotta, "Automated image registration: II. Intersubject validation of linear and nonlinear models," *Journal of computer assisted tomography*, vol. 22, no. 1, pp. 153–165, 1998.

[114] R. Wiemker, "Registration of airborne scanner imagery using akima local quintic polynomial interpolation," *San Francisco, CA*, 1996.

[115] A. Sotiras, C. Davatazikos, and N. Paragios, "Deformable medical image registration: A survey," *RR-7919, INRIA*, 2012.

[116] L. Zagorchev and A. Goshtasby, "A comparative study of transformation functions for nonrigid image registration," *Image Processing, IEEE Transactions on*, vol. 15, no. 3, pp. 529–538, 2006.

[117] F. L. Bookstein, "Principal warps: Thin-plate splines and the decomposition of deformations," *Pattern Analysis and Machine Intelligence, IEEE Transactions on*, vol. 11, no. 6, pp. 567–585, 1989.

[118] J. Li, X. Yang, and J. Yu, "Compact support thin plate spline algorithm," *Journal of Electronics (China)*, vol. 24, no. 4, pp. 515–522, 2007.

[119] K. Rohr and S. Worz, "An extension of thin-plate splines for image registration with radial basis functions," in *Biomedical Imaging (ISBI), 2012 9th IEEE International Symposium on*. IEEE, 2012, pp. 442–445.

[120] S. Marsland and C. J. Twining, "Constructing diffeomorphic representations for the groupwise analysis of nonrigid registrations of medical images," *Medical Imaging, IEEE Transactions on*, vol. 23, no. 8, pp. 1006–1020, 2004.

[121] D. Shen and C. Davatzikos, "HAMMER: hierarchical attribute matching mechanism for elastic registration," *Medical Imaging, IEEE Transactions on*, vol. 21, no. 11, pp. 1421–1439, 2002.

[122] D. Ruprecht, R. Nagel, and H. Müller, "Spatial free-form deformation with scattered data interpolation methods," *Computers & Graphics*, vol. 19, no. 1, pp. 63–71, 1995.

[123] D. Mattes, D. R. Haynor, H. Vesselle, T. K. Lewellen, and W. Eubank, "PET-CT image registration in the chest using free-form deformations," *Medical Imaging, IEEE Transactions on*, vol. 22, no. 1, pp. 120–128, 2003.

[124] T. Rohlfing, C. R. Maurer Jr, D. A. Bluemke, and M. A. Jacobs, "Volume-preserving nonrigid registration of MR breast images using free-form deformation with an incompressibility constraint," *Medical Imaging, IEEE Transactions on*, vol. 22, no. 6, pp. 730–741, 2003.

[125] S. K. Balci, P. Golland, M. Shenton, and W. M. Wells, "Free-form B-spline deformation model for groupwise registration," in *Medical image computing and computer-assisted intervention: MICCAI... International Conference on Medical Image Computing and Computer-Assisted Intervention*, vol. 10, no. WS. NIH Public Access, 2007, p. 23.

[126] M. Modat, G. R. Ridgway, Z. A. Taylor, M. Lehmann, J. Barnes, D. J. Hawkes, N. C. Fox, and S. Ourselin, "Fast free-form deformation using graphics processing units," *Computer methods and programs in biomedicine*, vol. 98, no. 3, pp. 278–284, 2010.

[127] J. Hadamard and P. M. Morse, "Lectures on cauchy's problem in linear partial differential equations," *Physics Today*, vol. 6, p. 18, 1953.

[128] G. Hermosillo, C. Chefd'Hotel, O. Faugeras *et al.*, "A variational approach to multimodal image matching," 2001.

[129] N. Cahil, J. A. Noble, and D. J. Hawkes, "Fourier methods for nonparametric image registration," in *Computer Vision and Pattern Recognition, 2007. CVPR'07. IEEE Conference on*. IEEE, 2007, pp. 1–8.

[130] B. K. Horn and B. G. Schunck, "Determining optical flow," *Artificial intelligence*, vol. 17, no. 1, pp. 185–203, 1981.

[131] J.-P. Thirion, "Image matching as a diffusion process: an analogy with Maxwell's demons," *Medical image analysis*, vol. 2, no. 3, pp. 243–260, 1998.

[132] B. Fischer and J. Modersitzki, "Curvature based image registration," *Journal of Mathematical Imaging and Vision*, vol. 18, no. 1, pp. 81–85, 2003.

[133] S. Henn, "A full curvature based algorithm for image registration," *Journal of Mathematical Imaging and Vision*, vol. 24, no. 2, pp. 195–208, 2006.

[134] B. Fischer and J. Modersitzki, "Fast curvature based registration of mr-mammography images," in *Bildverarbeitung fur die Medizin 2002*. Springer, 2002, pp. 139–142.

[135] C. Broit, "Optimal registration of deformed images," Ph.D. dissertation, University of Pennsylvania, 1981.

[136] P. Cachier and N. Ayache, "Isotropic energies, filters and splines for vector field regularization," *Journal of Mathematical Imaging and Vision*, vol. 20, no. 3, pp. 251–265, 2004.

[137] G. E. Christensen, R. D. Rabbitt, and M. I. Miller, "Deformable templates using large deformation kinematics," *Image Processing, IEEE Transactions on*, vol. 5, no. 10, pp. 1435–1447, 1996.

[138] J. A. Parker, R. V. Kenyon, and D. E. Troxel, "Comparison of interpolating methods for image resampling," *Medical Imaging, IEEE Transactions on*, vol. 2, no. 1, pp. 31–39, 1983.

[139] G. J. Grevera and J. K. Udupa, "An objective comparison of 3D image interpolation methods," *Medical Imaging, IEEE Transactions on*, vol. 17, no. 4, pp. 642–652, 1998.

[140] K. Toraichi, S. Yang, M. Kamada, and R. Mori, "Two-dimensional spline interpolation for image reconstruction," *Pattern Recognition*, vol. 21, no. 3, pp. 275–284, 1988.

[141] H. Hou and H. Andrews, "Cubic splines for image interpolation and digital filtering," *Acoustics, Speech and Signal Processing, IEEE Transactions on*, vol. 26, no. 6, pp. 508–517, 1978.

[142] C. R. Appledorn, "A new approach to the interpolation of sampled data," *Medical Imaging, IEEE Transactions on*, vol. 15, no. 3, pp. 369–376, 1996.

[143] P. Thévenaz, T. Blu, and M. Unser, *Image interpolation and resampling*. Citeseer, 2000.

[144] T. M. Lehmann, C. Gonner, and K. Spitzer, "Survey: Interpolation methods in medical image processing," *Medical Imaging, IEEE Transactions on*, vol. 18, no. 11, pp. 1049–1075, 1999.

[145] M. Unser, A. Aldroubi, and M. Eden, "Fast B-spline transforms for continuous image representation and interpolation," *IEEE Transactions on Pattern Analysis and Machine Intelligence*, vol. 13, no. 3, pp. 277–285, 1991.

[146] F. Maes, D. Vandermeulen, P. Suetens *et al.*, "Comparative evaluation of multiresolution optimization strategies for multimodality image registration by maximization of mutual information," *Medical Image Analysis*, vol. 3, no. 4, pp. 373–386, 1999.

[147] A. A. Goshtasby, *Image Registration: Principles, Tools and Methods*. Springer-Verlag New York Incorporated, 2012.

[148] S. Klein, M. Staring, and J. P. Pluim, "Evaluation of optimization methods for nonrigid medical image registration using mutual information and B-splines," *Image Processing, IEEE Transactions on*, vol. 16, no. 12, pp. 2879–2890, 2007.

[149] M. P. Wachowiak and T. M. Peters, "High-performance medical image registration using new optimization techniques," *Information Technology in Biomedicine, IEEE Transactions on*, vol. 10, no. 2, pp. 344–353, 2006.

[150] T. McInerney and D. Terzopoulos, "Deformable models in medical image analysis: a survey," *To appear in Medical Image Analysis*, vol. 1, p. 2, 1996.

[151] M. Holden, "A review of geometric transformations for nonrigid body registration," *Medical Imaging, IEEE Transactions on*, vol. 27, no. 1, pp. 111–128, 2008.

[152] G. E. Christensen, R. D. Rabbitt, and M. I. Miller, "3D brain mapping using a deformable neuroanatomy," *Physics in medicine and biology*, vol. 39, no. 3, p. 609, 1994.

[153] J. C. Gee, D. R. Haynor, M. Reivich, and R. K. Bajcsy, "Finite element approach to warping of brain images," in *Medical Imaging 1994*. International Society for Optics and Photonics, 1994, pp. 327–337.

[154] J. He and G. E. Christensen, "Large deformation inverse consistent elastic image registration," in *Information Processing in Medical Imaging*. Springer, 2003, pp. 438–449.

[155] S. F. Gibson and B. Mirtich, "A survey of deformable modeling in computer graphics," *MERL, TR-97*, vol. 19, 1997.

[156] C. Tanner, M. White, S. Guarino, M. A. Hall-Craggs, M. Douek, and D. J. Hawkes, "Large breast compressions: Observations and evaluation of simulations," *Medical Physics*, vol. 38, p. 682, 2011.

[157] Y. Hu, H. U. Ahmed, Z. Taylor, C. Allen, M. Emberton, D. Hawkes, D. Barratt *et al.*, "MR to ultrasound registration for image-guided prostate interventions," *Medical image analysis*, vol. 16, no. 3, p. 687, 2012.

[158] T.-C. Shih, J.-H. Chen, D. Liu, K. Nie, L. Sun, M. Lin, D. Chang, O. Nalcioglu, and M.-Y. Su, "Computational simulation of breast compression based on segmented breast and fibroglandular tissues on magnetic resonance images," *Physics in medicine and biology*, vol. 55, no. 14, p. 4153, 2010.

[159] A. Wittek, G. Joldes, M. Couton, S. K. Warfield, and K. Miller, "Patient-specific non-linear finite element modelling for predicting soft organ deformation in real-time; application to non-rigid neuroimage registration," *Progress in biophysics and molecular biology*, vol. 103, no. 2-3, p. 292, 2010.

[160] J. R. Crouch, S. M. Pizer, E. L. Chaney, Y.-C. Hu, G. S. Mageras, and M. Zaider, "Automated finite-element analysis for deformable registration of prostate images," *Medical Imaging, IEEE Transactions on*, vol. 26, no. 10, pp. 1379–1390, 2007.

[161] J. Eom, X. G. Xu, S. De, and C. Shi, "Predictive modeling of lung motion over the entire respiratory cycle using measured pressure-volume data, 4DCT images, and finite-element analysis," *Medical physics*, vol. 37, p. 4389, 2010.

[162] A. Nabavi, P. M. Black, D. T. Gering, C.-F. Westin, V. Mehta, R. S. Pergolizzi Jr, M. Ferrant, S. K. Warfield, N. Hata, R. B. Schwartz *et al.*, "Serial intraoperative magnetic resonance imaging of brain shift," *Neurosurgery*, vol. 48, no. 4, pp. 787–798, 2001.

[163] F. S. Azar, D. N. Metaxas, and M. D. Schnall, "A deformable finite element model of the breast for predicting mechanical deformations under external perturbations," *Academic Radiology*, vol. 8, no. 10, pp. 965–975, 2001.

[164] J. A. Schnabel, C. Tanner, A. D. Castellano-Smith, A. Degenhard, M. O. Leach, D. R. Hose, D. L. G. Hill, and D. J. Hawkes, "Validation of nonrigid image registration using finite-element methods: application to breast MR images," *Medical Imaging, IEEE Transactions on*, vol. 22, no. 2, pp. 238–247, 2003.

[165] L. Han, J. Hipwell, T. Mertzanidou, T. Carter, M. Modat, S. Ourselin, and D. Hawkes, "A hybrid fem-based method for aligning prone and supine images for image guided breast surgery," in *Biomedical Imaging: From Nano to Macro, 2011 IEEE International Symposium on*. IEEE, 2011, pp. 1239–1242.

[166] Z. Yaniv, R. Stenzel, K. Cleary, and F. Banovac, "A realistic simulation framework for assessing deformable slice-to-volume (CT-fluoroscopy/CT) registration," in *Medical Imaging*. International Society for Optics and Photonics, 2006, pp. 61 410F–61 410F.

[167] I. Kaplan, N. E. Oldenburg, P. Meskell, M. Blake, P. Church, and E. J. Holupka, "Real time MRI-ultrasound image guided stereotactic prostate biopsy," *Magnetic resonance imaging*, vol. 20, no. 3, pp. 295–299, 2002.

[168] J. Krücker, S. Xu, N. Glossop, A. Viswanathan, J. Borgert, H. Schulz, and B. J. Wood, "Electromagnetic tracking for thermal ablation and biopsy guidance: clinical evaluation of spatial accuracy," *Journal of Vascular and Interventional Radiology*, vol. 18, no. 9, pp. 1141–1150, 2007.

[169] S. Xu, J. Kruecker, P. Guion, N. Glossop, Z. Neeman, P. Choyke, A. K. Singh, and B. J. Wood, "Closed-loop control in fused MR-TRUS image-guided prostate biopsy," in *Medical Image Computing and Computer-Assisted Intervention–MICCAI 2007*. Springer, 2007, pp. 128–135.

[170] M. Bro-Nielsen, "Finite element modeling in surgery simulation," *Proceedings of the IEEE*, vol. 86, no. 3, pp. 490–503, 1998.

[171] A. Wittek, T. Dutta-Roy, Z. Taylor, A. Horton, T. Washio, K. Chinzei, and K. Miller, "Subject-specific non-linear biomechanical model of needle insertion into brain," *Computer methods in biomechanics and biomedical engineering*, vol. 11, no. 2, pp. 135–146, 2008.

[172] O. Zienkewickz and R. Taylor, *The Finite Element Method*. McGraw Hill, 1987.

[173] M. S. De Craene, A. du Bois d'Aische, I.-F. Talos, M. Ferrant, P. M. Black, F. Jolesz, R. Kikinis, B. Macq, and S. K. Warfield, "Dense deformation field estimation for brain intraoperative images registration," in *Medical Imaging 2004*. International Society for Optics and Photonics, 2004, pp. 1216–1224.

[174] L. D. Cohen and I. Cohen, "Finite-element methods for active contour models and balloons for 2D and 3D images," *Pattern Analysis and Machine Intelligence, IEEE Transactions on*, vol. 15, no. 11, pp. 1131–1147, 1993.

[175] G. Hermosillo, C. Chefd'Hotel, and O. Faugeras, "Variational methods for multimodal image matching," *International Journal of Computer Vision*, vol. 50, no. 3, pp. 329–343, 2002.

[176] G. H. Golub and C. F. Van Loan, *Matrix computations*. JHUP, 2012, vol. 3.

[177] "Triple modality biopsy training breast phantom," http://www.cirsinc.com/products/all/63/triple-modality-biopsy-training-phantom/, accessed: 2013-06-04.

[178] "COMSOL: Multiphysics and simulation software," http://www.comsol.com/, accessed: 2013-06-04.

[179] A. L. Kellner, T. R. Nelson, L. I. Cerviño, and J. M. Boone, "Simulation of mechanical compression of breast tissue," *Biomedical Engineering, IEEE Transactions on*, vol. 54, no. 10, pp. 1885–1891, 2007.

[180] A. Samani, J. Zubovits, and D. Plewes, "Elastic moduli of normal and pathological human breast tissues: an inversion-technique-based investigation of 169 samples," *Physics in medicine and biology*, vol. 52, no. 6, p. 1565, 2007.

[181] "3DSlicer: a multi-platform, free and open source software package for visualization and medical image computing," http://www.slicer.org/, accessed: 2013-06-04.

[182] "IRTK: Image registration toolkit," http://www.doc.ic.ac.uk/ dr/software/, accessed: 2013-06-24.

[183] G. Welch and G. Bishop, "An introduction to the kalman filter," 1995.

[184] G. F. Franklin, M. L. Workman, and D. Powell, *Digital control of dynamic systems*. Addison-Wesley Longman Publishing Co., Inc., 1997.

[185] W. Birkfellner, M. Figl, J. Kettenbach, J. Hummel, P. Homolka, R. Schernthaner, T. Nau, and H. Bergmann, "Rigid 2D/3D slice-to-volume registration and its application on fluoroscopic CT images," *Medical physics*, vol. 34, p. 246, 2007.

[186] N. H. Peters, C. Meeuwis, C. J. Bakker, P. T. M. Willem, A. M. Fernandez-Gallardo, R. van Hillegersberg, M. E. Schipper, and M. A. van den Bosch, "Feasibility of MRI-guided large-core-needle biopsy of suspiscious breast lesions at 3 T," *European radiology*, vol. 19, no. 7, pp. 1639–1644, 2009.

[187] L. Liberman, E. A. Morris, D. D. Dershaw, C. M. Thornton, K. J. Van Zee, and L. K. Tan, "Fast MRI-guided vacuum-assisted breast biopsy: initial experience," *American Journal of Roentgenology*, vol. 181, no. 5, pp. 1283–1293, 2003.

[188] R. F. Wagner, S. W. Smith, J. M. Sandrik, and H. Lopez, "Statistics of speckle in ultrasound B-scans," *IEEE TRANS. SONICS ULTRASONICS.*, vol. 30, no. 3, pp. 156–163, 1983.

[189] A. Buades, B. Coll, and J.-M. Morel, "A non-local algorithm for image denoising," in *Computer Vision and Pattern Recognition, 2005. CVPR 2005. IEEE Computer Society Conference on*, vol. 2. IEEE, 2005, pp. 60–65.

[190] "FlexPDE 6: PDE Solution INC," http://www.pdesolutions.com/, accessed: 2013-07-01.

[191] J. P. Whiteley, D. J. Gavaghan, S. J. Chapman, and J. M. Brady, "Non-linear modelling of breast tissue," *Mathematical Medicine and Biology*, vol. 24, no. 3, pp. 327–345, 2007.

[192] M. E. Ladd, P. Erhart, J. F. Debatin, B. J. Romanowski, P. Boesiger, and G. C. McKinnon, "Biopsy needle susceptibility artifacts," *Magnetic resonance in medicine*, vol. 36, no. 4, pp. 646–651, 1996.

[193] V. Rasche, D. Holz, J. Köhler, R. Proksa, and P. Röschmann, "Catheter tracking using continuous radial MRI," *Magnetic resonance in medicine*, vol. 37, no. 6, pp. 963–968, 1997.

[194] A. Shankaranarayanan, M. Wendt, A. J. Aschoff, J. S. Lewin, and J. L. Duerk, "Radial keyhole sequences for low field projection reconstruction interventional MRI," *Journal of Magnetic Resonance Imaging*, vol. 13, no. 1, pp. 142–151, 2001.

[195] S. Roujol, M. Ries, B. Quesson, C. Moonen, and B. Denis de Senneville, "Real-time MR-thermometry and dosimetry for interventional guidance on abdominal organs," *Magnetic Resonance in Medicine*, vol. 63, no. 4, pp. 1080–1087, 2010.

[196] "HOLOGIC: The women's health company," http://www.hologic.com/en/, note = Accessed: 2013-07-02.

[197] H. Mousazadeh, B. Marami, S. Sirouspour, and A. Patriciu, "GPU implementation of a deformable 3D image registration algorithm," in *Engineering in Medicine and Biology Society, EMBC, 2011 Annual International Conference of the IEEE*. IEEE, 2011, pp. 4897–4900.

[198] C.-T. Chen, *Linear system theory and design*. Oxford University Press, Inc., 1998.

[199] N. M. Newmark, "A method of computation for structural dynamics," in *Proc. ASCE*, vol. 85, no. 3, 1959, pp. 67–94.

[200] R. S. Bucy and P. D. Joseph, *Filtering for stochastic processes with applications to guidance*. American Mathematical Soc., 1987, vol. 326.

Appendix A

Newmark Integration Method

Newmark in [199] proposed a direct integration method for the computation of structural dynamics. This method is employed in this thesis to solve the linear dynamic equations of deformation in the form of

$$\mathbf{M}\ddot{\mathbf{u}} + \mathbf{C}\dot{\mathbf{u}} + \mathbf{K}\mathbf{u} = -\mathbf{f}(\mathbf{u}) \tag{A.1}$$

where $\mathbf{M}$, $\mathbf{C}$ and $\mathbf{K}$ are the mass, damping and stiffness matrices respectively. $\mathbf{f}(\mathbf{u})$ is the vector of external applied forces, which is computed based on the image similarity/distance measures using Equation (4.2). $\mathbf{f}(\mathbf{u})$ is computed at each sample time T_s and is assumed to be constant during the integration time step. The time step for integration is given by

$$\Delta t = \frac{T_s}{n_t} \tag{A.2}$$

where n_t is the number of time steps that each sampling time T_s is divided. In the experiments of this thesis $n_t = 10$. The selection of T_s was discussed in Equation (4.11).

In the Newmark integration method, the following approximations are employed [26]

$$\dot{\mathbf{u}}_{t+\Delta t} = \dot{\mathbf{u}}_t + [(1-\delta)\ddot{\mathbf{u}}_t + \delta\ddot{\mathbf{u}}_{t+\Delta t}]\,\Delta t \tag{A.3a}$$

$$\mathbf{u}_{t+\Delta t} = \mathbf{u}_t + \dot{\mathbf{u}}_t\Delta t + \left[(\tfrac{1}{2}-\xi)\ddot{\mathbf{u}}_t + \xi\ddot{\mathbf{u}}_{t+\Delta t}\right]\Delta t^2 \tag{A.3b}$$

where δ and ξ are the parameters of the method which can be tuned to obtain a desired integration accuracy. Newmark originally proposed that $\delta = 1/2$ and $\xi = 1/4$ would provide unconditionally stable results. To find the displacement of the FE mesh, Equation (A.1) at time $t + \Delta t$ is considered as

$$\mathbf{M}\ddot{\mathbf{u}}_{t+\Delta t} + \mathbf{C}\dot{\mathbf{u}}_{t+\Delta t} + \mathbf{K}\mathbf{u}_{t+\Delta t} = -\mathbf{f}(\mathbf{u}_{t+\Delta t}) \tag{A.4}$$

Solving from (A.3b) for $\ddot{\mathbf{u}}_{t+\Delta t}$ in terms of $\mathbf{u}_{t+\Delta t}$ and substituting $\ddot{\mathbf{u}}_{t+\Delta t}$ into (A.3a), $\dot{\mathbf{u}}_{t+\Delta t}$ and $\ddot{\mathbf{u}}_{t+\Delta t}$ can be obtained in terms of the unknown displacements $\mathbf{u}_{t+\Delta t}$. Then, these two relations for $\dot{\mathbf{u}}_{t+\Delta t}$ and $\ddot{\mathbf{u}}_{t+\Delta t}$ are substituted into (A.4) to solve for $\mathbf{u}_{t+\Delta t}$. After computing $\mathbf{u}_{t+\Delta t}$, $\dot{\mathbf{u}}_{t+\Delta t}$ and $\ddot{\mathbf{u}}_{t+\Delta t}$ can also be calculated using Equations (A.3a) and (A.3b).

The step-by-step algorithm for the solution of Equation (A.1) using Newmark integration method is as follows [26]

A. *Initial Calculations*

1. Initialize $\mathbf{u}_0$, $\dot{\mathbf{u}}_0$ and $\ddot{\mathbf{u}}_0$.

2. Select time step Δt, parameters δ and ξ in a way that

   $\delta \geq 0.5$ and $\xi \geq 0.25(0.5+\delta)^2$

   which are also stability conditions.

3. Calculate the integration constants

$a_0 = \frac{1}{\xi \Delta t^2}$ $a_1 = \frac{\delta}{\xi \Delta t}$ $a_2 = \frac{1}{\xi \Delta t}$ $a_3 = \frac{1}{2\xi} - 1$

$a_4 = \frac{\delta}{\xi} - 1$ $a_5 = \frac{\Delta t}{2}\left(\frac{\delta}{\xi} - 2\right)$ $a_6 = \Delta t(1-\delta)$ $a_7 = \delta \Delta t$

4. Construct the effective stiffness matrix as $\mathbf{K}_e = \mathbf{K} + a_0\mathbf{M} + a_1\mathbf{C}$.

B. *At Each Time Step*

1. Calculate the effective load at time $t + \Delta t$:

   $\mathbf{f}_e(\mathbf{u}_{t+\Delta t}) = \mathbf{f}(\mathbf{u}_{t+\Delta t}) - \mathbf{M}(a_0\mathbf{u}_t + a_2\dot{\mathbf{u}}_t + a_3\ddot{\mathbf{u}}_t) + \mathbf{C}(a_1\mathbf{u}_t + a_4\dot{\mathbf{u}}_t + a_5\ddot{\mathbf{u}}_t)$

2. Solve for displacement field at time $t + \Delta t$:

   $\mathbf{K}_e\mathbf{u}_{t+\Delta t} = -\mathbf{f}_e(\mathbf{u}_{t+\Delta t})$

3. Calculate acceleration and velocities at time $t + \Delta t$:

   $\ddot{\mathbf{u}}_{t+\Delta t} = a_0(\mathbf{u}_{t+\Delta t} - \mathbf{u}_t) - a_2\dot{\mathbf{u}}_t - a_3\ddot{\mathbf{u}}_t$

   $\dot{\mathbf{u}}_{t+\Delta t} = \dot{\mathbf{u}}_t + a_6\ddot{\mathbf{u}}_t + a_7\ddot{\mathbf{u}}_{t+\Delta t}$

Appendix B

Steady-State Equilibrium in State Estimation-Based Registration

In the method proposed in Chapter 4, the registration is achieved when the weighted linear elastic energy of the deformation model gets into a balance with externals potential energy defined as a similarity/distance measure between images. In other words, the displacement field of the images is estimated in a way that internal elastic forces of the deformation model and external image-derived forces are balances. Therefore, the steady-state equilibrium equations of the deformation model become

$$\mathbf{Ku} = -\mathbf{f}(\mathbf{u}) = -\frac{1}{\gamma}\Lambda^{+}\,\nabla I_{\mathbf{x}_c}(R, T[\mathbf{u}]). \tag{B.5}$$

as given is Equation (4.9). In this appendix, the steady-state equilibrium equations in the state estimation-based registration method are derived when the tissue undergoes a static deformation. To simplify the analysis, a continuous-time Kalman formulation is considered

here. The dynamic FE deformation model developed in Chapter 3 is

$$\mathbf{M}\ddot{\mathbf{u}} + \mathbf{C}\dot{\mathbf{u}} + \mathbf{K}\mathbf{u} = -\mathbf{f} \tag{B.6}$$

Assume that $\mathbf{y} = [\mathbf{y}_1; \mathbf{y}_2] = [\mathbf{u}; \dot{\mathbf{u}}]$. With this change of variables, the continuous-time state-space equations for the observer model can be written as

$$\dot{\mathbf{y}} = \mathbf{A}\mathbf{y} + \mathbf{G}\mathbf{f} + \mathbf{w} \tag{B.7}$$

$$\mathbf{z} = \mathbf{H}\mathbf{y} + \mathbf{v} \tag{B.8}$$

where

$$\mathbf{A} = \begin{bmatrix} 0 & \mathbf{I} \\ -\mathbf{M}^{-1}\mathbf{K} & -\mathbf{M}^{-1}\mathbf{C} \end{bmatrix};\ \mathbf{G} = \begin{bmatrix} 0 \\ \mathbf{M}^{-1} \end{bmatrix} \tag{B.9}$$

and $\mathbf{w}$ and $\mathbf{v}$ are process and measurement noise respectively. Here, the vector of applied forces on the tissue $\mathbf{f}$ is unknown and is modelled as part of the process noise $\mathbf{w}$ as white Gaussian noise with a normal probability distribution of $p(\tilde{\mathbf{f}}) = N(0, \mathbf{S})$. In the continuous-time Kalman filtering, the state observer dynamics can be written as [200]

$$\dot{\hat{\mathbf{y}}} = \mathbf{A}\hat{\mathbf{y}} + \Gamma\mathbf{d}\mathbf{x}_c \tag{B.10}$$

where $\Gamma = [\Gamma_1; \Gamma_2]$ is the steady-state Kalman gain computed for the continuous-time model and $\mathbf{d}\mathbf{x}_c$ is the observation prediction error given in Equation (5.10). In the steady-state

equilibrium $\dot{\hat{\mathbf{y}}} = 0$, i.e., $[\dot{\hat{\mathbf{u}}}; \ddot{\hat{\mathbf{u}}}] = 0$ which yields

$$\mathbf{A}\hat{\mathbf{y}} + \Gamma \mathbf{d}\mathbf{x}_c = 0 \tag{B.11}$$

or

$$-\mathbf{M}^{-1}\mathbf{K}\hat{\mathbf{y}}_1 - \mathbf{M}^{-1}\mathbf{C}\hat{\mathbf{y}}_2 + \Gamma_2 \mathbf{d}\mathbf{x}_c. \tag{B.12}$$

Since at steady-state $\hat{\mathbf{y}}_2 = \dot{\hat{\mathbf{u}}} = 0$ and $\hat{\mathbf{y}}_1 = \hat{\mathbf{u}}$, Equation (B.12) becomes

$$\mathbf{K}\hat{\mathbf{u}} = \mathbf{M}\Gamma_2 \mathbf{d}\mathbf{x}_c \tag{B.13}$$

and using Equation (5.10), one can write

$$\mathbf{K}\hat{\mathbf{u}} = -\mathbf{f}(\hat{\mathbf{u}}) = -\frac{1}{\gamma}\mathbf{M}\Gamma_2 \nabla I_{\mathbf{x}_c}(R, T[\hat{\mathbf{u}}]) \tag{B.14}$$

Comparing Equations (B.5) and (B.14), it can be concluded that in both methods, the internal elastic forces get into a balance with external image-derived forces. Although external forces are computed based on the derivative of the similarity/distance measure at control points in both methods, they are slightly different.